

Co on Pt(111)
studied by
spin-polarized
scanning tunneling microscopy
and spectroscopy

Dissertation
zur Erlangung des Doktorgrades
im Department Physik
der Universität Hamburg

vorgelegt von

Focko Karl Meier
aus Norden/Ostfriesland

Hamburg
2006

Gutachter der Dissertation:
Prof. Dr. R. Wiesendanger
Prof. Dr. R. L. Johnson

Gutachter der Disputation:
Prof. Dr. R. Wiesendanger
Prof. Dr. W. Wurth

Datum der Disputation:
27.10.2006

Vorsitzender des Prüfungsausschusses:
Dr. A. Chudnovskiy

Vorsitzender des Promotionsausschusses:
Prof. Dr. G. Huber

Departmentleiter:
Prof. Dr. R. Klanner

Abstract

In this thesis the electronic properties of the bare Pt(111) surface, the structural, electronic, and magnetic properties of monolayer and double-layer high Co nanostructures as well as the spin-averaged electronic structure of single Co atoms on Pt(111) were studied by low-temperature scanning tunneling microscopy (STM) and spectroscopy (STS).

The experiments on the bare Pt(111) surface and on single Co atoms have been performed in an STM facility operating at temperatures of down to 0.3 K and at magnetic fields of up to 14 T under ultra-high vacuum conditions. The facility has been taken into operation within the time period of this thesis and its specifications were tested by STS measurements. These characterization measurements show a very high stability of the tunneling junction and an energy resolution of about $100 \mu\text{eV}$, which is close to the thermal limit.

The investigation of the electronic structure of the bare Pt(111) surface reveals the existence of an unoccupied surface state. By a comparison of the measured dispersion to first-principles electronic structure calculations the state is assigned to an *sp*-derived surface band at the lower boundary of the projected bulk band-gap. The surface state exhibits a strong spin-orbit coupling induced spin splitting. The close vicinity to the bulk bands leads to a strong linear contribution to the dispersion and thus to a deviant appearance in the density of states in comparison to the surface states of the (111) surfaces of noble metals.

A detailed study of Co monolayer and double-layer nanostructures on the Pt(111) surface shows that both kinds of nanostructures exhibit a highly inhomogeneous electronic structure which changes at the scale of only a few Å due to a strong stacking dependence with respect to the Pt(111) substrate. With the help of first principles calculations the different spectroscopic appearance for Co atoms within the Co monolayer is assigned to a stacking dependent hybridization of Co states with the substrate states. Despite this electronic inhomogeneity, the magnetic domains and domain walls are clearly observed by spin-resolved STS. For both types of Co nanostructures the out-of-plane orientation of the magnetic moments is proven. Furthermore, new insights into the anisotropy of the Co nanostructures as well as a strong dependence of the coercivity on the local sample morphology for Co double-layer islands were found.

The experiments performed on single Co atoms on the Pt(111) surface show that two groups of Co atoms are present on the surface. Each group can be characterized by a specific spectroscopic signature. An analysis of the spectroscopy and atom manipulation experiments proves that the spectroscopic differences are related to the two possible adsorption sites of the Co atoms on the Pt(111) substrate.

Zusammenfassung

In dieser Arbeit wurden die elektronischen Eigenschaften der reinen Pt(111)-Oberfläche, die strukturellen, elektronischen und magnetischen Eigenschaften von ein- und zweilagigen Co-Nanostrukturen sowie die spin-gemittelte elektronische Struktur von einzelnen Co-Atomen auf Pt(111) mittels Tief-Temperatur-Rastertunnelmikroskopie (RTM) und -spektroskopie (RTS) untersucht.

Die Experimente auf der reinen Pt(111)-Oberfläche und den Co-Einzelatomen wurden in einer RTM-Anlage durchgeführt, die unter Ultrahochvakuum-Bedingungen bei Temperaturen bis zu 0.3 K und bei Magnetfeldern bis zu 14 T arbeitet. Während meiner Arbeit wurde die Anlage in Betrieb genommen. Die Spezifikationsmessungen haben gezeigt, daß die Anlage über einen außerordentlich stabilen Tunnelkontakt und eine Energieauflösung von $100 \mu\text{eV}$ verfügt, die nahe am thermischen Limit liegt.

Die Untersuchung der elektronischen Struktur der reinen Pt(111)-Oberfläche wiesen die Existenz eines unbesetzten Oberflächenzustandes nach. Durch den Vergleich der gemessenen Dispersion mit *ab initio*-Rechnungen zur elektronischen Struktur kann der Zustand einem *sp*-artigen Oberflächenband oberhalb der unteren Grenze der projizierten Bulkbandlücke zugeordnet werden. Aufgrund der Spin-Bahn-Kopplung ist der Zustand spinaufgespalten. Die Nähe zu den Bulk-bändern führt zu einem starken linearen Beitrag zur Dispersion und somit auch zu einem abweichenden Erscheinen in der gemessenen Zustandsdichte im Vergleich zu den Oberflächenzuständen der (111)-Edelmetalloberflächen.

Eine detaillierte Studie der ein- und zweilagigen Co-Nanostrukturen zeigt, daß beiden Nanostrukturen eine höchst inhomogene elektronische Struktur zu eigen ist, die sich aufgrund des starken Einflusses der Stapelung bezüglich des Pt-Substrats innerhalb weniger Å ändert. Mit Hilfe von *ab initio*-Rechnungen kann die unterschiedliche spektroskopische Erscheinung der Co-Atome innerhalb einer Monolage auf die stapelungsabhängige Hybridisierung der Co-Zustände mit den Substratzuständen zurückgeführt werden. Trotz dieser elektronischen Ungleichmäßigkeit können magnetische Domänen und Domänenwände klar mittels spin-aufgelöster RTS beobachtet werden. Desweiteren wurden neue Einblicke hinsichtlich der Anisotropie der Co-Nanostrukturen sowie der starken Abhängigkeit des Koerzitivätsfeldes von der Morphologie der Co-Doppellageninseln gewonnen.

Die Experimente, die auf den Co-Einzelatomen durchgeführt wurden, zeigen, daß zwei Gruppen von Co-Atomen auf der Pt(111)-Oberfläche zu finden sind. Jede Gruppe zeichnet sich durch eine spezifische spektroskopische Signatur aus. Eine Analyse der spektroskopischen Messungen und der Atommanipulations-Experimente läßt schlußfolgern, daß die beobachteten Unterschiede auf die zwei möglichen Adsorptionplätze der Co-Atome auf dem Pt-Substrat zurückzuführen sind.

Contents

Abstract	i
Zusammenfassung	ii
1 Introduction	1
2 Scanning tunneling microscopy and spectroscopy	4
2.1 How does an STM work?	4
2.2 The tunneling effect in one dimension	6
2.3 Tersoff-Hamann-Model	8
2.4 Scanning tunneling spectroscopy	10
2.5 Spin-resolved STM/STS	12
2.6 Tip preparation	16
2.7 Measurement modes	18
3 Instrumentation	20
3.1 Setup	20
3.2 Low temperature properties	26
3.2.1 Cooling procedure	26
3.2.2 Base temperature hold time	27
3.2.3 z-stability	28
3.2.4 Energy resolution	30
3.2.5 Spin resolution	34
4 The Pt(111) surface and its surface state	37
4.1 Introduction	37
4.2 Preparation of the Pt(111) surface	43
4.3 Experimental results	45
4.4 Theoretical results	50
4.5 Discussion	52
4.6 Summary	54
5 Co nanostructures on Pt(111)	55
5.1 Introduction	55
5.2 Experimental details	57

5.3	Structure and spin-resolved electronic properties of monolayer Co wires and islands	58
5.3.1	Experimental results	58
5.3.2	Theoretical results	65
5.3.3	Discussion	69
5.4	Structural and spin-resolved electronic properties of double-layer Co islands	70
5.5	Magnetism of Co nanostructures	73
5.5.1	Co monolayer nanostructures	74
5.5.2	Co double-layer nanostructures	77
5.6	Summary	80
6	Single Co atoms on Pt(111)	82
6.1	Introduction	82
6.2	Preparation	87
6.3	Electronic properties	88
6.4	Manipulation	95
6.5	Height switching	98
6.6	Summary	101
7	Conclusions and outlook	102
	Bibliography	105

1 Introduction

The magnetism of ultrathin films and nanostructures is a field of interest which is located at the border line between technology and basic research [1, 2]. The advanced knowledge of the physics of magnetic nanostructures will be beneficial for the increasing demand of storage density in technology development, which is achievable through smaller magnetic units.

The properties of nanoscale magnetic systems cannot be simply obtained by scaling down the properties of macroscopic magnetic systems, which consist of 10^{23} magnetic moments. For magnetic nanostructures on substrates this number is decreased by more than 18 orders of magnitude. Consequently, this reduction in size and in dimensionality goes in hand with a reduction of coordination for the magnetic atoms and leads to an important role of the underlying substrate.

While the reduction of the spatial extent and shape of the system has dramatic consequences for the size of magnetic domains and domain walls, the impact of the reduced coordination is threefold. First, it leads to a reduced exchange interaction for each magnetic atom. Second, it generally increases the spin moment and thus may induce magnetism even for materials which are nonmagnetic in bulk. Third, the reduced coordination tends to increase the orbital moments, which increases the magnetocrystalline anisotropy [3,4]. Finally, the substrate may also affect the spin and orbital moment of the magnetic atoms of the nanostructure by hybridization with their electronic states which reveals the importance of the position of the atoms. The substrate, size and shape thus govern the interplay between exchange interaction, magnetocrystalline anisotropy, and surface anisotropy and determine the magnetic properties of the system concerning the magnetic ordering, the direction and strength of the magnetic anisotropy energy as well as the strength of the coercivity.

The magnetic properties of nanostructures cannot be rationalized without taking into account the dimensionality, size, and shape of the nanostructure as well as the structural and electronic properties of the substrate.

A highly interesting model system to study the impact of shape and reduced dimensions is Co/Pt(111). Thin Co films on Pt(111) [5,6], monolayer and double-layer high Co islands [7], Co wires [8,9] and single Co atoms on Pt(111) [4] have been investigated concerning their magnetic anisotropy by spatially averaging techniques. These studies revealed, that the perpendicular magnetic anisotropy, which is observed for ultrathin Co films on Pt(111), is conserved even for Co islands and single atoms, which exhibit a giant magnetic anisotropy of 9 meV per

atoms. In contrast to this the magnetic orientation of ferromagnetic Co wires decorating Pt step edges is canted with respect to the surface normal.

A perfect tool to study the interaction of the structural, electronic, and magnetic properties of magnetic nanostructures as well as single magnetic atoms is the spin-polarized scanning tunneling microscopy (SP-STM). This measurement technique is based on the pioneering work of Binnig *et al.*, who succeeded in the realization of the first scanning tunneling microscope (STM) in 1981 [10, 11]. Nearly one decade later, first experiments revealed the opportunities which are given by expanding scanning tunneling microscopy by a magnetic sensitivity using magnetic tips [12]. Nowadays, SP-STM is highly advanced technique for probing surface magnetism at the local scale [13].

In this thesis the correlation of topographic, electronic, and magnetic properties of Co nanostructures on the Pt(111) surface is investigated by spin-resolved STM at the atomic scale. Experiments were performed on the bare Pt(111) surface, monolayer and double-layer high Co nanostructures as well as single Co atoms on Pt(111).

After a brief introduction into the experimental and theoretical aspects of SP-STM in Chap. 2, the setup and the performed characterization measurements of a ^3He STM facility operating under ultra high vacuum and high magnetic fields will be described in Chap. 3. Due to its properties this facility is highly qualified for STM experiments which demand a high lateral, energy, and spin resolution as well as for sample systems, whose magnetization has to be stabilized by low temperatures, like for example single atoms or very small superparamagnetic islands.

In Chap. 4 the results concerning the electronic structure of the bare Pt(111) surface are presented. By scanning tunneling spectroscopy it was possible to reveal the existence of an unoccupied surface state, which was not imaged before. Furthermore, a comparison to bandstructure calculations gives insight into the origin of the surface state, its energetic position with respect to the bulk bands and its spin-splitting. The differences of the surface state on Pt(111) to surface states on noble metals are discussed in detail.

Chapter 5 contains a detailed study of Co monolayer and double-layer nanostructures on Pt(111) at the atomic scale. Both kinds of nanostructures show a highly inhomogeneous electronic structure due to a strong stacking dependence with respect to the Pt(111) substrate. First principles calculations are able to explain the different spectroscopic appearance for Co atoms within the Co monolayer nanostructure due to a stacking dependent hybridization of Co states with the substrate states. Despite this electronic inhomogeneity at the scale of only a few Å, SP-STM is able to image domains and domain walls.

For both sample systems the out-of-plane orientation of the magnetic moments of the nanostructures is proven. Due to the magnetic sensitivity new insights into the anisotropy of the Co nanostructures as well as a strong dependence of the coercivity on the local sample morphology for Co double-layer islands were found.

Chapter 6 shows the spin-averaged results obtained on single Co atoms on Pt(111). Two groups of atoms will be presented which can be characterized by different spectroscopic signatures. Due to a combined spectroscopy and manipulation experiment each group of atoms can be assigned to a different adsorption site on the Pt(111) surface.

Finally, Chap. 7 gives a summary of the results presented in this thesis as well as an outlook regarding the ongoing work.

2 Scanning tunneling microscopy and spectroscopy

In this chapter, a brief introduction into scanning tunneling microscopy and spectroscopy will be given. After presenting the working principle of the scanning tunneling microscope (STM) (Sec. 2.1), a simplified picture of the tunneling process is discussed (Sec. 2.2). A more realistic description of the tunneling process — the Tersoff-Hamann model — will be presented (Sec. 2.3) due to its great importance for the description and the interpretation of the experimental results. This is followed by an introduction to scanning tunneling spectroscopy (STS) (Sec. 2.4) and spin-resolved scanning tunneling spectroscopy (SP-STs) (Sec. 2.5). It will be pointed out why scanning tunneling microscopy is such a powerful tool to study the structural, electronic, and magnetic properties down to the atomic scale. The tip preparation (Sec. 2.6) and the various STM measurement modes (Sec. 2.7) are explained at the end of this chapter.

A more detailed introduction to the theoretical as well as technical aspects of scanning tunneling microscopy is, for example, given in Refs. [14, 15].

2.1 How does an STM work?

Twentyfive years after the first construction of an STM, the basic concept of the setup is still the same [16]. It consists of a conductive sample, a metallic tip, which is the probe head, and a very accurate regulation of the tip position as shown in Fig. 2.1.

The STMs used in this thesis regulate the position of the tip by a piezoelectric actuator called tube scanner according to its shape. It consists of a hollow cylinder made from piezoelectric material. A smart arrangement of electrodes on this tube scanner allows a vertical (z) as well as a horizontal (x, y) tip movement with an accuracy better than 1 pm. During operation the distance between tip and sample is reduced to only several Å, which leads to an overlap of the wave functions of the outward tip atom and of the sample atoms. When applying a so-called bias voltage U to the sample with respect to the tip, a current can flow between both electrodes because of the quantum mechanical tunneling effect (see Sec. 2.2). Therefore, the current is called tunneling current. It is the primary measurement signal of all STM experiments. The applied bias voltages, which are typically in the range

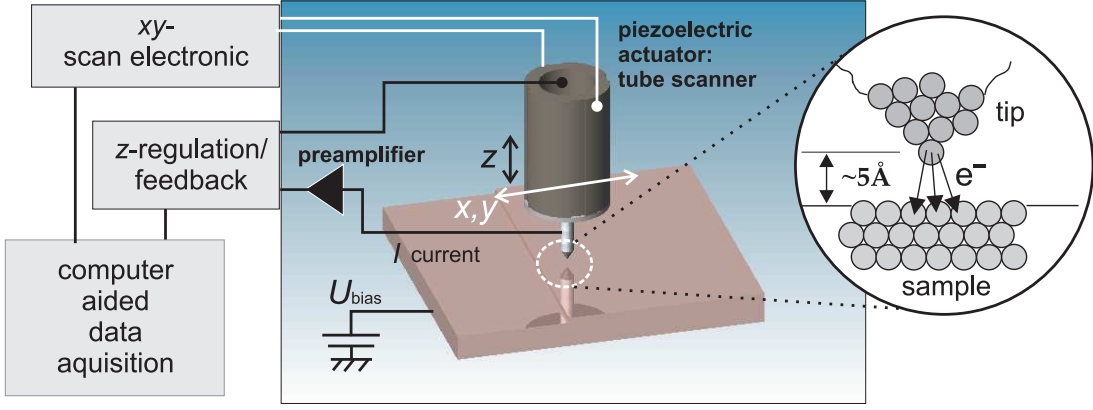


Figure 2.1: Sketch of the operating mode of the STM. A sharp metallic tip is mounted on top of a piezoelectric actuator. The topmost atoms of the tip have a distance of only a few Å to the sample. By applying a bias voltage U between tip and sample a small and strongly distance dependent current flows. The tip is scanned via the piezoelectric actuator line by line above a certain area of the sample. Meanwhile, the tunneling current serves as feedback control parameter for the positioning of the tip which follows the contour of the surface approximately at a constant distance.

of several mV to 3 V, result in tunneling currents I of a few pA up to several nA. Taking into account the Tersoff-Hamann model, which will be discussed in Sec. 2.3, the tunneling current I is described by

$$I \propto \int_0^{eU} \rho_s(E_F + \epsilon) \cdot \rho_t(E_F - eU + \epsilon) \cdot T(\epsilon, U, s) d\epsilon, \quad (2.1)$$

where the indices s and t mark the sample and tip density of states ρ . The so-called transmission coefficient $T(E, U, s)$ is given by

$$T(E, U, s) \cong \exp \left[-s \cdot \sqrt{\frac{4m_e}{\hbar^2} (\phi_t + \phi_s + eU - 2E)} \right] \quad (2.2)$$

with the effective tunneling distance s and the corresponding work functions ϕ . \hbar is Planck's constant divided by 2π and m_e is the mass of a free electron. If the bias voltage is small compared to the work functions, I is thus exponentially depending on s :

$$I \propto \exp \left(-2s \sqrt{\frac{m_e}{\hbar^2} (\phi_s + \phi_t) - eU} \right). \quad (2.3)$$

Equations 2.1 and 2.2 show that fundamental sample and tip properties influence the current I and therefore can be extracted from this primary measurement signal.

The exponential dependence between the tunneling current and the effective tunnel distance s causes the extremely high sensitivity concerning any variations of the tunneling distance. Typically, the increase of the distance by 1 Å leads to a decrease of I by a factor of ten. How this distance sensitivity is used in order to obtain topographic images of the sample surface with very high lateral resolution is shown in Fig. 2.1. An atomically sharp tip is approached to the sample until a fixed chosen current I_0 is detected when applying a selected constant bias voltage. The current is measured by a preamplifier and compared to I_0 . A z -regulation unit, which consists of a feedback loop, controls the z -movement of the tip by applying U_Z to the z -electrode of the tube scanner until the measured current equals I_0 . This is done during scanning a selected surface area (x - y plane) thus achieving a map of $U_Z(x,y)$. When the tip approaches e.g. a protrusion on the surface, the tip has to be retracted by changing U_Z . These differences in U_Z can be calibrated and translated into real height differences. Therefore, the height differences with respect to the lateral position result in topographic images of the scanning area which are also called constant current images. The exponential dependence of I on the tunneling distance allows to measure height differences of the order of 1 pm. Furthermore, this dependence causes a very high lateral resolution since most of the current flows via the foremost atom.

According to Eqn. 2.1 the interpretation of constant current images as topographic images is valid without any restrictions only if the main tip and sample properties, namely the density of states and work functions, are not changing within the scanning area. Section 2.4 will show how to get access to these sample properties.

2.2 The tunneling effect in one dimension

The principle of the quantum mechanical tunneling effect can be demonstrated by considering an one-dimensional rectangular potential barrier with a height of V_0 and a width of s as shown in Fig. 2.2. Outside the barrier the potential is assumed to be zero. In classical mechanics a particle of energy E cannot pass the potential barrier if $E < V_0$. This is different in the terms of quantum physics which has to be applied when the incoming particle is sufficiently small. For an incoming electron in the region I with $E < V_0$, there is a non-zero probability to penetrate into region III behind the barrier. For the one-dimensional case this transmission probability can be calculated analytically from the time-independent Schrödinger

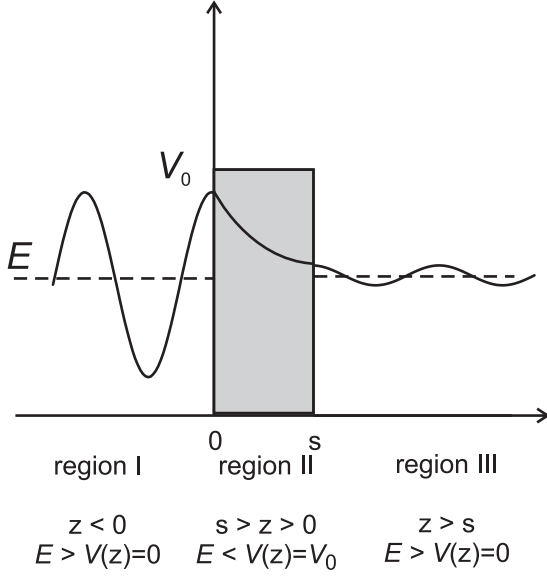


Figure 2.2: One-dimensional rectangular potential barrier with height V_0 and width s . Outside the barrier the potential is zero. E denotes the energy of an incoming (region I) electron. If the energy of the tunneling electron is conserved, the tunneling process is called elastic.

equation:

$$\left(-\frac{\hbar^2}{2m_e} \frac{d^2}{dz^2} + V(z) \right) \psi(z) = E \psi(z), \quad (2.4)$$

where ψ is the electron wave function. The solution of the wave functions of the electron in each region is given by:

$$\psi_{\text{I}} = e^{ikz} + \alpha e^{-ikz} \quad (2.5)$$

$$\psi_{\text{II}} = \beta e^{-\kappa z} + \gamma e^{\kappa z} \quad (2.6)$$

$$\psi_{\text{III}} = \delta e^{ikz} \quad (2.7)$$

with $k^2 = 2mE/\hbar^2$ and $\kappa^2 = 2m(V_0 - E)/\hbar^2$. As indicated in Fig. 2.2, outside the barrier the electron shows its oscillatory behavior, while inside the barrier an exponential decay takes place. With the given boundary conditions (the wave functions and their derivatives have to match at $z = 0$ and $z = s$) the coefficients α , β , γ , and δ can be derived. Therefore, it is possible to determine the transmission coefficient T , which is the ratio of the transmitted and the incident current density j_t and j_i . It is given by

$$T = \frac{j_t}{j_i} = |\delta|^2 = \frac{1}{1 + ((k^2 + \kappa^2)^2 / 4k^2\kappa^2) \sinh(\kappa s)} \quad (2.8)$$

and results in the limit of a strongly attenuating barrier ($\kappa s \gg 1$) in

$$T \approx \frac{16k^2\kappa^2}{(k^2 + \kappa^2)^2} \cdot e^{-2\kappa s}. \quad (2.9)$$

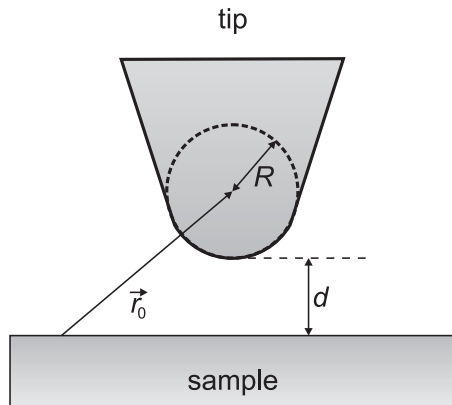


Figure 2.3: Geometry of the STM tip in the Tersoff-Hamann model. The tip has an arbitrary shape but a spherical geometry close to the surface with a radius R and distance d from the foremost end of the tip to the sample surface (taken from Ref. [17]).

In this derivation it was assumed that a tunneling electron possesses the same energy after passing the barrier as before. This case is called elastic tunneling. In realistic systems the energy of a tunneling electron can be lowered by so-called second order processes where energy is deposited, e.g. into the excitation of photons, phonons, or magnons. Since these processes are usually much less likely than elastic tunneling, they are neglected in this work.

Even though this model is too simple to describe realistic STM experiments, it demonstrates already the exponential dependence between the tunneling current and the tunnel distance.

2.3 Tersoff-Hamann-Model

In order to describe the tunneling between a conducting surface and a probe tip, Tersoff and Hamann developed an appropriate model, the so-called Tersoff-Hamann model (THM). Using the THM allows to deduce and extract fundamental sample properties from the measured tunneling current and from the measured differential conductance.

The THM is based on the work of Bardeen, who described the tunnel process within time-dependent perturbation theory for a planar metal-oxide-metal tunnel junction [18]. According to this approach the tunneling current between two weakly bounded electrodes, sample and tip, separated by a vacuum barrier, is given by:

$$I = \frac{2\pi e}{\hbar} \sum_{\mu,\nu} \{f(E_\mu^t) [1 - f(E_\nu^s + eU)] - f(E_\nu^s + eU) [1 - f(E_\mu^t)]\} \cdot |M_{\mu\nu}|^2 \cdot \delta(E_\mu^t - E_\nu^s), \quad (2.10)$$

where U is the applied bias voltage with respect to the sample. $M_{\mu\nu}$ is the tunneling matrix element between the state ψ_ν^s of the sample and ψ_μ^t of the tip.

E_ν^s and E_μ^t are the energy eigenvalues of the states ψ_ν^s and ψ_μ^t in the absence of tunneling. $f(E)$ is the Fermi-Dirac distribution.¹ The delta function describes the conservation of energy for the case of elastic tunneling. The tunneling matrix element is given by:

$$M_{\mu\nu} = \frac{\hbar^2}{2m_e} \cdot \int d\vec{S} \cdot \left(\psi_\mu^{t*} \vec{\nabla} \psi_\nu^s - \psi_\nu^s \vec{\nabla} \psi_\mu^{t*} \right). \quad (2.11)$$

where the integral has to be performed over any surface lying within the vacuum barrier. For low temperatures and small applied bias voltages Eqn. 2.10 reduces to

$$I = \frac{2\pi}{\hbar} e^2 U \cdot \sum_{\mu,\nu} |M_{\mu\nu}|^2 \cdot \delta(E_\nu^s - E_F) \cdot \delta(E_\mu^t - E_F), \quad (2.12)$$

where E_F is the Fermi level. But still it is too difficult to calculate the tunneling matrix in a general case. The THM overcomes this difficulty by assuming a simple model for the foremost atom of the tip with a locally spherical symmetry as displayed in Fig. 2.3. The tip state is assumed to be of s -type with orbital momentum $l = 0$. Within this approximation the tunneling matrix element can be calculated and the tunneling current is described by:

$$I \propto U \cdot \rho_t(E_F) \cdot \kappa^{-4} e^{2\kappa R} \cdot \sum_{\nu} |\psi_\nu^s(\vec{r}_0)|^2 \cdot \delta(E_\nu^s - E_F), \quad (2.13)$$

where $\kappa = \sqrt{2m\phi}/\hbar$ is the decay constant, ϕ is the work function which is assumed to be equal for tip and sample and \vec{r}_0 is the centre of the tip curvature. $\rho_t(E_F)$ is the local density of states (LDOS) of the tip at the Fermi level. The LDOS of the sample at the position of the tip and the Fermi level is given by:

$$\rho_s(\vec{r}_0, E_F) = \sum_{\nu} |\psi_\nu(\vec{r}_0)|^2 \cdot \delta(E_\nu^s - E_F). \quad (2.14)$$

Therefore, we can conclude for the tunneling current I in the case of small bias voltages and small temperatures:

$$I \propto U \cdot \rho_s(\vec{r}_0, E_F) \cdot \rho_t(E_F) \cdot e^{2\kappa R}. \quad (2.15)$$

Since the sample wave functions decay exponentially into the vacuum, it follows $\rho_s(\vec{r}_0, E_F) \propto \exp(-2\kappa(R+d))$. Thus the tunneling current depends also exponentially on the tip-sample distance in this model:

$$I \propto \exp(-2\kappa d). \quad (2.16)$$

Equation 2.15 already shows that constant current images can be interpreted as surfaces of constant sample density of states measured at the centre of the tip state and at E_F for small U and $T \approx 0$.

¹ $f(E) = (1 + \exp[E/k_B T])^{-1}$. k_B is the Boltzmann constant, T the temperature.

2.4 Scanning tunneling spectroscopy

For larger bias voltages an extension of the THM at $T = 0$ K results from Eqn. 2.10 by converting the sum into an integral over quasi continuum states. This results in:

$$I \propto \int_0^{eU} \rho_s(\vec{r}_0, E_F + \epsilon) \cdot \rho_t(E_F - eU + \epsilon) d\epsilon. \quad (2.17)$$

The sample LDOS at the centre of the tip state $\rho_s(\vec{r}_0, E)$ is related to the LDOS of the sample at the surface $\rho_s(E, x, y, z = 0) \equiv \rho_s(E)$ via the relation $\rho_s(\vec{r}_0, E) = \rho_s(E) \cdot T(E, U, s)$ with $s = R + d$ and a transmission coefficient $T(E, U, s)$. This leads to:

$$I \propto \int_0^{eU} \rho_s(E_F + \epsilon) \cdot \rho_t(E_F - eU + \epsilon) \cdot T(\epsilon, U, s) d\epsilon. \quad (2.18)$$

Using a semi-classical WKB²-approximation the transmission coefficient can be written as [14, 19]:

$$T(E, U, s) \cong \exp \left[-s \cdot \sqrt{\frac{4m_e}{\hbar^2} (\phi_t + \phi_s + eU - 2(E - E_{\parallel}))} \right]. \quad (2.19)$$

where ϕ_s and ϕ_t are the work functions of sample and tip. $E_{\parallel} = \hbar^2 k_{\parallel}^2 / (2m_e)$ is the component of the electron energy parallel to the surface, and \vec{k}_{\parallel} is the corresponding electron wave vector. $T(E, U, s)$ becomes minimal at certain energies that have a vanishing wave vector parallel to the surface ($k_{\parallel} = 0$). Thus, it is often concluded that the main contributions to I originate from states which are located at the centre of the surface Brillouin zone $\bar{\Gamma}$ and E_{\parallel} is neglected as in Eqn. 2.2. However, in Sec. 5.3.2 it will be shown that also states in the vicinity of $\bar{\Gamma}$ can play an important role.

The meaning of Eqns. 2.18 and 2.19 is demonstrated for a metallic tip and sample in Fig. 2.4. A constant LDOS is assumed for the tip, while the LDOS of the sample is assumed to exhibit some broad states. Without an applied bias voltage the Fermi levels of tip and sample are equal and different work functions ϕ_t and ϕ_s lead to a non-rectangular vacuum barrier as shown in Fig. 2.4(a). No net tunneling current is detectable. In Fig. 2.4(b) a negative bias voltage U is applied to the sample. Therefore, the energy levels of the sample are shifted upwards and electrons tunnel from an energy window $[0, eU]$ into the unoccupied states of the tip. The sign of the current is reversed when a positive voltage is applied as

²WKB denotes Wentzel, Kramers, and Brillouin.

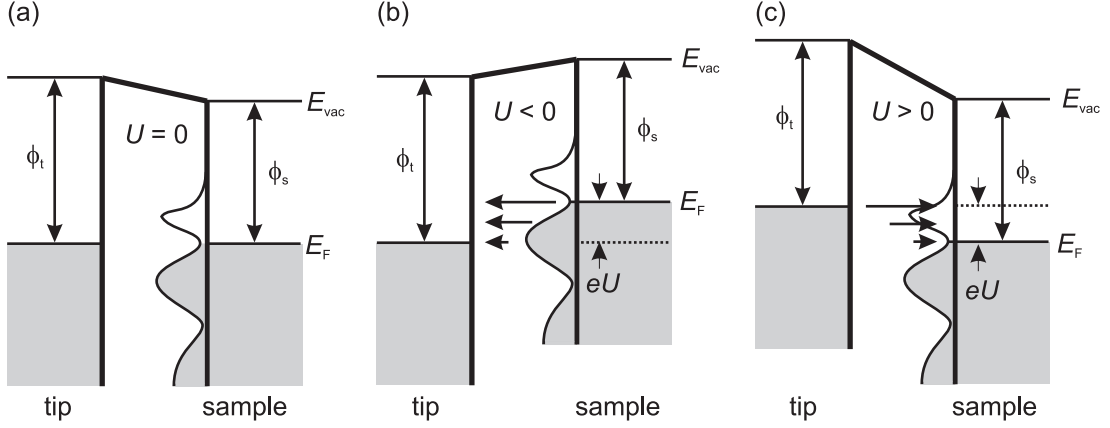


Figure 2.4: Tip and sample in tunnel contact. The energy-dependent sample density of states is sketched by the curve inside the barrier. A constant density of states is assumed for the tip. (a) Zero sample bias equilibrium: Tunneling current occurs only until the Fermi levels are equal. (b) Negative sample bias: Net tunneling current from sample to tip. (c) Positive sample bias: Net tunneling current from tip to sample. The length of the arrows indicate the different transmission coefficients due to the corresponding barrier height.

shown in (c). In Figs. 2.4(b) and (c) the indicated arrows of different size reflect the voltage dependence of the transmission coefficient: Electrons with a higher energy contribute more to I since the effective barrier height is smaller.

In order to obtain the sample LDOS, the first derivative of I in Eqn. 2.18 with respect to the bias voltage U is calculated, which results in the so-called differential conductance:

$$\begin{aligned}
 \frac{dI}{dU}(U, s) &\propto \rho_s(E_F + eU) \cdot \rho_t(E_F) \cdot T(eU, U, s) \\
 &+ \int_0^{eU} \rho_s(E_F + \epsilon) \cdot \rho_t(E_F + \epsilon - eU) \cdot \frac{d}{dU} T(\epsilon, U, s) d\epsilon \\
 &+ \int_0^{eU} \rho_s(E_F + \epsilon) \cdot T(\epsilon, U, s) \cdot \frac{d}{dU} \rho_t(E_F + \epsilon - eU) d\epsilon. \quad (2.20)
 \end{aligned}$$

The first term contains the sample LDOS $\rho_s(E_F + eU)$ at the applied bias voltage. The second and third terms are often neglected, assuming a constant LDOS of the tip ρ_t and weak dependence of T on U at small bias voltages. Thus, Eqn. 2.20

can be simplified to:

$$\frac{dI}{dU}(U, s) \propto \rho_s(E_F + eU) \cdot \rho_t(E_F) \cdot T(eU, U, s) . \quad (2.21)$$

Hence, the differential conductance dI/dU which can be directly measured by lock-in technique gives an access to the energy resolved sample LDOS.

All these results are only valid by assuming that the temperature of tip and sample is nearly zero. A non-zero temperature leads to thermal broadening, which is important to consider even at very low temperatures as will be shown in Chap. 3. Additionally, the amplitude of the modulation voltage U_{mod} , which is used to measure directly $dI/dU(U, s)$ by the lock-in technique, deteriorates the so-called energy resolution ΔE of the experiment. Taking into account thermal broadening and the modulation voltage, ΔE is given by [20, 21]:

$$\Delta E = \sqrt{\Delta E_{\text{therm}}^2 + \Delta E_{\text{mod}}^2} = \sqrt{(3k_B T)^2 + (2.5 \cdot eU_{\text{mod}})^2} . \quad (2.22)$$

Consequently, features in the sample LDOS which have a width of less than the energy resolution ΔE are hardly detectable by STS. In order to increase ΔE , both temperature and U_{mod} have to be decreased as low as possible. For the facility described in Chap. 3 the limit of ΔE is 100 μV . In Sec. 3.2.4 it will be shown how the energy resolution affects the STS measurements.

2.5 Spin-resolved STM/STS

Up to now the spin of the tunneling electrons was not considered in the theoretical concept for describing the tunneling current between tip and sample. All expressions for I and dI/dU were spin-averaged.

The influence of the spin on the tunneling current becomes obvious by considering tunneling between two spin-polarized electrodes as displayed in Fig. 2.5. The energy depending spin-polarization of each electrode is defined by

$$P(E) \equiv \frac{\rho_{\uparrow}(E) - \rho_{\downarrow}(E)}{\rho_{\uparrow}(E) + \rho_{\downarrow}(E)} . \quad (2.23)$$

where $\rho_{\uparrow}(E)$ and $\rho_{\downarrow}(E)$ denote the density of states of the majority and minority electrons, respectively. The indicated shift in energy of both subbands, which show different spin orientations, reflects a simple model for ferromagnetism known as the Stoner-Wohlfarth model. In this model one subband is shifted upwards, the other is shifted downwards due to exchange interaction. Thus, the numbers of electrons exhibiting a particular spin are different which leads to a macroscopic magnetization. The electrons in the downward shifted band are called majority electrons, while those from the upward shifted band are called minority electrons.

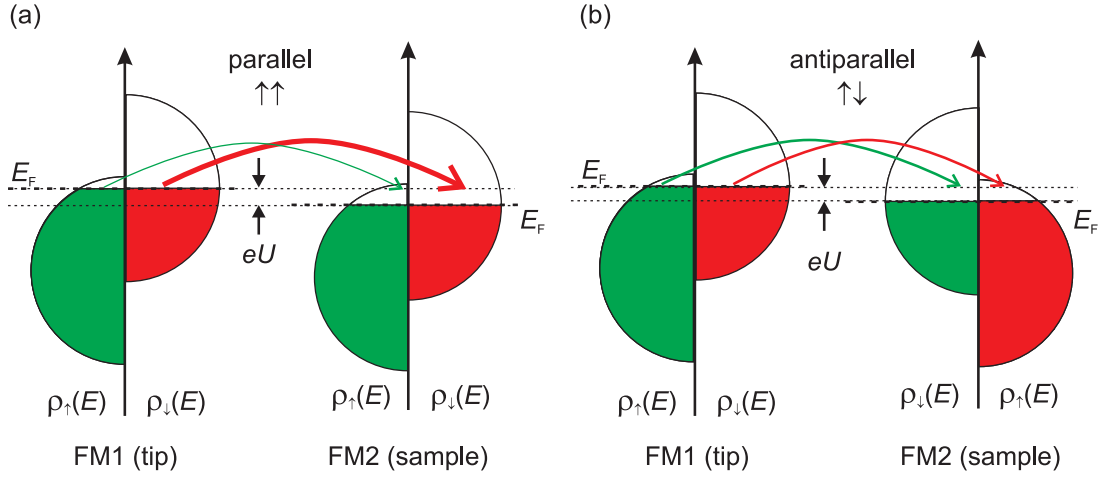


Figure 2.5: Principle of spin-polarized tunneling between two ferromagnetic electrodes (FM) with a parallel orientation of the magnetization in (a) and an antiparallel orientation in (b). The density of states of the majority (ρ_{\uparrow}) and minority (ρ_{\downarrow}) electrons is sketched. The color represents the absolute orientation of the spin: green is spin-up(\uparrow) and red is spin-down(\downarrow). For elastic tunneling and spin-conservation during tunneling the tunneling current in case (a) is different from that in case (b).

Figure 2.5 displays the electron transfer between two ferromagnetic electrodes, FM1 and FM2. The color represents the absolute spin orientation in the bands of each electrode. Since the spin of electrons is conserved during tunneling, spin-up and spin-down electrons of the left electrode tunnel solely into the corresponding unoccupied states of the right electrode. For the parallel magnetic configuration sketched in Fig. 2.5(a) majority and minority electrons of FM1 tunnel into unoccupied majority and minority states of FM2, respectively. In the antiparallel case in Fig. 2.5(b) majority electrons tunnel into unoccupied minority states and vice versa. A comparison of both total currents reveals that in this model the tunneling current for the antiparallel case is different. This shows exemplarily how the spin polarization of the electrodes, tip and sample, can influence the tunneling process.

For tunneling between two ferromagnetic planar tunnel junctions exhibiting arbitrary magnetic orientations \vec{M}_I and \vec{M}_{II} it was theoretically predicted and later experimentally verified that in the limit of free electrons and small bias voltages the tunnel conductance σ can be described by

$$\sigma = \sigma_0[1 + P_I(E)P_{II}(E) \cos \theta]. \quad (2.24)$$

$\theta(\vec{M}_I, \vec{M}_{II})$ denotes the angle between the magnetization orientation of both electrodes. Depending on θ the conductance σ varies around the spin-averaged value

σ_0 in a range which is given by the corresponding spin-polarizations P_{\uparrow} and P_{\downarrow} [22, 23].

In analogy to these results the previously introduced THM has been expanded in order to describe spin-polarized tunneling between tip and sample [24, 25]. Like for the spin-averaged case it is assumed that the majority (\uparrow) and minority (\downarrow) s -wave states of the tip can be characterized by the same decay constant κ . In addition, it is assumed that the majority and minority tip density of states $\rho_{\uparrow}^{\dagger}$ and $\rho_{\downarrow}^{\dagger}$ are constant in energy but different in size. This causes a non-zero spin polarization of the tip, $P_t = (\rho_{\uparrow}^{\dagger} - \rho_{\downarrow}^{\dagger})/\rho_t$ with $\rho_t = \rho_{\uparrow}^{\dagger} + \rho_{\downarrow}^{\dagger}$. The total tunneling current I , which consists of a spin-averaged (sa) and a spin-polarized (sp) part, can be written as

$$I(\vec{r}_0, U, \theta) = I(\vec{r}_0, U)_{\text{sa}} + I(\vec{r}_0, U, \theta)_{\text{sp}}, \quad (2.25)$$

where $\theta(\vec{r}_0)$ now denotes the angle between the fixed magnetization direction of the tip and the local sample magnetization $\vec{M}_s(\vec{r}_0)$.

In the case of small bias voltages U and neglecting any spin-flip processes the tunneling current is given by

$$I(\vec{r}_0, U, \theta(\vec{r}_0)) \propto \rho_t \cdot \tilde{\rho}_s(\vec{r}_0, U) \left(1 + P_t \tilde{P}_s(\vec{r}_0, U) \cos \theta(\vec{r}_0) \right), \quad (2.26)$$

with

$$\tilde{\rho}_s(\vec{r}_0, U) = \int_0^{eU} (\rho_s^{\uparrow}(\vec{r}_0, E_F + \epsilon) + \rho_s^{\downarrow}(\vec{r}_0, E_F + \epsilon)) d\epsilon \quad \text{and} \quad (2.27)$$

$$\tilde{P}_s(\vec{r}_0, U) = \left(\int_0^{eU} (\rho_s^{\uparrow}(\vec{r}_0, E_F + \epsilon) - \rho_s^{\downarrow}(\vec{r}_0, E_F + \epsilon)) d\epsilon \right) / \tilde{\rho}_s(\vec{r}_0, U). \quad (2.28)$$

$\tilde{\rho}_s(\vec{r}_0, U)$ describes the energy-integrated and spin-averaged density of states, while $\tilde{P}_s(\vec{r}_0, U)$ describes the energy-integrated local spin polarization of the sample. Thus, the first summand in Eqn. 2.26 contains the spin-averaged part, which is analogous to Eqn. 2.17. The second summand describes the influence of a non-zero tip and sample spin polarization on the tunneling current. Consequently, the complete information on the magnetic structure of the sample is already contained in constant current images. Nevertheless, the topographic mode is most of the time not used because height differences, which are caused by a laterally changing sample magnetization, are hardly distinguishable from other contributions to the topographic image of the sample.

A way to circumvent this problem is the use of spin-resolved STS. In analogy to the tunneling current also the differential conductance dI/dU can be separated into a spin-averaged and a spin-polarized part:

$$\frac{dI}{dU}(\vec{r}_0, U, \theta(\vec{r}_0)) \propto \frac{dI}{dU}_{\text{sa}}(\vec{r}_0, U) \cdot \left(1 + P_t \cdot P_s(\vec{r}_0, E_F + eU) \cos \theta(\vec{r}_0) \right). \quad (2.29)$$

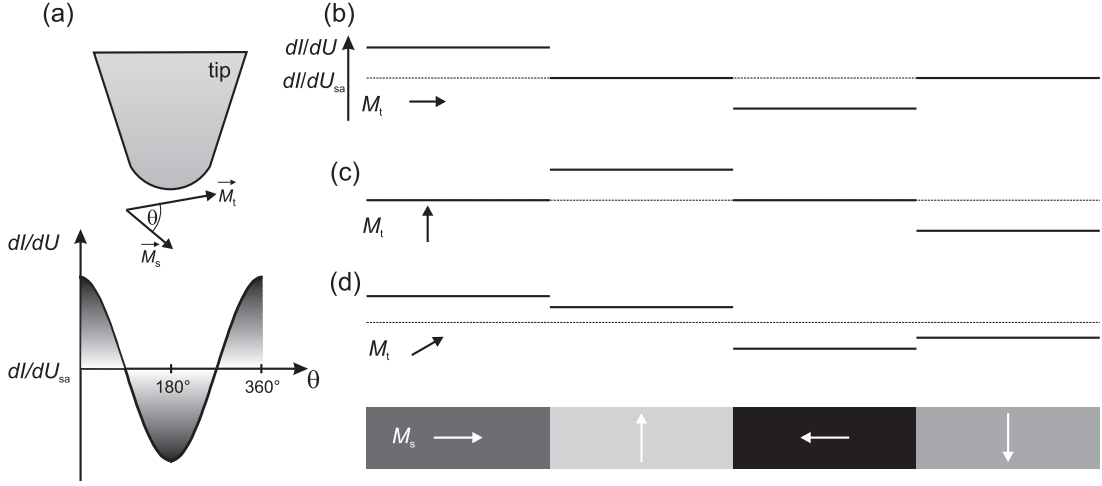


Figure 2.6: (a) Angular dependence of the total dI/dU signal on the tip and sample magnetization. dI/dU_{sa} denotes the spin-averaged differential conductance. (b)–(d) Response of dI/dU to a sample with locally different magnetic orientation by assuming an electronically homogeneous surface. Due to the canted magnetization of the tip in (d) dI/dU is sensitive to the in-plane as well as to the out-of-plane orientation of the sample.

Here $P_s(\vec{r}_0, U)$ denotes the energy-resolved local spin polarization of the sample. It has to be noticed, that usually the density of states as well as the spin-polarization of the tip are energy-dependent which is not considered in Eqn. 2.29. In the case of such an energy dependence, especially for negative bias voltages, integrals analogous to Eqn. 2.20 have to be included. The advantage of Eqn. 2.29 in comparison to Eqn. 2.26 in revealing differences due to a laterally changing sample magnetization is given by the fact that bias voltages can be chosen in order to maximize the magnetic contrast. Therefore, it is possible to separate the magnetic information from the topographic information.

Figure 2.6 shows how the local sample magnetization can be imaged by spin-resolved STS in the case of different tip magnetizations and for an electronically homogeneous sample. Figure 2.6(a) shows the angular dependence of the spin-polarized contribution to the differential conductance according to Eqn. 2.29. Figures 2.6(b)–(d) display the measured differential conductance above a sample which shows a laterally inhomogeneous magnetic configuration with two out-of-plane domains and two in-plane domains. The measured differential conductance reflects the local configuration of the tip and sample magnetization. In Figs. 2.6(b) and (c) the tip has a magnetization direction pointing in-plane and out-of-plane, respectively. Only three different levels of dI/dU intensity are observable. In

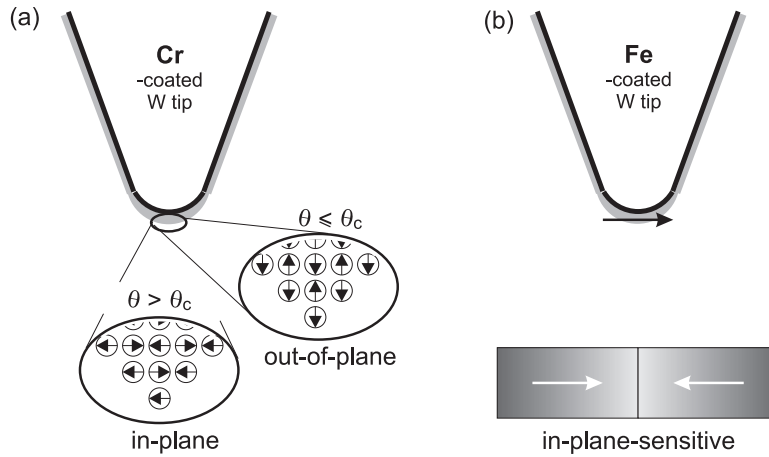


Figure 2.7: (a) Magnetic sensitivity of Cr-coated W tips. Tips with a Cr-coverage below $\theta_c = 45$ AL are sensitive to the out-of-plane component of the sample magnetization while tips with a coverage above tend to exhibit an in-plane sensitivity. (b) The magnetic sensitivity of Fe-coated W tips is usually in-plane.

Fig. 2.6 (d) all four magnetic domains of the sample magnetization can be resolved due to a canted tip magnetization. Therefore, the tip is sensitive to the in-plane as well as to the out-of-plane components of the sample magnetization.

One should point out that it is not possible to draw a conclusion concerning the orientation of magnetic moment of tip and sample from the observation of a magnetic contrast alone. Whether a higher or a lower intensity in the dI/dU signal corresponds to a parallel or antiparallel configuration of tip and sample magnetization can only be proven by applying an external magnetic field. In the following it will be shown how a coating of magnetic sensitive STM tips by different ferromagnetic and antiferromagnetic films can be used to adjust the sensitivity to in-plane or out-of-plane directions.

2.6 Tip preparation

All STM tips used in this thesis are etched electrochemically from polycrystalline tungsten (W) wire except for the Nb tip used in Sec. 3.2.4. The advantage of using W wires is that the standard preparation results in well-defined sharp and stable tips. Additionally, these tips are outstandingly qualified for coating by ferromagnetic or antiferromagnetic materials in order to obtain spin-sensitive tips.

The standard preparation starts with using sodium hydroxide (2M NaOH) for electrochemically etching the W wire which has a diameter of 0.3–0.9 mm. Before clamping the W tip into the tip holder (see Fig. 3.4) and both into the tip shuttle,

it is cleaned with distilled water. After inserting it into the load lock of the UHV system the tip shuttle with the tip is transferred to one of the side chambers where the electron bombardment takes place. During this procedure the tip and the shuttle is heated up to $T \geq 2000$ K for a couple of seconds (so-called *flashing*).³ This temperature is sufficient to remove any contamination as well as the oxide film covering the tungsten tip. After mounting the tip into the STM the state of the tip is probed by performing STM and STS measurements on clean W(110) surfaces. The W(110) substrate is cleaned as described in Sec. 3.2.5. If the obtained images exhibit experimental artefacts which let conclude that the tip is blunt or shows a so-called multiple-tip, the tip is pulsed. For pulsing, a tunneling current of up to 10 nA is applied with voltage pulses of up to 10 V for approximately one second. This results in a lost of material and/or touches of tip and sample. Both procedures lead consequently to a change of the tip apex. This treatment is repeated until the tip fulfills the requirements concerning sharpness and stability.

For the spin-resolved measurements clean W tips are coated with thin films of antiferromagnetic (Cr) or ferromagnetic (Fe) materials [13]. The ferromagnetic or antiferromagnetic coating takes place right after flashing the tip, which provides a clean tip surface and therefore defined growth conditions of the magnetic material. Afterwards the coated tip is annealed at 500 K. It is known that the magnetic sensitivity of Cr-coated tips shows a transition depending on the thickness of the Cr film as displayed in Fig. 2.7(a) [26]. Cr tips with a coverage below 45 atomic layers (AL) are sensitive to the out-of-plane component of the sample magnetization while tips with a coverage above 45 AL tend to exhibit an in-plane sensitivity. In the study shown in Chap. 5 the Cr coverage is 15–20 AL, which results in out-of-plane sensitive tips. But sometimes also Cr tips with a high nominal Cr-coverage (90 AL) were found to show a strong out-of-plane contrast as will be shown in Sec. 3.2.5. Fe-coated tips with an Fe-coverage of around 10 AL are usually magnetized in the surface plane as shown in Fig. 2.7(b) [13]. Anyhow, the Fe-coated tip with a coverage of 10–15 AL used in Chap. 5 also showed an out-of-plane component of the magnetization. Using Fe-coated tips can be advantageous due to a higher spin polarization of the electronic states compared to Cr-coated tips yielding a higher magnetic contrast in dI/dU maps. On the other hand, due to their antiferromagnetic configuration Cr tips do not show stray fields and thus have no influence on the magnetic state of the sample.

³In order to avoid melting of the tip holder as well as of the tip shuttle both are made of molybdenum. ($T_{\text{melt}}^{\text{Mo}} \approx 2900$ K, $T_{\text{melt}}^{\text{W}} \approx 3700$ K)

2.7 Measurement modes

Topographic images

All images presented in this work which are referred to *topographic images* have been recorded in the constant current mode. In this mode the feedback keeps the value of the integral in Eqn. 2.18, i.e. the tunneling current, by varying the tip-sample distance at each point of the image as explained in Sec. 2.1. Since the electronic structure of the sample can also spatially vary not all height regulations are due to local changes of the sample topography. A pure topographic image is only obtained for a chemically, electronically, and magnetically (in the case of SP-STM) homogeneous surface. In this work it will be shown that such inhomogeneities result in small height variations of a only few ten pm. This is small in comparison to topographic changes such as monolayer high step edges exhibiting heights of up to 3 Å.

Spectroscopy fields

To obtain information about the electronic structure of the sample the differential conductance $dI/dU(U)$ signal is measured, which is closely related to the LDOS of the sample according to Eqns. 2.21 and 2.29. In order to perform such a measurement the tip is first stabilized at U_{stab} and I_{stab} . Then the feedback is deactivated, the voltage is swept to a final value and $I(U)$ as well as $dI/dU(U)$ are recorded. The $dI/dU(U)$ spectra are obtained by using lock-in technique where a small *ac* modulation voltage U_{mod} with frequencies in the range of 1 kHz to 4 kHz is added to U . Depending on the required energy resolution the modulation voltage U_{mod} varies from 25 μV to several tens of a mV. This can be done for each image point thus achieving $dI/dU(U)$ spectra with high lateral resolution, or so-called full spectroscopy fields. In addition, topographic images are recorded simultaneously which allows a direct correlation of the topographic and spectroscopic properties of the sample. In this thesis the spatially resolved dI/dU signal at a fixed bias voltage extracted from a full spectroscopy field is called dI/dU slice.

The topographic images, which are recorded simultaneously, allow to evaluate whether different tip-sample distances z are adjusted to obtain the same value for I_{stab} at each image point. Different $z(x, y)$ values due to a laterally changing electronic structure or work function lead consequently to laterally changing transmission coefficients which affects the comparability of the measured $dI/dU(U, x, y)$ spectra. In order to overcome this problem the measured $dI/dU(U)$ spectra can be normalized using the decay constant $\kappa(U)$ which can be determined from the slope by plotting $\ln(I(z))$ versus z .

The normalized $dI/dU(U)$ spectra are then given by

$$dI/dU_{\text{norm}}(U, x, y) = dI/dU_{\text{meas}}(U, x, y) \cdot e^{2\kappa(U)z(x,y)}. \quad (2.30)$$

Any normalization of the measurements shown in this thesis will be discussed where necessary.

dI/dU maps

A less time-consuming method to get access to the electronic properties of the sample is the measurement of so-called *dI/dU* maps at a fixed bias voltage. In contrast to *dI/dU* spectra, *dI/dU* maps are obtained by recording the *dI/dU* signal via lock-in technique simultaneously to constant-current images with a closed feedback loop. There are two disadvantages of this method in comparison to spectroscopy fields. First, *dI/dU* maps acquired at different bias voltages are usually obtained at different tip-sample distances. This complicates the comparison of *dI/dU* maps at different energies. Second, while for recording a spectroscopy field it is possible to choose a stabilization voltage where the topographic contribution is sufficiently small, this is not possible for *dI/dU* maps. The main advantage of this method is that the data can be recorded with high spatial resolution in a short time. This is in particular advantageous in the case of SP-STM when imaging magnetic domains. As shown in Sec. 2.5 the use of magnetic tips allows for the measurement of the spin-resolved *dI/dU* signal, which depends on the scalar product of tip and sample magnetization. Thereby, any differences in spin-resolved *dI/dU* signals observed for structures exhibiting the same spin-averaged electronic structure are due to a different relative alignment of the tip and sample magnetization vectors as displayed in Fig. 2.6. In this thesis the appearance of these differences in spin-resolved *dI/dU* maps is called magnetic contrast.

3 Instrumentation

The unique power of spin-resolved scanning tunneling spectroscopy (SP-STs) is its ability to give direct access to the spin-resolved local density of states (LDOS) of the electron system of conducting solid surfaces with a high spatial and energy resolution. The high spatial resolution is basically guaranteed by the working principle of an STM for all temperatures. A high energy resolution requires low temperature systems.

This chapter gives an overview of the setup and the properties of the ultra-high vacuum (UHV) STM system with a 14 T magnet operating at liquid ^3He temperatures which was used for the measurements on the Pt(111) surface (Chap. 4) as well as for the investigations on the single Co atoms on Pt(111) (Chap. 6). In the present thesis UHV conditions are defined by a base pressure below 1×10^{-10} mbar for the whole UHV system. They are absolutely required to guarantee clean and well-defined samples as well as tips and the reproducibility of their preparation, in particular for SP-STs measurements and single atoms as studied in Chap. 6. A high magnetic field is an important experimental parameter to manipulate the magnetic state of the investigated sample systems.

Originally the facility has been designed and set up by J. Wiebe and A. Wachowiak [21, 27]. In the first phase of my work the setup of the system has been completed and the operation of the facility has been started. Some serious technical problems required an improvement of the technical realization in some aspects regarding the cryostat delivered from *Oxford Instruments Superconductivity* [28]. This is described in Sec. 3.1. Section 3.2 shows the excellent results of the characterization measurements, which have been performed in this thesis, concerning the stability of the STM, the energy resolution, and the spin resolution at base temperature. A detailed description of the system is given in Ref [29].

3.1 Setup

Figure 3.1 gives an overview of the facility. The main part of the system is a ^3He evaporation refrigerator in a bottom loading cryostat which was designed and built by *Oxford Instruments Superconductivity*. It contains a superconducting single coil magnet and the low temperature STM. In order to achieve an effective mechanical decoupling from the building and thus from the main vibrational noise sources, a three stage damping system is used. First, the cryostat itself is embedded in a

sand-filled aluminum barrel which rests on three supports. Second, the supports themselves rest on air springs. Third, they are supported on a sand layer having a depth of 1 m which is kept within the supporting legs. The whole facility rests on the foundation in the basement of the building. The performed test measurements shown in Sec. 3.2.3 will reveal that all stages of the damping concept decouple the facility from external noise sources very effectively.

The bottom flange of the cryostat is connected to a home-built three chamber UHV-system. After baking the system including a UHV tube inside the cryostat for about one week at temperatures of 110°C–150°C, each chamber exhibits a base pressure of $p < 1 \cdot 10^{-10}$ mbar, even with the cryostat kept at room temperature. In the central UHV chamber, STM tips and samples can be stored and transferred into and out of the STM. From there they are transported between the chambers by means of magnetic drives and wobblesticks. In addition a molecular beam evaporator is mounted onto the central chamber. Since this evaporator can be separated from the chamber by a valve and thus baked-out independently, it is possible to exchange the evaporator material without breaking the vacuum of the system. The second UHV chamber contains a molecular beam evaporator, a room-temperature STM for an easy and fast sample characterization as well as a combined LEED/Auger-electron¹ spectroscopy unit. The third UHV chamber contains an ion source for sputtering, a gas inlet for dosage of different gases, several metal beam evaporators, a quadrupole mass spectrometer, and a home-built electron bombardment heater for tips and samples with $T_{\max} > 2400$ K assembled on an x,y,z-manipulator. Finally, it contains a home-built variable-temperature MOKE² setup for the characterization of the spatially averaged magnetic properties of thin film samples [30]. By means of a load lock, tips and samples are easily transferred into the system without breaking the UHV in the main chambers.

Figure 3.2 shows a section through the cryostat. The STM and the ³He refrigerator can be moved over a distance of 500 mm in the UHV tube by an external motor drive. The UHV tube itself extends from the electrical feedthroughs at the top of the cryostat to the bottom flange. The motor drive turns a threaded leadscrew via a rotary feedthrough. By this mechanism the STM can be moved from the fully retracted position, which is the measuring position, to the fully extended position inside the central UHV chamber as shown in Fig. 3.2. There, tips and samples can be exchanged. Additionally, in this position it is possible to evaporate material from the molecular beam evaporator onto the cold surface as described in Chap. 6. In the fully retracted position the STM can be cooled down to base temperature. A superconducting solenoid, which is placed in the liquid ⁴He dewar, can provide a maximum magnetic field of 12 T perpendicular to the sample surface. A lambda fridge can be used to cool the magnet to 2.2 K in order to achieve a field of 14 T. For additional thermal insulation of the cryostat

¹LEED stands for low energy electron diffraction.

²MOKE is an acronym for magneto-optical Kerr effect.

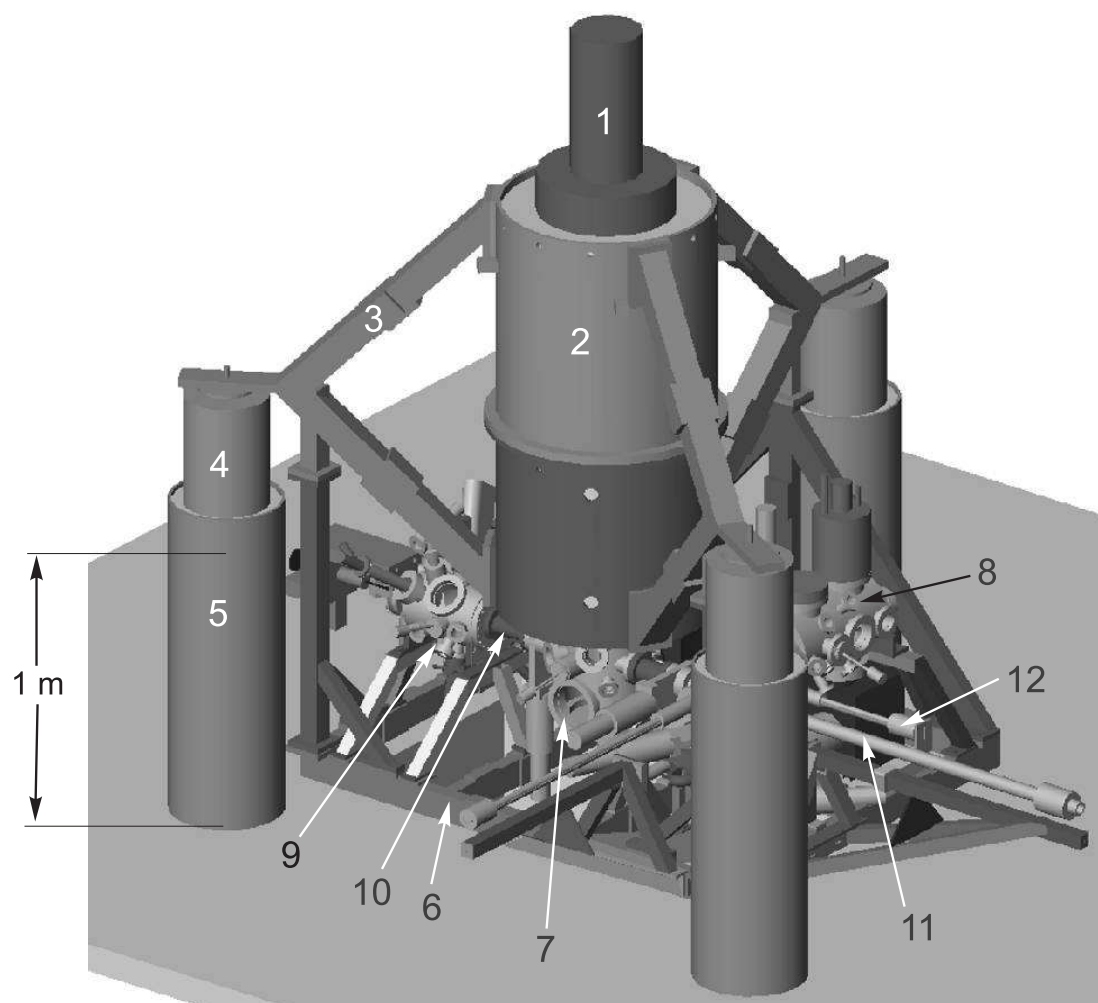


Figure 3.1: Overview of the facility. (1) Bottom loading cryostat containing the ^3He refrigerator, the low temperature STM and the superconducting single coil magnet. (2) Sand-filled aluminum barrel, (3) stainless-steel supports, (4) air springs, (5) sand-filled supporting legs, (6) sand-filled stainless-steel frame mounted to the supports (3), (7) central UHV chamber for sample and tip exchange from the low temperature STM; it contains a molecular beam evaporator for evaporating on cold surfaces, (8) second UHV chamber containing a room temperature STM, molecular beam evaporators and a combined LEED/Auger-system, (9) third UHV chamber containing a variable-temperature MOKE-setup, the tip- and sample heater, molecular beam evaporators and an ion source, (10) edge-welded bellows, (11) magnetic linear and rotary motion drives, (12) load lock.

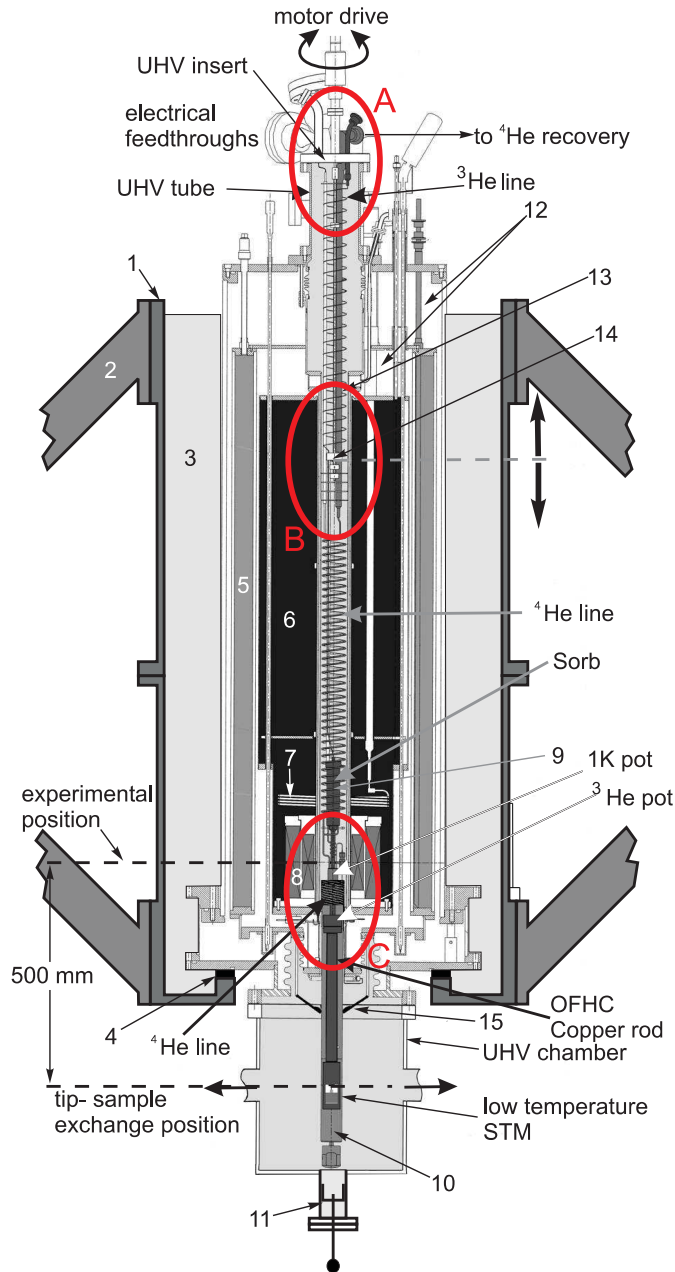


Figure 3.2: The bottom loading cryostat with the ^3He refrigerator. The UHV insert is shown in the fully extended position with the STM moved into the UHV chamber for tip or sample exchange and material deposition onto cold surfaces. (1) Aluminum barrel, (2) stainless-steel supports, (3) sand, (4) rubber ring, (5) liquid nitrogen bath, (6) ^4He dewar, (7) lambda fridge, (8) 12/14 T magnet, (9) single-shot ^3He refrigerator, (10) radiation shield, (11) UHV rotary feedthrough for opening the radiation shield (10), (12) super-insulation vacuum, (13) threaded leadscrew, (14) aluminum-bronze nut, (15) radiation flaps at 77 K.

the ^4He dewar is surrounded by a super-insulation vacuum and a liquid nitrogen dewar.

The cooling of the STM is provided by a ^3He refrigerator. It consists of a vibrationless charcoal sorption pump (also called sorb) which is connected to the ^3He pot via a pumping line that passes through the so-called 1K pot. The charcoal pump adsorbs or desorbs the ^3He gas while being cooled below 20 K or heated to 40 K, respectively. The STM is attached to the ^3He pot via an OFHC-copper

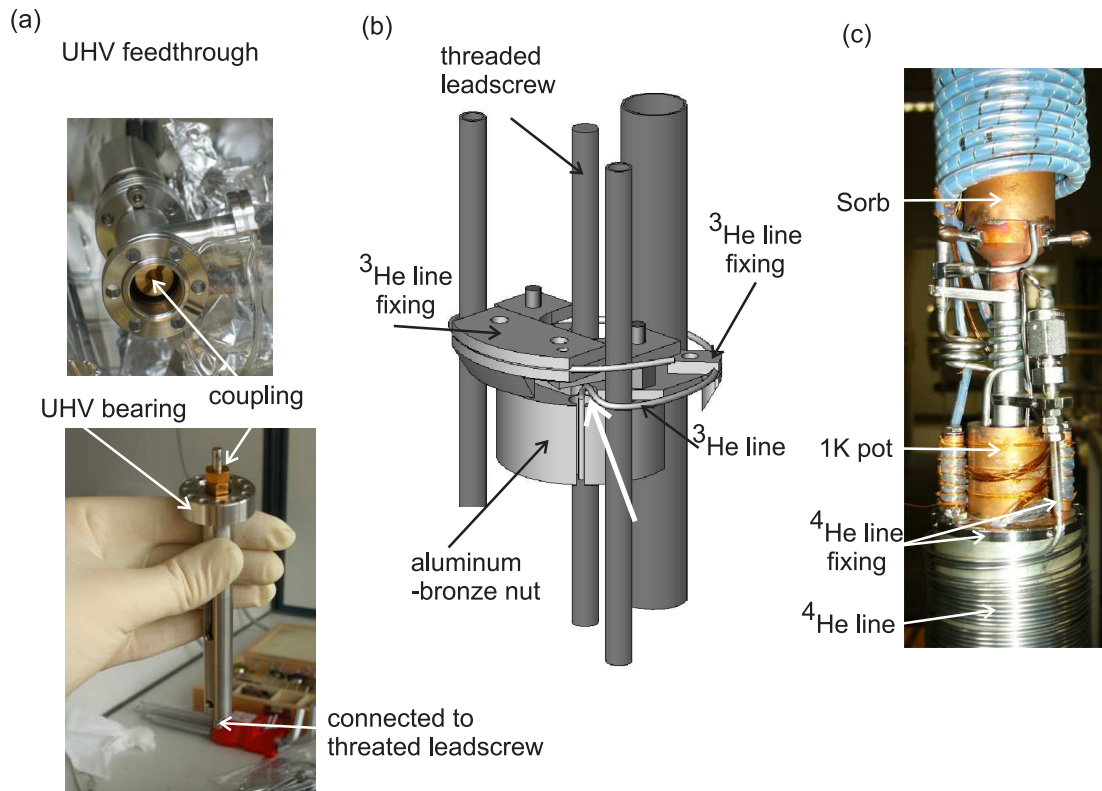


Figure 3.3: (a) UHV bearing which replaced the original UHV feedthrough set-up. (b) Schematic drawing of the mounted ^3He line fixing for releasing the soldering position (see white arrow). (c) ^4He line fixing in order to avoid catching of the ^4He line by the 1K pot.

rod which provides a very good thermal connection (see Sec. 3.2.2). A capillary from the ^4He dewar to the ^4He recovery line (^4He line) outside the facility is connected to the sorb as well as to the 1K pot. Therefore, both can be cooled to $< 4\text{K}$ by pumping the capillary which causes a continuous flow of ^4He to the sorb as well as to the 1K pot. Without pumping this capillary the 1K pot stays at temperatures around 4.2K . Furthermore, the 1K pot is attached to a thermal radiation shield which protects the ^3He pot and the STM from heat radiation. Thus, the temperature of the 1K pot influences the temperature of the STM weakly (see Sec. 3.2.2).

Technical improvements

The ellipses labelled by A,B, and C in Fig. 3.2 indicate parts of the original UHV-insert setup which caused serious technical problems. First, the UHV rotary feedthrough (A) was overloaded by carrying the total weight of the UHV insert. The occurring mechanical overload lead to an early abrasion of the feedthrough

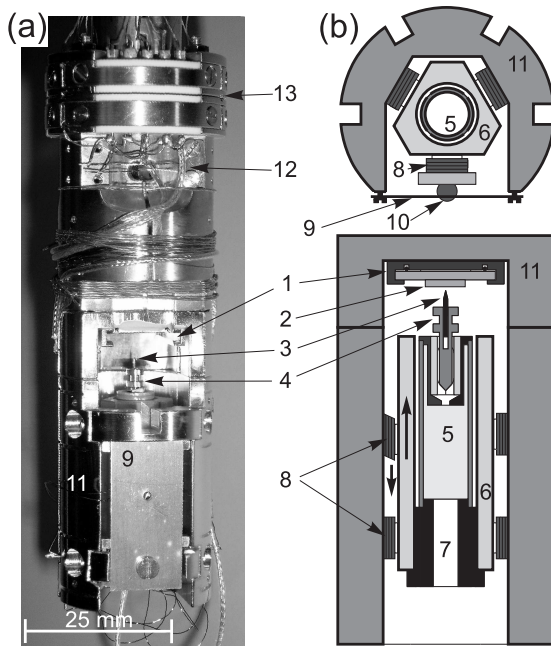


Figure 3.4: (a) Photo of the STM head. (b) Horizontal (top) and vertical (bottom) cross sections. (1) Sample holder, (2) sample, (3) tip, (4) tip holder (molybdenum), (5) tube scanner, (6) sapphire prism, (7) tube scanner holder (marmor), (8) shear-piezo stacks, (9) molybdenum leaf-spring, (10) titanium ball, (11) microscope body (phosphorous bronze), (12) Cernox temperature sensor, (13) electrical connector (OFHC copper).

which thus prohibited the travelling of the insert and thus of the STM. This problem had been overcome by mounting an additional UHV bearing between a new magnetically coupled rotary feedthrough and the threaded leadscrew as displayed in Fig. 3.3(a). Thus the weight of the insert rests on the flange of the bearing and the rotary feedthrough only provides the turning of the leadscrew. The second problem (B) was a leak in the ^3He line. As shown in Fig. 3.3(b) the flexible ^3He line passes the aluminum-bronze nut, which travels along the leadscrew. An overstress at the position marked by the white arrow caused a ^3He leak, which required soft soldering at the affected position. To avoid further weakening of this position, a ^3He line fixing had been mounted. Finally at position (C), the flexible ^4He line (see Fig. 3.3(c)) got caught by the 1K pot. This required a replacement of the line and the setup of a simple fixing, which avoids such catching effectively.

After healing these teething troubles, now the system exceeds all our expectations which is emphasized by the results obtained at low temperatures as shown in Sec. 3.2.

STM head

Figure 3.4(a) shows a photo of the home-built STM head. It has been designed to be as small and compact as possible in order to make it less susceptible against vibrations. The gold plated microscope body is made of phosphorous bronze, a hard, nonmagnetic, and UHV-compatible copper alloy and includes the coarse approach motor, which is of the so-called Walker design [31], as well as the tube

scanner. Figure 3.4(b) shows two schematic cross sections of the STM. This provides a view of the coarse approach motor consisting of a sapphire prism, which is clamped between six shear piezo stacks. Operating the piezo motor in the so-called stick-slip mode, the tip can be approached to the sample until the tunneling distance is reached [32]. The tube scanner, which is mounted within the sapphire prism, provides the (x,y,z) -movement of the tip during the measurement. The maximal scan range in the (x,y) -plane is $1 \times 1 \mu m^2$ with applied voltages of ± 240 V and the z -range is about 200 nm at base temperature.

Because of the achievable magnetic fields of up to 12 (14) T, it is important to avoid any magnetic materials for the set up of the STM. The right choice of materials is not trivial since even non-ferromagnetic materials can exhibit a very high paramagnetic or diamagnetic susceptibility at temperatures below 1 K, which leads to a reasonable interaction with the external field. Since the present setup of the ^3He refrigerator requires a small bellow between the sorb and the ^3He pot, already small forces lead to a displacement of the STM which can result in a touching of the STM and the radiation shield which causes vibrational noise and a temperature increase. This has been observed for the original setup of the STM when magnetic fields of more than 4 T were applied. The reason was found in a Ni wetting-layer between the STM body and the gold plating. Therefore, a new STM was set up without any Ni layers even for the shear- and tube scanner electrodes.³ The following will show that this improvement allows experiments in the presence of magnetic fields of up to 12 T.

3.2 Low temperature properties

3.2.1 Cooling procedure

A standard cooling down procedure of the ^3He pot as well as of the STM is as follows: After storing all ^3He gas in the sorb by cooling it below at least 20 K, the sorb is warmed to 45 K by heaters. This results in a ^3He gas pressure increase which activates a thermal switch between the ^3He pot and the 1K pot. Therefore, the ^3He pot is cooled down to 1K pot temperature. When the 1K pot temperature is below 2 K the ^3He gas is free to condense in the 1K pot region and fills the ^3He pot with liquid. In order to reach the base temperature, the sorb is cooled to approximately 7 K after the complete condensing. This reduces the vapor pressure above the liquid ^3He and deactivates the thermal switch. Thus, the temperature of the ^3He pot as well as of the STM drops to base temperature. When all the ^3He has been adsorbed by the sorb, the STM warms up to 4.2 K. In order to reach the base temperature again the liquid has to be recondensed by repeating the process, which takes typically less than 1 h. An additional feature of the system

³The new setup of the STM was done by Daniel Haude.

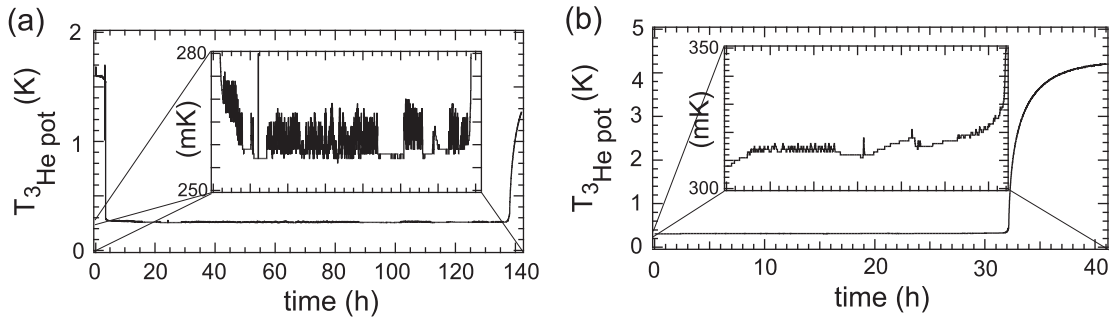


Figure 3.5: Temperature of the ^3He pot as a function of time. Typically the temperature of the STM is only 2–3 mK higher. (a) The 1K pot is cooled ($T_{1\text{Kpot}} < 2\text{ K}$) by pumping at the 1K pot. In this operation mode a base temperature of 262 ± 5 mK and a base temperature hold time of approximately 130 h are reached. (b) Without pumping at the 1K pot ($T_{1\text{Kpot}} = 4.2\text{ K}$). A base temperature of 315 ± 5 mK and a base temperature hold time of approximately 30 h are accomplished.

is the possibility to heat the ^3He pot and the sorption pump in order to achieve higher temperatures. Below 4 K the temperature of the STM is regulated by the temperature of the sorption pump. Above 4 K, the heat load is regulated by a resistive heater on the ^3He pot. Thereby, a wide temperature range from base temperature up to 100 K is accessible.

3.2.2 Base temperature hold time

Figure 3.5 shows the temperature run of the ^3He pot when the sorb cools the liquid ^3He . The temperature of the STM is only 2–3 mK higher than the temperature measured by the sensors at the ^3He pot. This indicates an excellent thermal coupling between the STM and the ^3He pot via the OFHC copper rod. Fig. 3.5(a) shows the temperature run while the temperature of the 1 K pot is below 2 K due to pumping the ^4He capillary. With a 3.51 (NTP)⁴ ^3He -gas charge that condenses into about 5 cm^3 of liquid the STM can be held at a base temperature of 262 ± 5 mK for 130 h. After this time the STM warms up and reaches a temperature which is close to the 1K pot temperature. Since this mode of operation causes additional vibrations probably due to turbulence arising from the ^4He injection into the 1K pot, the system is operated in a second mode where the 1K pot is not pumped and stays at around 4.2 K. For this mode Fig. 3.5(b) shows a slightly higher base temperature of 315 ± 5 mK with a decreased hold time of 30 h. Since this time period is usually sufficient for high-resolution STS measurements, all of the following results at base temperature were achieved in the second

⁴Normal Temperature and Pressure (NTP).

mode of operation. The difference of both base temperatures can be explained by taking into account the radiation shield which is connected to the 1K pot and surrounds the STM. An increase of the 1K pot temperature thus causes a higher heat radiation to the STM.

Another important time scale is given by the time it takes to reach the base temperature after exchanging tip or sample. Typically, such a procedure takes less than 4 h. During the tip and sample exchange the STM temperature stays below 35 K.

The system can also be operated at a stable temperature of 4.2 K without any temperature regulation. This is achieved when no ^3He is recondensed. Then the STM stays at 4.2 K and the temperature hold time is (practically) unlimited. The measuring time is only limited by the hold time of the ^4He dewar, which has to be refilled at least after 120 h.

3.2.3 z-stability

In order to specify the z-stability of the tunneling junction atomically clean and largely defect free (110) surfaces of InSb and InAs have been prepared by cleaving single crystals in the load lock and a fast transfer to the STM afterwards. Thus, these surfaces provide an ideal test system for the specification of the piezo-sensitivity and the z-stability. Figure 3.6(a) shows an atomically resolved topographic image of the InSb(110) surface obtained at 313 mK.⁵ It is known for the (110)-surfaces of III-V semiconductors that only one sort of atoms is imaged by STM in a certain voltage range while the other sort is invisible [33]. The two line sections taken perpendicular and parallel to the atomic rows are shown in Fig. 3.6(b). They exhibit an atomic corrugation of about 20 pm and 13 pm, respectively with a period given by the unit cell of one atomic sort. In both plots the z-noise level is below 3 pm. In order to demonstrate the performance in the presence of a magnetic field, an InAs(110) surface has been probed at 8 T which is imaged in Fig. 3.6(c). The sections in Fig. 3.6(d) along the lines marked in (c) show a lower corrugation than in Fig. 3.6(a), which is in particular visible for section 2. Though the corrugation along this line is tiny (<2 pm) the atoms are still resolved. This proves that applying the external magnetic field does not cause additional noise.

While the z-noise level was determined in the topography mode with a closed feedback loop, the following reveals the stability of the tunneling junction when the feedback is switched off. As described in Sec. 2.7 this is required for measuring $I(U)$ and dI/dU spectra.

Figure 3.7(a) shows the time dependency of the tunneling current measured at a single point on the InSb(110) surface, which was partly covered by Fe clusters. Originally, this measurement was performed to obtain information about charging

⁵All images in Fig. 3.6 show unfiltered raw data. Fig. 3.6(a) and (b) are plane and line fitted.

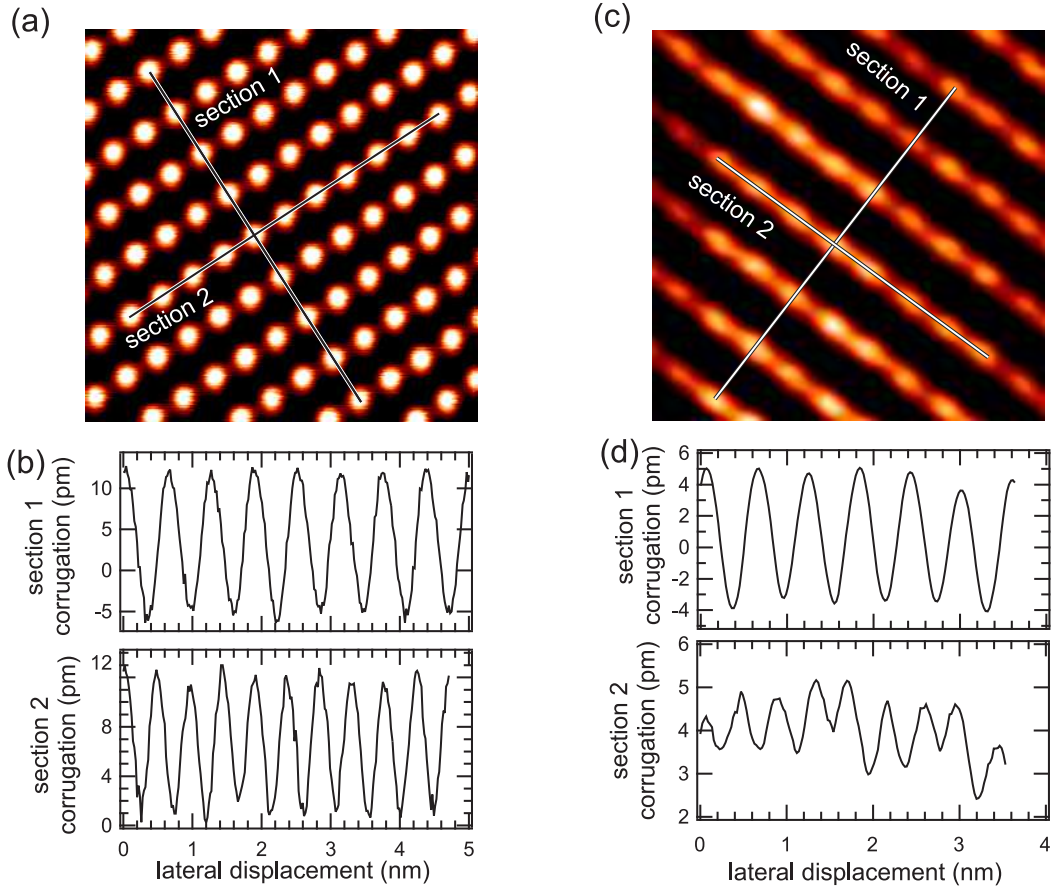


Figure 3.6: (a) Topographic image of the atomically resolved InSb(110) surface (unfiltered data, $U = 0.3$ V, $I = 0.8$ nA). (b) Line sections along the lines marked in (a). The atomic corrugations show a z-noise level below 3 pm. (c) Topographic image of the atomically resolved InAs(110) surface in a magnetic field of 8 T (unfiltered data, $U = +0.05$ V, $I = 0.2$ nA). (d) Line sections along the lines marked in (c). Both images have been recorded at 0.315 K.

effects in the sample which causes discrete jumps in the current. Therefore, the tip has been stabilized at $U_{\text{stab}}=1$ V and $I_{\text{stab}}=1$ nA. After switching off the feedback, the bias voltage was set to -0.95 V, which resulted in a current of about -41 pA. The current was measured for 400 s. The image consists of 2000×2000 data points and each row took 0.1 s. Due to the used data acquisition method there is a time gap of 0.1 s between neighboring rows. Thus, the indicated points A,B,C, and D correspond to $t=0.0$ s, $t=0.1$ s, $t=399.9$ s, and $t=400.0$ s. According to the color code of the image the dominating bright color reflects a current of around -40 pA while the mentioned jumps to a current of less than -150 pA are visible as black lines. Figure 3.7(b) displays sections along the first, the 820th, and the

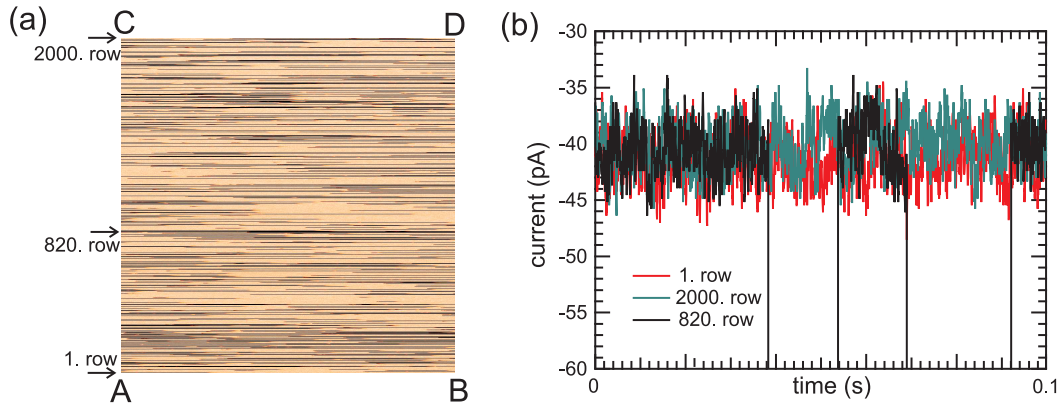


Figure 3.7: (a) Image of the time dependency of the tunneling current at a single point on Fe/InSb(110) without z-regulation (for A,B,C, and D see text). (b) Sections along the first, the 820th, and 2000th row in (a). The current jumps (black lines in (a)) are due to charging effects and not related to the stability of the system. Even though the feedback has been switched off for more than 6.5 min, the current has changed barely due to drift effects. The image has been recorded at 0.315 K.

last row of Fig. 3.7(a), corresponding to the time intervals 0.0–0.1 s, 163.9–164.0 s, and 399.9–400.0 s. Apart from the current jumps caused by charging, the current stays extremely constant over a time period of 400 s. By comparing the plots of the first and the last row we can extract that the average of each row changed from $I_1 = -41.6 \pm 2.1$ pA to $I_2 = -40.01 \pm 2.10$ pA. This corresponds to a current change of $(I_1 - I_2)/I_1 = 3.6\%$ in 400 s. Assuming a reasonable range for the averaged work function $(\Phi_s + \Phi_t)/2 = 1-3$ eV, this results in a z-change of 2–5 pm, according to Eqn. 2.3. Thus, the z-stability over a time period of 400 s, which is usually long enough to acquire a high energy resolved spectrum, is in the same range as the z-stability with an active feedback regulation.

3.2.4 Energy resolution

In order to demonstrate the high energy resolution of the facility, STS measurements on superconducting as well as metallic samples with metallic as well as superconducting tips were performed.

NbSe₂ was used for the superconducting sample, which is a type II superconductor with a superconducting phase transition at approximately $T_C = 7.2$ K [34]. Since it is a layered sample system it is easily cleaved in UHV in order to obtain a clean surface. Cleavage is achieved by an adhesive tape which is glued to the NbSe₂ surface as well as to the load-lock wall. When the sample is moved, the first layers, which were exposed to air, stick to the tape and the remaining sample

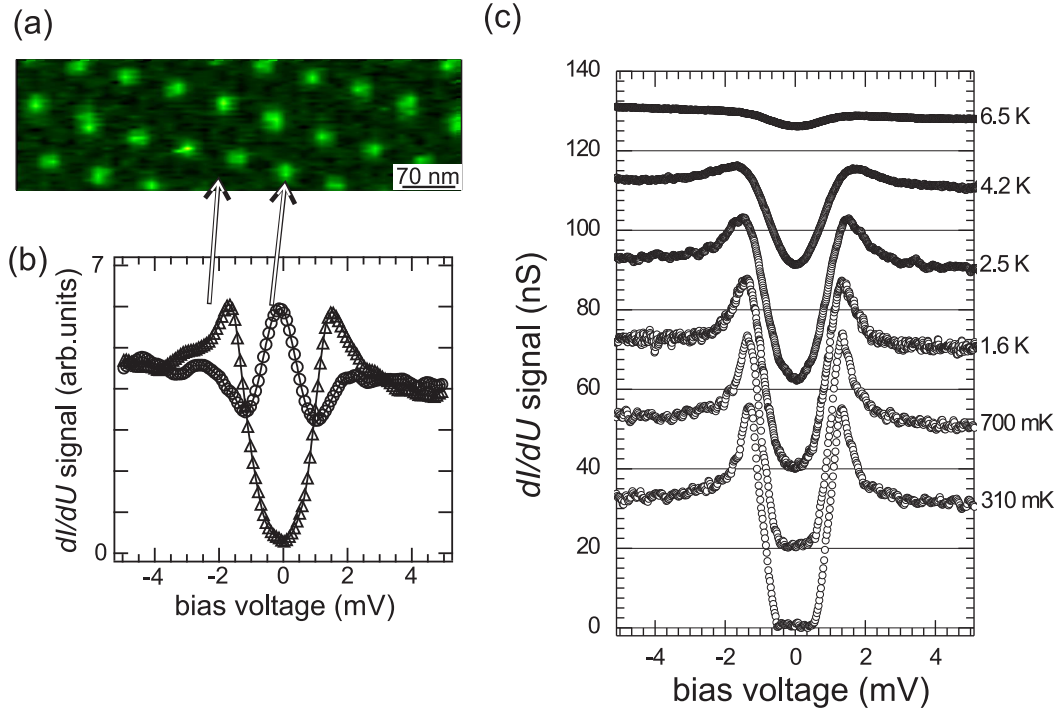


Figure 3.8: (a) dI/dU slice of the cleaved NbSe₂ surface showing the Abrikosov flux lattice at a magnetic field of 0.5 T and at a sample bias of 0 mV ($I_{\text{stab}} = 0.2$ nA, $U_{\text{stab}} = -6.8$ mV, $U_{\text{mod}} = 80$ μV_{rms} , $T = 310$ mK). (b) dI/dU spectra measured on a superconducting area (triangles) and on a vortex (circles). (c) dI/dU spectra measured on NbSe₂ at 0 T. The measurement temperature is given besides each curve. The curves are averages from several single curves taken on the same sample area; 300 mK-1.6 K: average of 2×2 curves; 2.5 K: 3×3 ; 4.2 K-6.5 K: 10×10 . The curves are offset by 20 nS steps for clarity ($I_{\text{stab}} = 0.2$ nA, $U_{\text{stab}} = 6$ mV, $U_{\text{mod}} = 24$ μV_{rms}). For all measurements a W-tip was used.

with a flat and clean surface can be transferred to the STM.

Figure 3.8(a) shows a dI/dU slice of the NbSe₂ surface at zero bias voltage with an applied magnetic field of 0.5 T which is in between the lower and upper critical field of type II superconductors. Due to the magnetic flux, which penetrates the superconductor, a regular hexagonal lattice of vortices, the so-called Abrikosov flux lattice, is formed. The vortices appear brighter in the dI/dU slice at 0 mV, because the superconducting phase is destroyed inside the region, where a flux

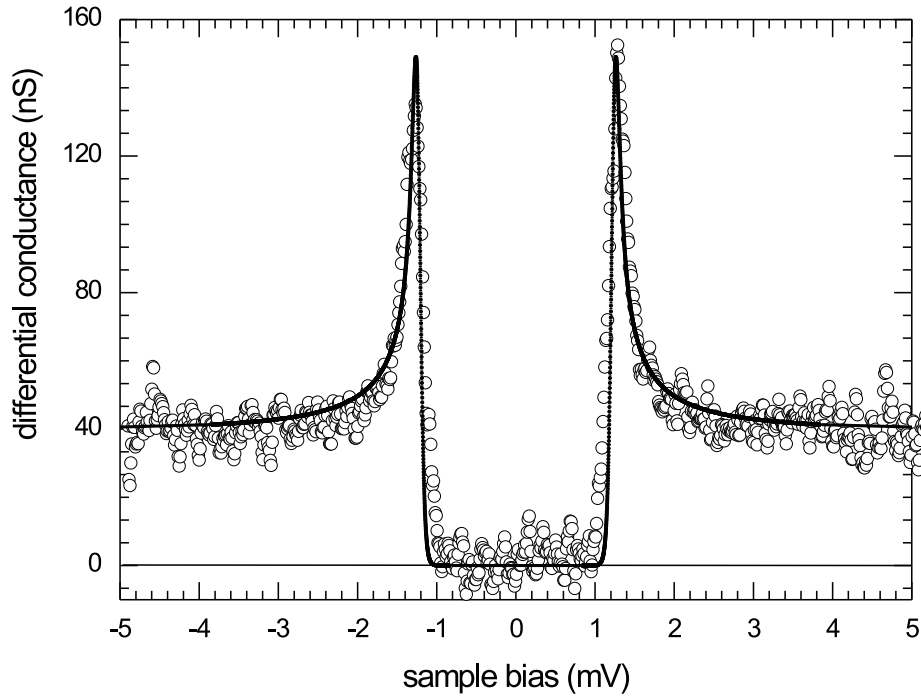


Figure 3.9: Open circles: dI/dU curve measured by lock-in technique with a Nb tip on a W(110) sample ($I_{\text{stab}} = 0.2$ nA, $U_{\text{stab}} = -5$ mV, $U_{\text{mod}} = 20$ μV_{rms} , $T = 315$ mK). Solid line: fit to the experimental data revealing a superconducting energy gap of $\Delta = 1.23$ meV and a fit temperature of $T_{\text{fit}} = 315$ mK.

quantum penetrates the material.⁶ This is illustrated in Fig. 3.8(b), which shows dI/dU spectra averaged above and outside of a vortex. While the spectrum on the vortex appears metal-like apart from a zero-bias anomaly [34], the spectrum taken on the superconducting area exhibits the characteristic superconducting gap with the vanishing conductance around 0 mV. Although the spectroscopic differences appear in a very small voltage range of below 8 mV, the differences in the dI/dU spectra are very well resolved, which indicates a high energy resolution even while applying a magnetic field.

In order to describe the differential tunneling conductance between a normal conductor (nc) and a superconductor (sc), the standard relation for $I(U)$ spec-

⁶For more details we refer to textbooks on superconductivity like [35].

tra [17, 36, 37]

$$I(U, T_{sc}, T_{nc}) \propto \int_{-\infty}^{\infty} \rho_{nc}(\epsilon + eU) \cdot \rho_{sc}(\epsilon) \cdot [f(\epsilon + eU, T_{nc}) - f(\epsilon, T_{sc})] d\epsilon \quad (3.1)$$

with the density of states ρ_{sc} and ρ_{nc} and the corresponding Fermi functions f is used. In contrast to Eqn. 2.17 non-zero temperatures, which can be different for the superconductor T_{sc} and the normal conductor T_{nc} , are now allowed. According to the BCS theory⁷ the density of states of the superconductor is given by [38]:

$$\rho_{sc}(\epsilon) \propto \begin{cases} \frac{|\epsilon|}{\sqrt{\epsilon^2 - \Delta^2(T_{sc})}} & : |\epsilon| \geq \Delta(T_{sc}) \\ 0 & : |\epsilon| < \Delta(T_{sc}) \end{cases} . \quad (3.2)$$

$\Delta(T_{sc})$ denotes the superconducting energy gap around E_F . Together with the assumption that ρ_{nc} is approximately constant in the small energy range around E_F , this leads to

$$\frac{dI}{dU}(U) \propto \int_{\Delta}^{\infty} \frac{\epsilon}{\sqrt{\epsilon^2 - \Delta^2(T_{sc})}} \times \frac{d}{dU} f_{nc}(\epsilon + eU, T_{nc}) d\epsilon . \quad (3.3)$$

This expression shows that the temperature dependence of $dI/dU(U)$ is mainly dominated by the temperature of the normal conductor via its Fermi function for $T_{sc} \ll T_C$ since $\Delta(T)$ is constant in this range. Fig. 3.8(c) shows dI/dU spectra measured on NbSe₂ with a W-tip at variable temperatures in zero magnetic field. The temperature dependence of the superconducting energy gap can clearly be observed: with increasing temperature the gaps become smaller and flat until only a small dip is visible close to T_C . A small difference between the spectra measured at 310 mK and 700 mK is visible, i.e. an earlier onset of non-zero conductance within the gap. Taking into account that the temperature dependence on the dI/dU signal is now dominated by the normal conducting tip, this indicates that the electronic temperature of the tip is well below 700 mK.

Since the superconducting gap of NbSe₂ is anisotropic [39], a fit to conventional BCS theory is difficult. Therefore, dI/dU spectra of a W(110) sample using a superconducting niobium tip were measured in order to determine the temperature of the sample. A similar experiment using the Au(111) surface is known to yield dI/dU spectra that fit well to BCS theory [40]. For this, mechanically sharpened, polycrystalline Nb wires with a diameter of 0.8 mm were used. The W(110) surface is prepared as described in Sec. 3.2.5. After mounting the tip into the STM, voltage pulses on the W(110) surface were applied to remove the oxide and contaminations from the tip. The dI/dU spectra are then measured

⁷Bardeen, Cooper, and Schrieffer.

on a clean W(110) area with a clean Nb tip. Figure 3.9 shows a dI/dU spectrum measured at base temperature. In order to determine the electronic temperature of the normal conducting sample the differential conductance measured via lock-in amplifier can be expressed alternatively to Eqn. 3.3 by

$$\frac{dI}{dU}(U) \propto \int_{-\pi/2}^{\pi/2} \sin\alpha \cdot I\left(U + \sqrt{2} \cdot U_{\text{mod}} \cdot \sin\alpha, T_{nc}, T_{sc}\right) d\alpha \quad (3.4)$$

with $I(U, T_{nc}, T_{sc})$ from Eqn. 3.1, which has to be numerically integrated, using $U_{\text{mod}} = 20 \mu\text{V}_{\text{rms}}$. A curve, which is given by Eqn. 3.4, is fitted to the raw data by adjusting the energy gap $\Delta(T_{sc})$ and the temperature $T_{\text{fit}} \equiv T_{nc}$ of the Fermi function. The measured energy gap $\Delta(T_{sc})$ depends on the micro-tip, i.e. it can change after field emission, as already described by Pan *et al.* [40]. For the performed measurements this effect results in a variation of the gap by approximately $\pm 10\%$. The fit result is shown in Fig. 3.9 as a solid line revealing a fit temperature of $T_{\text{fit}} = 315 \text{ mK}$ and an energy gap of $\Delta(0) = 1.23 \text{ meV}$. The same procedure was carried out for several different measurements using different Nb micro-tips and different stabilization currents resulting in an average sample temperature of $T_{\text{fit}} = 350 \pm 35 \text{ mK}$. This is only slightly higher than the sample temperature read off from the temperature sensor on the STM head. According to Eqn. 2.22 and with $U_{\text{mod}} = 20 \mu\text{V}_{\text{rms}}$ such a temperature results in an energy resolution of $101 \mu\text{eV}$, which is only slightly higher than the thermal limit of $3k_B T = 85 \mu\text{eV}$.

3.2.5 Spin resolution

The intensively studied stripe-domain structure of Fe double-layer (DL) nanowires on W(110) is a perfect sample system to probe the magnetic sensitivity of the tips coated with thin magnetic films [41]. While the easy axis of the ML was found to be in-plane orientated, the DL nanowires are known to exhibit a domain configuration with alternating out-of-plane stripe domains and a Néel-type domain wall in between.

The nanowires are prepared by deposition of 1.4–1.6 AL Fe at a temperature of approx. 500 K on a clean W(110) substrate, which is obtained by repeated cycles of heating at 1500 K in an oxygen atmosphere of 5×10^{-7} mbar and subsequent flashing to $T = 2300 \text{ K}$ [42]. Figure 3.10(a) shows a topographic image of 1.5 AL Fe/W(110) at base temperature. It shows that alternating Fe monolayer (ML) and Fe DL stripes run parallel to the step edges of the W(110) substrate. The lattice mismatch of 9.4% between Fe and W leads to the formation of dislocation lines in the DL. Figure 3.10(b) shows the section along the line indicated in (a) and sketches the local Fe coverage on the substrate. Figure 3.10(c) reveals a simultaneously recorded dI/dU map using a Cr-coated tip (90 AL). Due to the out-of-plane orientation of the Cr tip, the ML appears uniformly dark, whereas

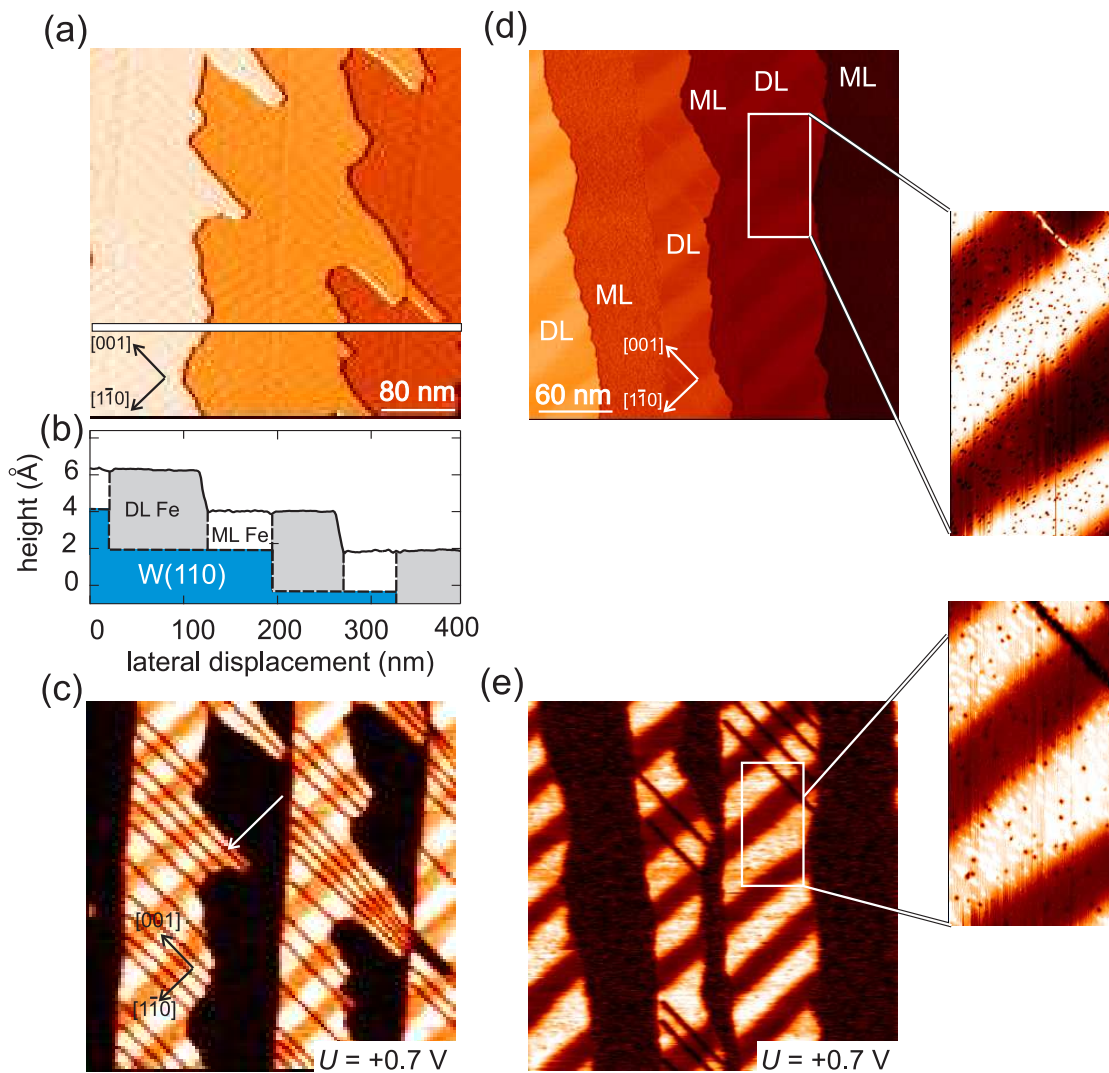


Figure 3.10: (a) Topographic image of 1.5 ML Fe/W(110) (partly differentiated) measured with an out-of-plane sensitive Cr tip. (b) Section along the line drawn in (a). (c) dI/dU map measured simultaneously to (a). DL stripes show an out-of-plane domain contrast with domain walls oriented roughly along $[1\bar{1}0]$ perpendicular to the dislocation lines (see white arrow) ($I = 0.7$ nA, $U_{\text{mod}} = 30$ mV). (d) Topographic image of 1.5 ML Fe/W(110) (partly differentiated) measured with an out-of-plane sensitive Fe tip. On DL stripes the domain contrast is visible ($I = 1.0$ nA, $U = +0.05$ V, $U_{\text{mod}} = 20$ mV). (e) dI/dU map measured simultaneously to (d). Insets in (d) and (e): Highly resolved magnified views. All images have been recorded at 0.315 K.

the DL exhibits a regular pattern of oppositely magnetized out-of-plane domains with a period of 44 ± 1 nm, which is in agreement with studies performed in a wide temperature range on this sample system [43]. The dislocation lines are visible as dark lines which run along the [001] direction as indicated.

In addition to the tip preparation method (reported in Sec. 2.6), the coating of the tip can also be achieved using a different procedure. Magnetic material can be transferred to the tip by voltage pulses on magnetic samples [44] or by dipping the tip into the magnetic sample surface. The latter has been performed with a bare W tip which gently touched the surface of 1.5 AL Fe/W(110) at around 40 K. While afterwards no magnetic contrast was observed at 40 K a strong magnetic contrast was found at 0.315 K as shown in Figs. 3.10(d) and (e). Already in the topography, the spin sensibility results in a height difference of about 40 pm on the oppositely magnetized domains at this particular bias voltage of +0.05 V. This is emphasized in the inset image, which reveals a magnified view of the marked region in (d). The magnetic contrast observed in the simultaneously recorded dI/dU map in Fig. 3.10(e) is relatively high with about 30%. Again the domains exhibit a period of 44 ± 1 nm. Fitting the domain wall profile as described in Ref. [26] reveals a tip magnetization of $10^\circ \pm 10^\circ$ relative to the surface normal. Since the magnetic contrast is absent at 40 K one can conclude that the magnetic material which is attached to the tip is in a superparamagnetic state with a blocking temperature below 40 K. This could be an Fe cluster of an appropriate size, which is attached to the apex of the nonmagnetic W tip. The observed unusual magnetic orientation of the Fe tip already reveals a disadvantage of such a preparation method, since the magnetic direction cannot be adjusted by the preparation procedure. Anyhow, these results suggest that the preparation of spin-sensitive tips could be quite easy at very low temperatures.

4 The Pt(111) surface and its surface state

This chapter presents the results concerning the electronic structure of the bare Pt(111) surface. It was possible to observe and explain the dispersion of an unoccupied surface state on Pt(111) by imaging scattering states with the help of scanning tunneling spectroscopy. By comparison to first-principles electronic structure calculations the state is assigned to an *sp*-derived surface band at the lower boundary of the projected bulk band-gap. The onset of the surface band appears as a rather broad feature in $dI/dU(U)$ spectra, whose shape is explained by two spin-orbit split branches with nearly linear dispersion where the lower mixes into bulk states at higher energies.

This chapter is organized as follows: After an introduction in Sec. 4.1, where basic properties of surface states on the (111)-surfaces of noble and late transition metals are discussed, Sec. 4.2 reports on the preparation of the Pt(111) surface. In Sec. 4.3 the experimental results are presented. The first-principles electronic-structure calculations are shown in Sec. 4.4 and compared to the experimental data in Sec. 4.5. Finally, in Sec. 4.6 the results are summarized.

4.1 Introduction

Partly occupied surface states are known to play a crucial role in chemistry, growth properties and magnetism of the surfaces of noble metals (Cu, Ag, Au) and late-transition fcc metals (Ni, Pd, Pt).¹ They have therefore been studied quite extensively by photoelectron spectroscopy [45]. As was shown more than ten years ago, surface states and their interaction with defects and step edges can be studied on a local scale by scanning tunneling spectroscopy (STS) [46,47]. Recent publications in this field deal with the interaction with atomic adsorbates [48,49] or with the interaction between atomic adsorbates mediated by surface states, [50] with lifetime effects, [51] the Stark effect [52] or even spin-orbit induced spin-splitting similar to the Rashba effect in two-dimensional electron systems of semiconductor heterostructures [53–55].

¹fcc denotes the crystal lattice structure *Face-Centered Cubic*.

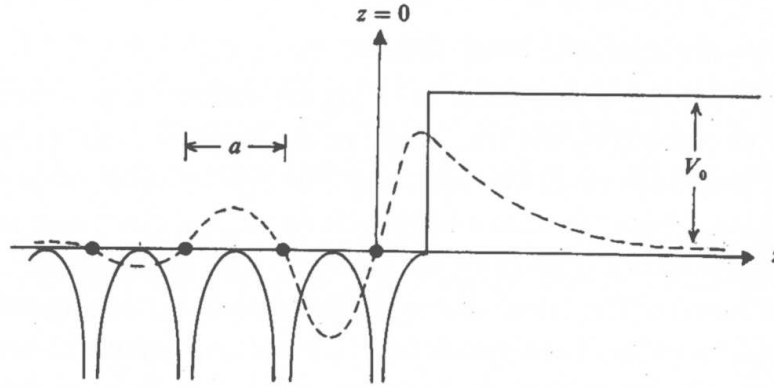


Figure 4.1: One dimensional semi-infinite lattice model potential (solid line). The surface state shows the highest localization at the surface and decays exponentially into the vacuum as well as into the crystal (dashed line). The figure is taken from Ref. [56].

Basic properties of surface states

The existence of a surface has a great impact on the structure and position of surface atoms as well as on the electronic properties of the crystal. In the bulk the Schrödinger equation is solved by three dimensional Bloch functions, which results in the formation of the bulk electron band structure. Due to the surface the translation symmetry, which is fundamental for the concept of Bloch functions, is broken at least in the direction of the surface normal. Even in the case of an ideal surface, where the atoms are still at bulk-like positions, new electronic effects can be observed [57]. One of these effects is the so-called surface state.

The development of a surface state and its fundamental properties can be described basically by assuming a simple one dimensional model where the electron is treated as nearly free. Figure 4.1 shows the potential of a one dimensional semi-infinite crystal or chain with a surface. In addition a wave function is indicated which shows a typical property of a surface state, i.e. an oscillation according to the wave vector k and an exponential growth in z -direction. Without the surface this wave function would be forbidden because of the unlimited exponential growth in one direction. The absence of such wave functions leads to the formation of a band gap in the bandstructure of the infinite chain. By introducing a surface a new boundary condition arises: Outside the crystal the wave function is exponentially damped if the energy of the electrons is smaller than the work function V_0 . This allows for the formation of new states with corresponding energy eigenvalues in the band gap, if these states fulfil the matching conditions at the surface. Then the corresponding wave functions are located only at the

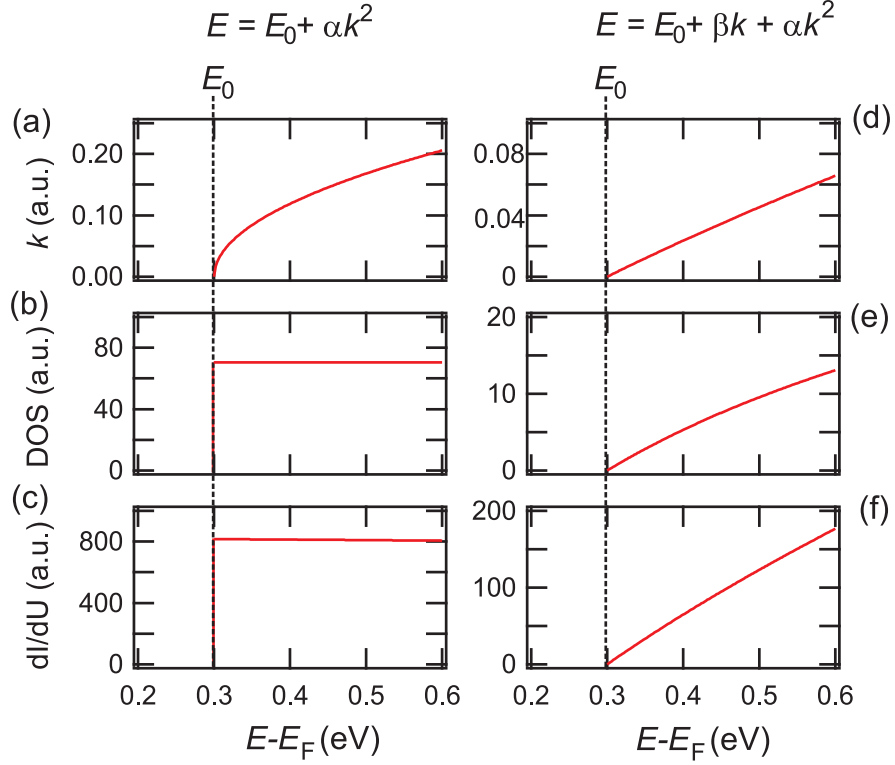


Figure 4.2: Left panels (a)-(c): Sketch of dispersion, DOS, and calculated dI/dU signal for purely quadratic dispersion as indicated. Right panels (d)-(f): As for the left panels but based on a quadratic dispersion with a strong linear contribution. ($E_0 = 0.3 \text{ eV}$, $\alpha = 5.59 \text{ eV\AA}^2$, $\beta = 4.56 \text{ eV\AA}$)

surface because they decay exponentially into the bulk as well as into the vacuum as indicated in Fig. 4.1. These states are called surface states.

In order to describe the impact of a surface to a three dimensional crystal, one can generalize the results obtained for a semi-infinite one-dimensional chain. Parallel to the surface where the translation symmetry is still valid the wave functions can be described by two dimensional Bloch functions with a vector \vec{k}_{\parallel} . For each \vec{k}_{\parallel} a surface state exists, which is localized in parallel to the normal of the surface plane. This leads to a two dimensional surface state band. If this surface state band starts below the Fermi energy, and thus is partly occupied, it contains a two dimensional electron system (2DES) directly at the interface. In the case that the electron system in the surface can be described by a nearly free electron (NEF) model the dispersion of the surface state band is described by

$$E(\vec{k}_{\parallel}) = E_0 + \frac{\hbar^2}{2m^*} k_{\parallel}^2 \quad (4.1)$$

where m^* is the effective electron mass which is a measure for the curvature of the parabola. Typically, m^* is given in units of the electron mass m_e . Figure 4.2(a) schematically shows a branch of the quadratic dispersion. Without taking into account any contributions of the bulk bands, the local density of states (*LDOS*) of the 2DES is given by

$$LDOS = \frac{k_{\parallel} dk_{\parallel}}{2\pi dE} = \frac{m^*}{\pi\hbar^2} = \text{constant}. \quad (4.2)$$

Thus, the energy depending *LDOS* of a 2DES in Fig. 4.2(b) shows a step-like feature exactly at the energy of the surface state band onset E_0 . Assuming a constant *LDOS* of the tip and taking into account the energy and k_{\parallel} dependence of the transmission coefficient (Eqn. 2.19) the numerical dI/dU signal can be calculated according to Eqn. 2.21. The result is shown in Fig. 4.2(c) and exhibits a nearly identical shape as the *LDOS*, but with a decrease for higher energies due to the increasing k_{\parallel} .

Furthermore the presence of a surface causes not only the formation of surface states but can also cause a spin-orbit-induced spin splitting due to the broken inversion symmetry in comparison to the bulk. This effect is in close analogy to the Rashba effect in 2DES of semiconductor heterostructures and can be described by an additional Hamiltonian

$$H_{\text{SO}} = \frac{\vec{s}}{2c^2} (\vec{\nabla}V \times \vec{p}) \quad (4.3)$$

where \vec{s} and \vec{p} are the spin and the momentum operator, respectively. $\vec{\nabla}V$ is the gradient of the potential at the surface. Adding this Hamiltonian to the Schrödinger equation of the 2DES the resulting energy eigenvalues are like in Eqn. 4.1 but complemented by a linear term, the so-called Rashba term. They are given by

$$E(k_{\parallel}) = E_0 + \frac{\hbar^2}{2m^*} k_{\parallel}^2 \pm \gamma_{\text{SO}} k_{\parallel}. \quad (4.4)$$

In a free electron approach the parameter γ_{SO} is only related to the surface potential gradient $\vec{\nabla}V$. Following a tight-binding approach, Petersen and Hedegård pointed out in Ref. [54], that γ_{SO} depends on the atomic spin-orbit parameter, which itself is proportional to the nuclear charge, as well as on the surface potential gradient. Due to a non-zero γ_{SO} there are now two parabolae, which are shifted horizontally by a constant Δk with respect to each other, representing each the dispersion of one spin direction.

As visible in Eqn. 4.1 the spin-orbit induced spin-splitting results not only in a splitting, but also in a linear contribution to the quadratic dispersion. Another reason for a linear contribution can originate from a coupling of the surface state to

noble metal	E_B (eV)	E_0 (eV)	m^*/m_e
Cu(111)	-0.82 eV	-0.39 eV	0.58
Ag(111)	-0.30 eV	-0.12 eV	0.28
Au(111)	-0.90 eV	-0.41 eV	0.34

Table 4.1: Values of sp -like surface state of Cu(111), Ag(111), and Au(111). The differences $E_B - E_0$ reveal that the surface states of the noble metals are located well inside the projected bulk band gap. All values are taken from Ref. [59].

bulk states as will be shown in Sec. 4.4. The impact of a strong linear contribution to the dispersion is shown in Fig. 4.2(d)–(f). As in the left panels of Fig. 4.2, the right panels show the same graphs but now for a dispersion exhibiting a strong linear contribution. A comparison to the corresponding graphs of the left panels reveals that the linear contribution in Fig. 4.2(a) leads to a different appearance of the DOS as well as of the dI/dU signal. The DOS in Fig. 4.2(e) leads consequently to a rising edge in the dI/dU signal in Fig. 4.2(e), which starts at E_0 , instead of a sharp onset as in (c). Especially these differences in the measured dI/dU signal for the two dispersions play a role in the following sections.

(111) surface states of noble metals

For (111) surfaces of the noble metals Cu, Ag, and Au it is well known that a partly occupied crystal-induced surface state resides far inside the projected bulk sp -band gap at the center of the Brillouin-zone. This sp -like surface state is usually referred to as Shockley surface state. Thereby sp denotes the origin of the bulk states which surround the band gap. Figure 4.3(a) shows a part of the measured surface Brillouin zone (SBZ) for Cu(111) [58]. A parabola which starts at $k_{\parallel} = 0$ and $E_B = -0.9$ eV marks the border between the occupied projected bulk bands and the band gap. Inside the energy gap of the SBZ the surface state band is found. It starts at $k_{\parallel} = 0$ and $E_0 \approx -0.4$ eV and is therefore well separated from the bulk states. Table 4.1 shows the corresponding values for Cu(111), Au(111), and Ag(111) as well as the effective electron masses. In Fig. 4.3(b) a measured dI/dU on Cu(111) is shown [51]. The sharp onset of the noble metal surface states at $E_0 \approx -0.4$ eV is clearly visible. Using high angular resolved photoemission experiments it was possible to measure the spin-degenerated dispersion for Au(111) [53, 55]. Figure 4.3(c) shows both spin degenerated (except at $k_{\parallel} = 0$) parabolic dispersions along one high symmetry direction. The splitting of the two branches amounts to $\Delta k = 0.025 \text{ \AA}^{-1}$. For a given wave vector the spin of one curve is antiparallel oriented with respect to the other curve at the same wave vector. Taking into account also other directions, Fig. 4.3(d) resolves the spectral intensity at E_F .

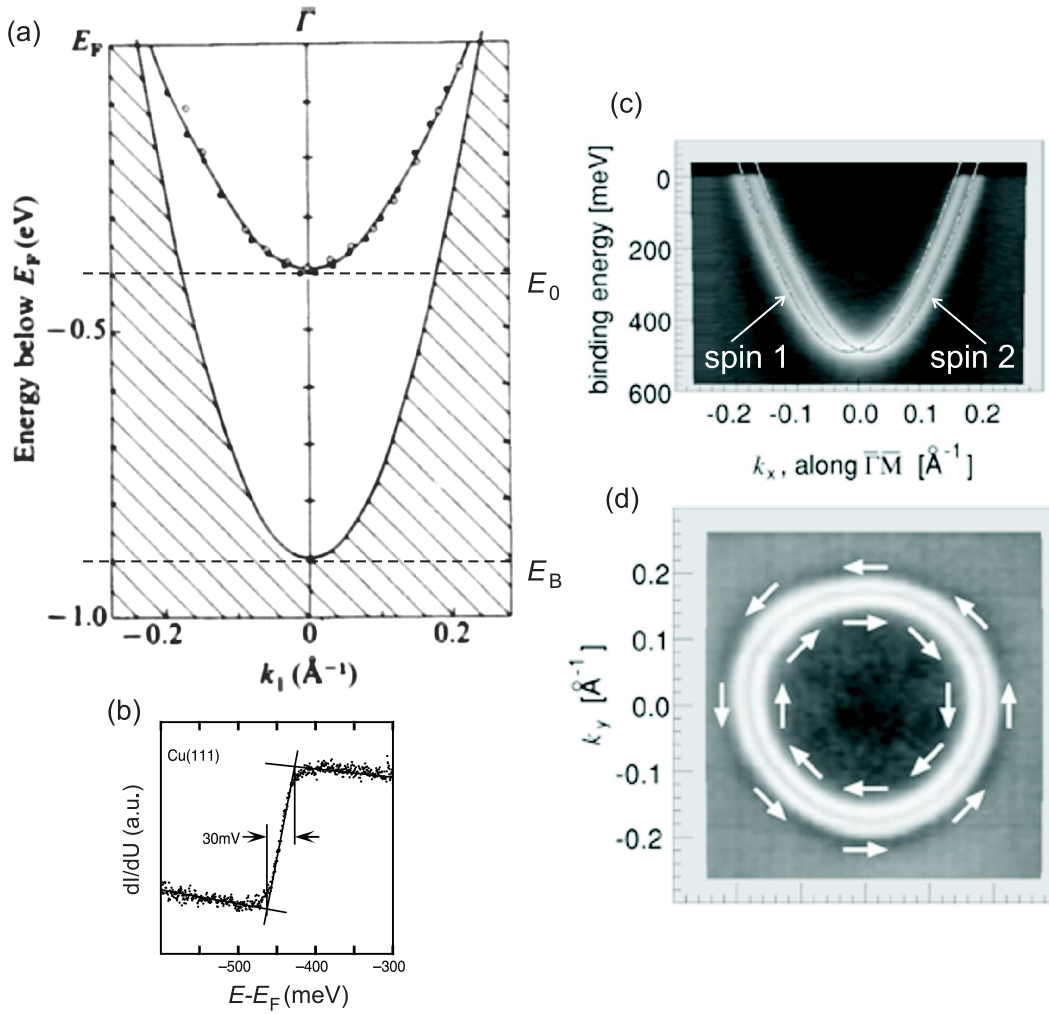


Figure 4.3: (a) Experimental dispersion of Cu(111) surface state from Ref. [58]. Hatched area indicates projection of the bulk bands. The surface state band is located in the projected bulk band gap. (b) dI/dU spectrum measured on Cu(111) (taken from Ref. [51]). The sharp onset of the surface state is visible. (c) Measured dispersion for spin-orbit-induced splitted surface state band of Au(111). (d) Spectral intensity at E_F for different wave vectors. Figures (b) and (c) are taken from Ref. [55].

The two rings originate from the shifted parabolae. The figure reflects, that the electron spin is oriented perpendicular to k_{\parallel} and lies in the surface plane. So far the spin-orbit-induced spin degeneration is only observed for Au(111) and not for Cu(111) and Ag(111) due to a smaller spin-orbit coupling. According to the work of Petersen and Hedegård [54] the splitting of the sp -like surface state is not observable in the surface LDOS as probed with STM.

(111) surface states of late transition metals

While the description of surface states of the (111) surfaces of noble metals is quite uniform, the situation is more complex for the late-transition fcc metals Ni, Pt, and Pd.

Ni(111) has a spin-split surface state just at the bottom of the band gap which is caused by exchange splitting. In contrast to the spin-orbit-effect the exchange splitting leads to a vertical shift of the dispersion in energy as shown by the NEF model [60]. In the case of Ni(111) this results in an unoccupied minority spin state whereas the majority spin state is partly occupied [61–63]. In contrast, the corresponding surface state on Pd(111) is unoccupied and far above the Fermi energy E_F [64,65]. The effective mass in both cases is $0.2m_e$ to $0.3m_e$ and thus comparable to the noble-metal case.

For Pt(111) the situation is controversial. In an early photoemission study of Roos *et al.* [66,67] a feature below E_F was attributed to a surface state in the projected bulk band structure which was thus claimed to be occupied but it would have a surprisingly large effective mass of $1.3m_e$. In contrast inverse photoemission data shows indications for an unoccupied surface state that is located approximately 0.5 eV above E_F [68]. Later, this was confirmed theoretically and substantiated by comparison to lifetime measurements of image potential states [69,70]. Up to now, there is no direct photoemission measurement of the dispersion of an unoccupied surface state, nor is it visible in previous STS studies [71]. This means that there are no experimental data so far to clarify the situation. This is even more surprising since the Pt(111) surface is one of the most studied surfaces due to its importance as catalyst for surface chemistry. Many experiments have been performed in order to obtain insights into the fundamental properties of sub-monolayer homoepitaxial growth, surface diffusion, molecular physics and adsorption as well as catalytic processes [72–76].

The following section will show that an unoccupied surface state on Pt(111) can be directly observed by STS in form of scattering states at step edges or point defects. By comparison of the measured dispersion relation to first-principles electronic-structure calculations it is assigned to an *sp*-derived surface state which is located just at the lower edge of the projected bulk band-gap.

4.2 Preparation of the Pt(111) surface

Following the preparation procedures reported in the literature, the present single crystal Pt(111) was prepared by repeated cycles of room temperature sputtering (5–10 AL) with 600 eV Ar-ions, flashing to 1000 K, annealing in an oxygen atmosphere of $2 \cdot 10^{-6}$ mbar at 1000 K for half an hour and a final flash at 1200 K. This preparation procedure results in a clean Pt(111) surface exhibiting tens of a nm wide terraces as shown in Fig. 4.4(a). Figure 4.4(b) shows a section along

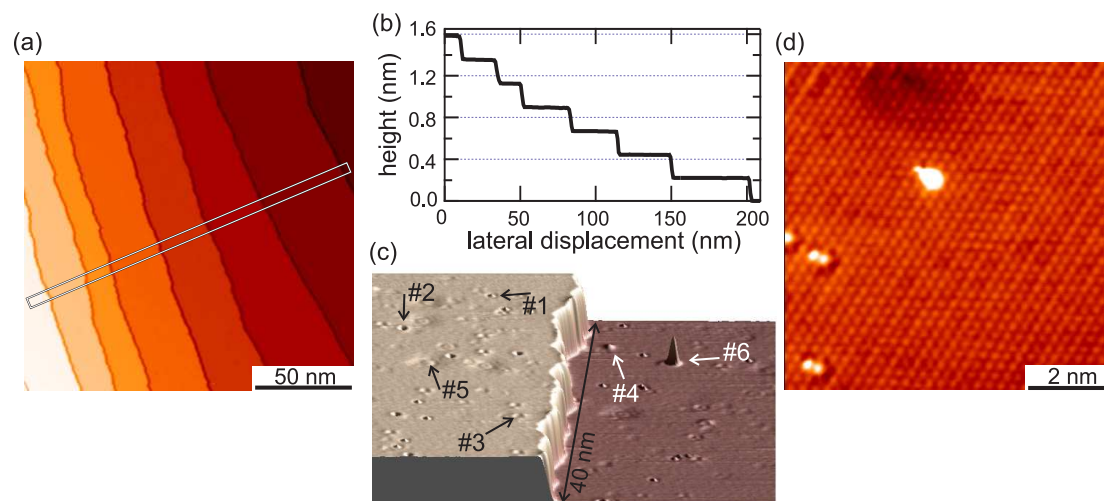


Figure 4.4: (a) Topographic image of the bare Pt(111) surface ($U = 1.0$ V, $I = 0.2$ nA). (b) Section along the box indicated in (a). (c) Topographic image of two terraces on Pt(111). Six different kinds of remaining adsorbates and defects are observable ($U = 0.6$ V, $I = 0.4$ nA). (a) and (c) are partially differentiated and obtained at 0.315 K. (d) Topographic image of the atomically resolved Pt(111) surface at 4.2 K ($U = -25$ mV, $I = 6.22$ nA).

the box indicated in Fig. 4.4(a). The terraces are separated by monoatomic steps with a height of 2.27 \AA . Even though no indications of remaining adsorbates were observed in Auger spectra, a closer inspection of the terraces reveal adsorbates as shown in Fig. 4.4(c). Six different kinds of point defects having heights of up to 20 pm (except #6) are visible and distinguishable on both terraces. While type #1 appears as a small protrusion which is surrounded by a ring of depression, #2 appears as a ringlike protrusion. #3 also appears as a ring-like protrusion but shows a threefold symmetry. #4 shows a small protrusion. #5 appears as depression with a comparatively large width of about $20\text{--}30 \text{ \AA}$. Finally, #6 exhibits a height of about 1 \AA and originates from the tip. Although the exact chemical composition of the adsorbates is unknown they are probably due to a remaining contamination of carbon and oxygen. Typically the coverage of remaining adsorbates and point defects is about 0.15% with respect to the total number of fcc and hcp adsorption sites. Figure 4.4(d) shows an image of the surface with atomic resolution. The hexagonal atomic lattice of the Pt(111) surface with an in-plane lattice constant of 2.77 \AA is clearly visible.

4.3 Experimental results

All experiments presented in this section were performed in the low temperature ultra-high vacuum STM-system operating at a temperature of $T = 0.3$ K as described in Chap. 3. Figure 4.5(a) shows a topographic image of the Pt(111) surface. The two terraces are separated by a monoatomic step apparent at the front. Figures 4.5(b)–(f) show dI/dU -maps with decreasing bias voltages as indicated. Most apparent in Fig. 4.5(b), a spatially oscillating dI/dU signal is visible near the step edge and in the surroundings of point defects. The wavelength λ of this oscillation is the same for all kinds of defects even though the intensity is changing for different defects. It is clearly visible that a decreased bias voltage U leads to a larger λ in Figs. 4.5(c) and (d). While the oscillating dI/dU signal is still faintly apparent in Fig. 4.5(e) it vanished in Fig. 4.5(f). Thus, the oscillation in dI/dU starts between 0.2 eV and 0.5 eV.

A close inspection of Fig. 4.5(f) reveals another, very weak oscillation with a much smaller wavelength. It is already apparent at higher voltages and marked in Figs. 4.5(c) and (d) by arrows. Since these oscillations are centered at locations without any topographic signature at the surface, they are most probably due to scattering of bulk states.

In order to obtain further information the dI/dU signal is plotted as a function of the distance from a step and from a point defect in Fig. 4.6 (a) and (b), respectively. In the case of the step edge the averaging is performed for a width of 5 nm perpendicular to the propagation direction of the scattering. For the point defect the dI/dU signal is averaged on segments of circles with increasing radius as a function of the distance from the center of the defect. By this averaging procedure overlapping of oscillations originating from other different point defects is avoided. Without loss of generality, the analysis is restricted to the point defects showing the strongest scattering, which appear as depressions with a width of 20 – 30 Å in Fig. 4.4(c) (see defect #5) and 4.5(a) (see arrows). According to Chap. 2 and Ref. [77] care has to be taken to interpret the oscillations in dI/dU directly as oscillations in the LDOS if the tip-sample separation is not constant. A line section of the topography at the top of Fig. 4.6 (a) reveals that the variation in the tip-height on the top terrace is less than 3 pm and not related to the oscillation in dI/dU . These height differences are close to the resolution of our experiment. Simulations analogous to Ref. [77] have shown that the error in λ is less than $\pm 5\%$ if the extracted dI/dU signal is used without normalization. In order to rule out effects of a changing tip height in case of the point defects, only the dI/dU signal farther than 15 Å from the center of the defect is considered.

In order to extract the wavelength λ and consequently the wave vector \vec{k} of the LDOS oscillations Bessel functions have been fitted to the dI/dU signal. As outlined in Ref. [46] different fit functions for scattering at step edges and point defects have to be used. For the step edge the LDOS at a certain energy E is

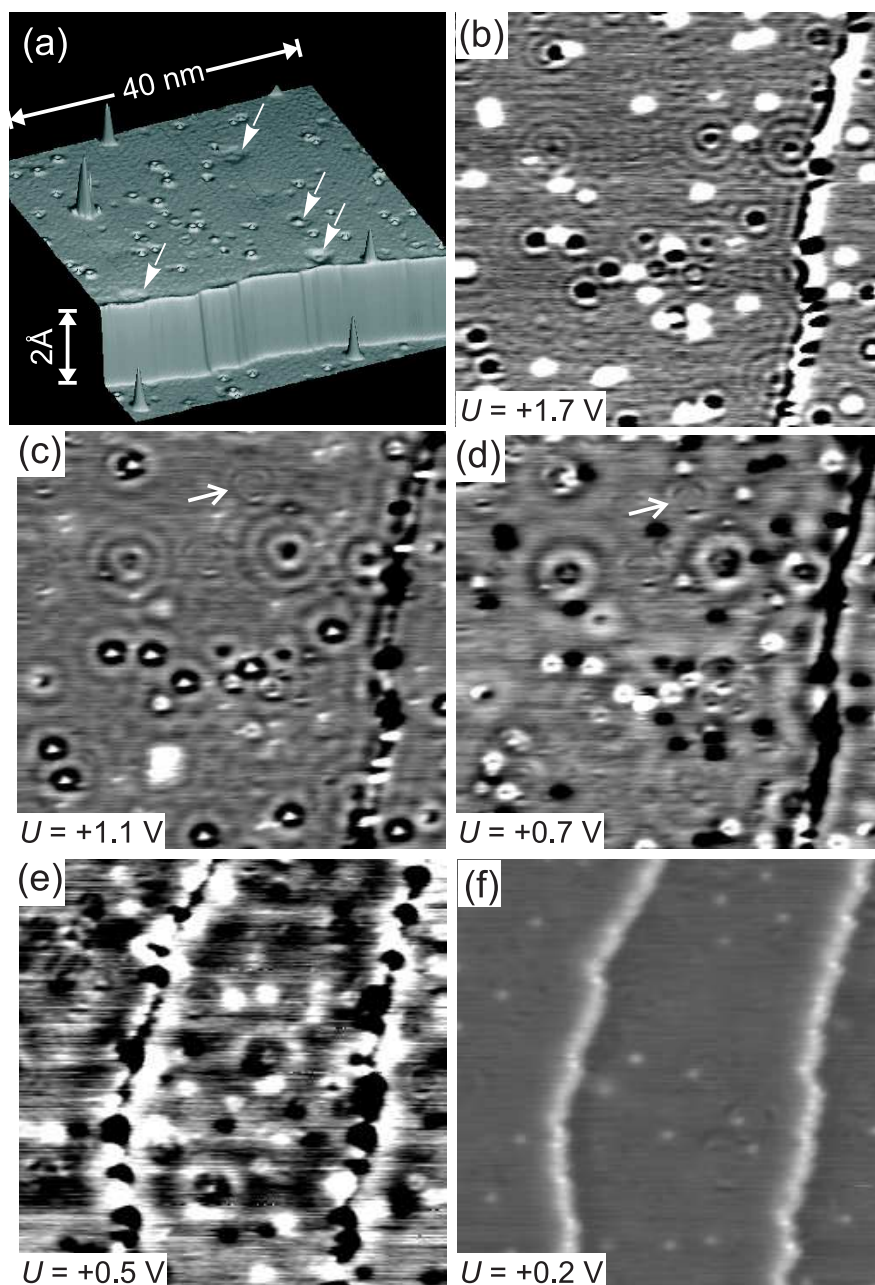


Figure 4.5: (a) Topographic image of the Pt(111) surface showing a step and different point defects on the terrace ($I = 1.0$ nA, $U = 1.1$ V). (b)–(d) dI/dU -maps of the same sample area as in (a) recorded at different sample voltages as indicated ($I = 1.5$ nA, $U_{\text{mod}} = 50$ mV). (e),(f) dI/dU -maps at indicated voltages taken at another sample area ($I = 2$ nA, $U_{\text{mod}} = 50$ mV). The contrast in (e) and (f) covers the same dI/dU range. The arrows in (c) and (d) mark scattering due to bulk states.

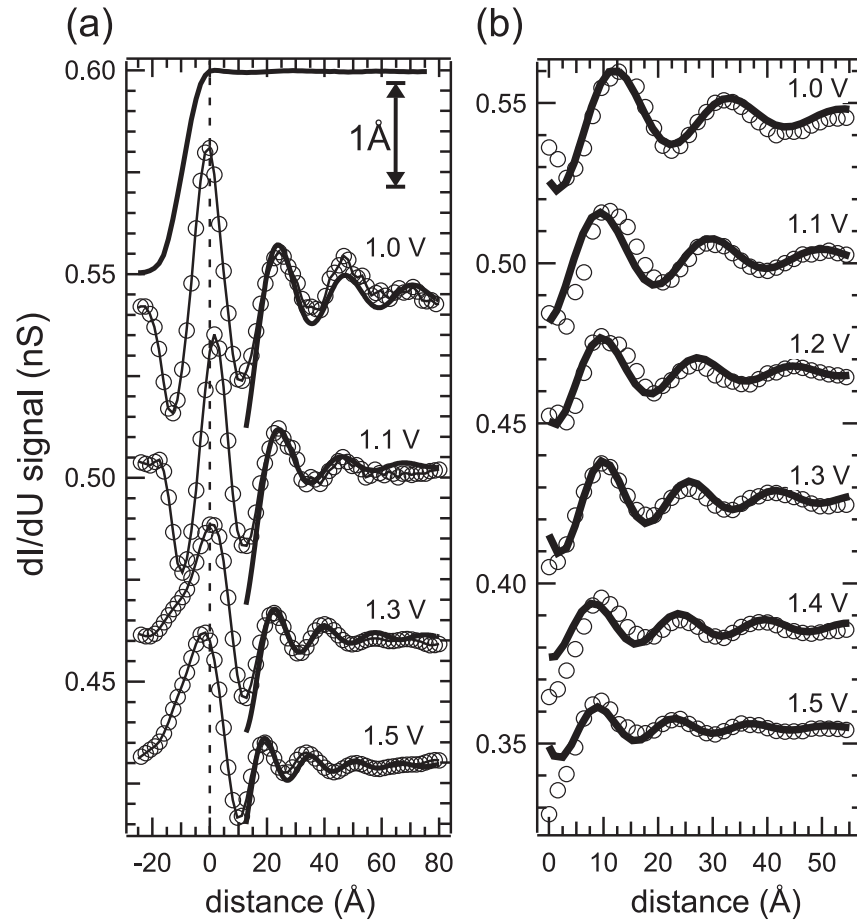


Figure 4.6: (a) Circles with thin lines: spatial dependence of the dI/dU signal measured as a function of the distance from a step edge at different sample voltages as indicated ($I = 1.5$ nA, $U_{\text{mod}} = 50$ mV). Curves at 1.3 V and at 1.5 V have been shifted by 0.035 nS and 0.075 nS, respectively. Thick lines: fit to the experimental data (see text). A line section of the step is shown at the top ($I = 2$ nA, $U = 1$ V). (b) Same as (a) but for a point defect. The dI/dU signal is averaged on segments of circles with increasing radius as a function of the distance from the center of the defect.

described by

$$\text{LDOS}(E, x) = (1 - e^{-\frac{x}{d}} J_0(2kx, \delta_0)) * A + B, \quad (4.5)$$

where x is the distance from the step edge. $J_0(2kx, \delta_0)$ is the zero-order Bessel function. The parameters used to fit the experimentally obtained curves are the background LDOS B , the amplitude of the oscillations A and a damping factor d . The cylindrically LDOS around a point defect is given by

$$\text{LDOS}(E, \rho) = \left(\cos^2(k\rho - \frac{\pi}{4} + \delta_0) - \cos^2(k\rho - \frac{\pi}{4}) \right) * e^{-\frac{\rho}{d}} * A + B. \quad (4.6)$$

where ρ is the distance from the point defect. The resulting fit curves are shown in Fig. 4.6(a) and (b) as thick lines. The agreement between the fitted LDOS curves and the measured dI/dU oscillations for step edges as well as for point defects is quite good. Only very close to the defects larger discrepancies occur, which is expected because of the very simple LDOS-model which was used and due to the presence of topographic effects.

Additional information regarding the electronic structure of the surface is obtained by measuring full dI/dU -spectra. Three typical spectra taken on the bare Pt(111) surface are shown in Fig. 4.7(a). For each of them a different STM tip was used. All spectra show a broad peak close to E_F and a step-like feature that starts with a rising edge at $+0.3 \pm 0.1$ eV, followed by a kink at $+0.4 \pm 0.1$ eV where the slope becomes nearly flat. These features have been observed using many different tips and are thus attributed to the sample electronic structure. A comparison of the dI/dU maps in Fig. 4.5 to Fig. 4.7(a) reveals that the position of the rising edge corresponds reasonably well to the onset of the oscillations. As shown in Fig. 4.3(b) for the case of noble metals, a step-like feature occurring together with oscillations around point defects and at step edges was explained in terms of a two dimensional surface state [46, 51, 77]. As explained in Sec. 4.1 the step is located energetically just at the bottom of the surface state band. One can thus tentatively conclude that the oscillations observed on Pt(111) are due to a surface state with the band onset at ≈ 0.3 eV. In other words, Pt(111) has a surface state above E_F .

To examine the surface state in detail, the k values ($k = \pi/\lambda$) versus energy extracted from scattering are plotted in Fig. 4.8. The error in k is due to the evaluation of several defects. The onset of the surface state resulting from the position of the rising edge in dI/dU spectra is included at $k = 0$. In order to determine the character of the surface state, different curves are fitted to the experimental dispersion. A parabolic fit which is expected to work for a typical two-dimensional free-electron like state is shown by a dashed line in Fig. 4.8. Obviously, the curvature of the experimental data is not reproduced. A linear contribution has to be added to the quadratic term. A polynomial fit $E(k) = E_0 + \alpha k + \beta k^2$ with the prefactors $\alpha = (4.1 \pm 0.9)$ eVÅ and $\beta = (7.1 \pm 3)$ eVÅ² results in the best fit and is shown by a solid line.

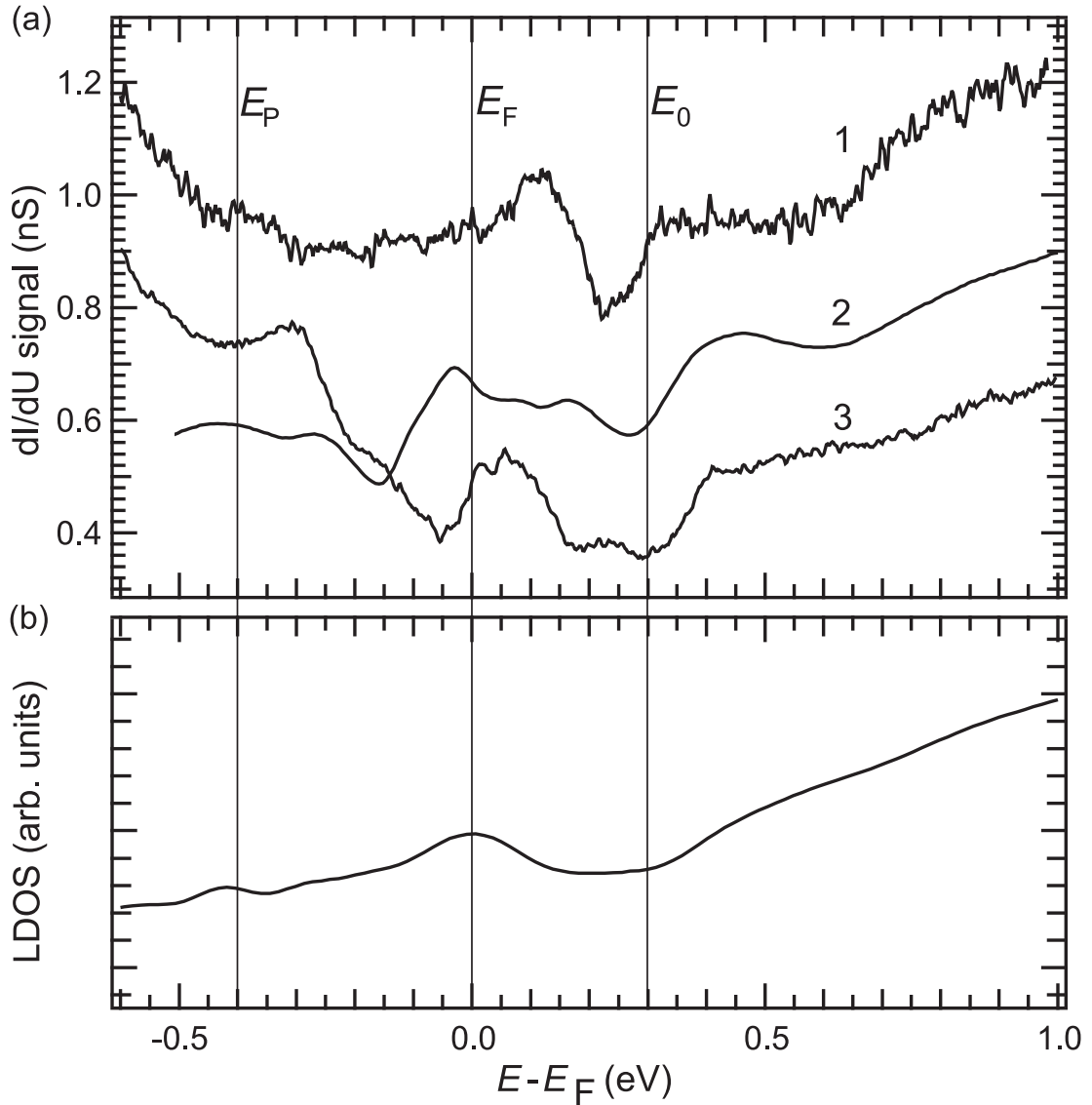


Figure 4.7: (a) Typical dI/dU spectra measured on the bare Pt(111) surface. Different tips were used for each spectrum. Top and middle spectra are shifted by 0.4 nS and 0.2 nS, respectively ($I_{\text{stab}} = 0.5$ nA, $U_{\text{stab}} = 1.0$ V, 1: $V_{\text{mod}} = 1.5$ mV, 2: $V_{\text{mod}} = 20$ mV, 3: $V_{\text{mod}} = 2$ mV). (b) Calculated vacuum LDOS at a distance of about 4 Å from the surface. Vertical lines at E_0 , E_F and E_P mark the onset of the surface state band, the Fermi energy, and the onset of a bulk band with 10% localization in the surface layer, respectively.

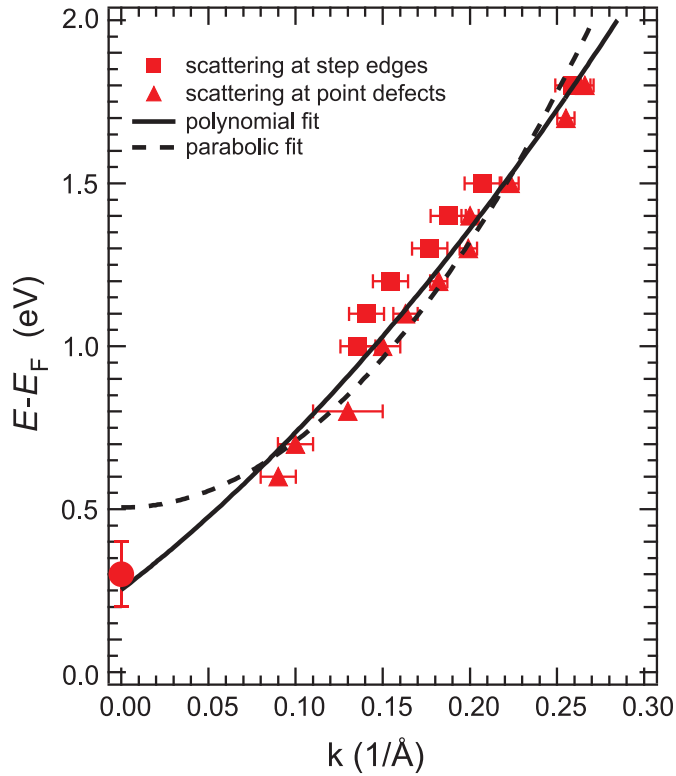


Figure 4.8: k values extracted from the scattering states at point defects (triangles) and step edges (squares). The value at $\bar{\Gamma}$ is extracted from dI/dU spectra (circle). The dashed and full lines represent a best purely parabolic and second-order polynomial fit, respectively.

4.4 Theoretical results

In order to find the origin of the observed scattering states the surface electronic structure has been calculated using density functional theory in the generalized gradient approximation.² Spin-orbit coupling was implemented in the full-potential linearized augmented plane wave method as outlined in Ref. [70]. Compared to these previous results a thicker film with 23 layers was used. The interplanar-distance relaxation at the surface is on the order of 1% [78].

The calculated projected bulk bands and surface states are shown in Fig. 4.9(a). The blue filled dots mark states with an LDOS fraction of 10% at the surface atoms and 5% in the vacuum, which are characteristic values for the surface states. Indicated by the color code a nearly symmetric surface state centered at $\bar{\Gamma}$ is located very close to the bottom of the projected bulk sp -band gap at about +0.35 eV. In order to obtain further information concerning the symmetry of the surface state a contour plot of this state at $\bar{\Gamma}$ is shown in Fig. 4.9(b), revealing that it is very similar to the Au(111) sp -type surface state. As visible at $\bar{\Gamma}$ the surface state is located mainly at the topmost three layers of the surface.

Below E_F an upwards dispersing, occupied bulk band with a 10% localization

²The calculations were performed by G. Bihlmayer and S. Blügel from the *Forschungszentrum Jülich* and by P. Ferriani and S. Heinze from the *Spin Theory Group* in Hamburg.

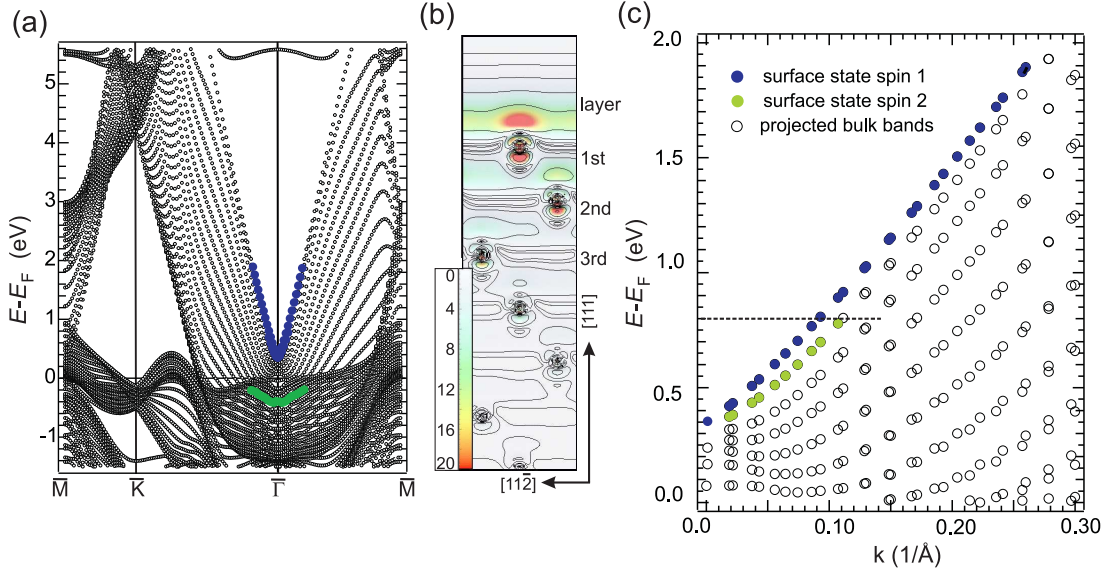


Figure 4.9: (a) Overview of the projected bulk band structure. Surface states are marked by blue dots. A bulk state at $\bar{\Gamma}$ with strong localization in the surface is marked by green dots. (b) Contour plot of the charge density of the surface state at $\bar{\Gamma}$. Contours start from $6.75 \cdot 10^3$ electrons/nm³ and increase by a factor of $\sqrt{10}$. (c) Magnified view of the calculated band structure, projected onto the positive k -halfspace shown as dots.

in the surface layer is visible, which is marked by green triangles in Fig. 4.9(a). This band starts at -0.4 eV and has a mass of about $1.5 m_e$.

A close-up view of the surface state region is shown in Fig. 4.9(c). Interestingly the calculation yields two branches for the state which are split by about 100 meV except near $\bar{\Gamma}$, where the splitting goes to zero. The reason is a spin-orbit coupling induced spin splitting as already discussed in Sec. 4.1. Therefore each branch represents one spin state: spin 1 and spin 2, respectively. In the present case, Δk is about 0.02 \AA^{-1} at energies below 0.8 eV. This value is comparable to the case of Au(111) which one would expect due to a similar nuclear charge (see Sec. 4.1) [53]. Furthermore, the analysis of the presented calculations show, that the shift in k is not the only difference between both branches: The lower Rashba-split surface state (spin 2) gently merges into the bulk continuum and therefore loses weight in the vacuum. As visible in Fig. 4.9(c) the surface state criterion is no longer fulfilled at about 0.8 eV where the spin 2 surface-state changes to a surface resonance.

In order to reveal the origin of the features in the measured dI/dU -spectra the vacuum LDOS at a distance of about 4 \AA has been calculated and is shown in Fig. 4.7(b). In total three features are observable: A broad peak at E_F , a rising edge at about 0.3 eV followed by a slope reduction at higher energy as well as a faint peak at around -0.4 eV. Concerning the peak at E_F , the bandstructure

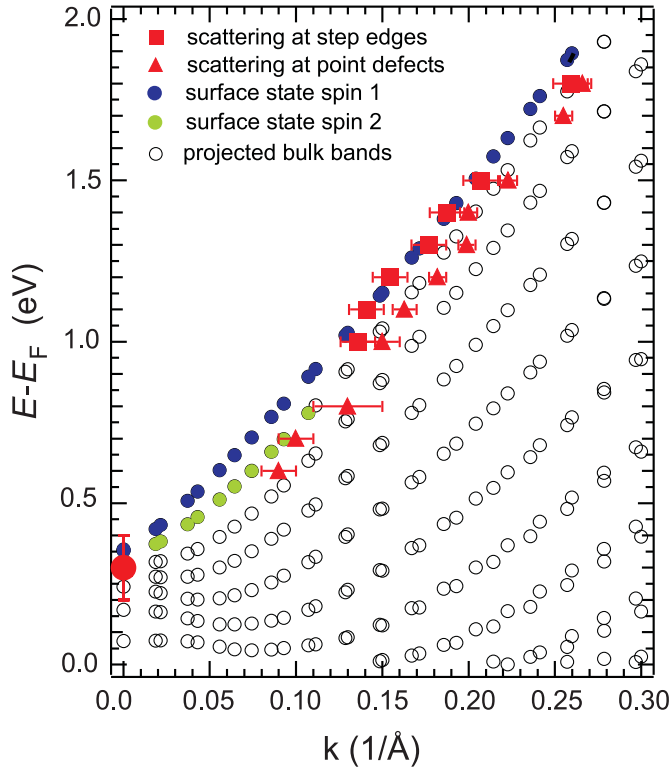


Figure 4.10: Experimental dispersion from scattering at steps (squares) and point defects (triangles) in comparison to the calculated bandstructure.

calculations show that a couple of bulk states have a significant contribution to the calculated surface LDOS at this energy. Therefore the peak at E_F in the calculated LDOS can be attributed to the rather flat d_{zx}, d_{yz} -like bulk bands at $\bar{\Gamma}$ with a localization of about 10% in the surface layer. A further comparison to the band-structure shows that the rising edge at +0.3 eV originates from the onset of the surface-state band. Finally, the peak around -0.4 eV originates from the upwards dispersing, occupied bulk band with an effective mass of $1.5 m_e$ and a 10% localization in the surface layer, indicated in Fig. 4.9(a). This bulk state is probably the one which was previously found by photoemission experiments exhibiting an effective mass of $1.3 m_e$ and has been assigned to an occupied surface state [66, 67]. As obtained from the calculations, it has d_{yz}, d_{zx} -like symmetry. This symmetry together with the weak dispersion could explain the sensitivity to oxygen which lead to the wrong assignment to a surface state as found in a photoemission experiment [66, 67].

4.5 Discussion

A comparison of the experimental data and the calculated band-structure in Fig. 4.10 reveals a striking agreement of the measured dispersion and the calculated surface state within the error bars. Interestingly, the data obtained from

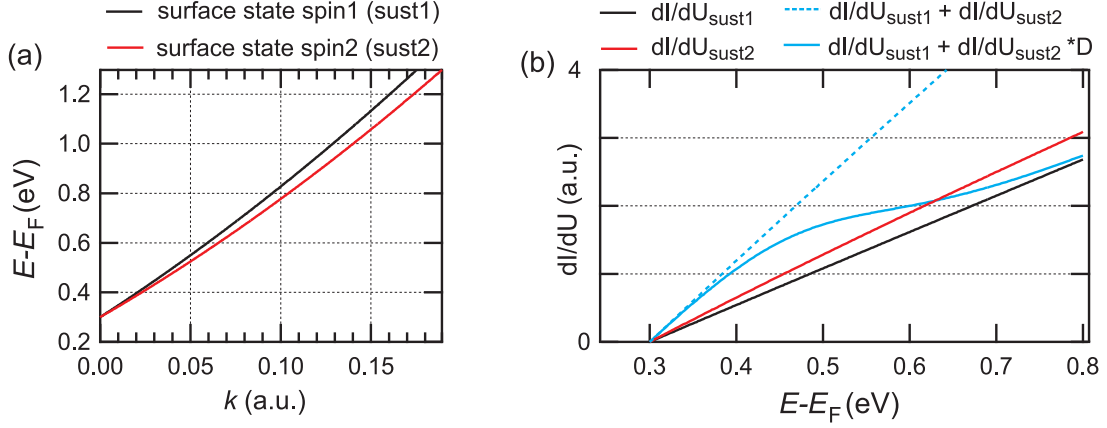


Figure 4.11: (a) Dispersion of a spin-split surface state with a large linear contribution for each spin branch. ($E_0 = 0.3$ eV, $\alpha = 5.59$ eVÅ², $\beta_{\text{sust2}} = 4.21$ eVÅ, $\beta_{\text{sust1}} = 4.71$ eVÅ), (b) Corresponding numerical dI/dU signal for each branch as well as for the weighted and unweighted sum. D denotes the weighting function which lowers the contribution of dI/dU_{sust2} to the sum for higher energies.

step edge scattering seemingly fits to the spin 1 branch, while the point defect data fits to the spin 2 branch. The reason for this small but systematic deviation is unknown so far. Anyhow, one can conclude that the imaged scattering states are due to this *sp*-derived surface state. On the other hand, theoretical predictions indicate, that the influence of the spin splitting on the scattering states cannot be observed by STS and only the mean value of the two branches enters into the measured dispersion [54].

Concerning the electronic structure, the broad peak at E_F and the rising edge at about 0.3 eV, followed by a slope reduction are well reproduced by the calculation as shown in Fig. 4.7. In contrast, the upwards dispersing, occupied bulk band starting at -0.4 eV is not always found in the measurements with different tips. Only two of the three spectra shown in Fig. 4.7(a) reveal a broad peak near -0.4 eV. A reason for these differences might be the influence of the tip LDOS, which could hide the peak originating from this bulk band.

The shape of the feature, which indicates the onset of the Pt surface state, is very different from the noble metal case. As described in Sec. 4.1 a sharp step-like rise with a width of only a few tens of a meV marks the onset of the surface-state band in the noble metal case [79]. The reason for this sharp step is the nearly parabolic dispersion, which indicates that the two-dimensional free-electron gas is a good approximation for the (111) surface of noble metals. This is obviously different for the present case. For the Pt(111) surface the spin-orbit splitting and the interaction of the surface state with nearby bulk states results in a strong linear contribution to the dispersion which induces a nearly linear rise

in dI/dU spectra at the onset of the surface-state band (see Sec. 4.1). This is visible in the measured as well as calculated LDOS in Fig. 4.7(a) and (b). In order to show that the loss of vacuum DOS for the lower spin branch leads to the slope reduction at about 0.4 eV, a simulation has been performed. Figure 4.11(a) shows the dispersion of a surface state with a strong linear contribution which is additionally spin-split similar to the experimental case. In Fig. 4.11(b) the corresponding numerical dI/dU signals are shown which have been obtained as described in Sec. 4.1. If both spin branches contribute equally to the total dI/dU signal, the dashed line in Fig. 4.11(b) would give the resulting dI/dU signal. A damping function $D = 1/(1 + \exp((E - E_F - E_C)/\delta))$ describes the loss of vacuum DOS for higher energies for `sust2` which is lower in energy and therefore closer to the bulk states. The resulting dI/dU signal (solid line) shows the rising edge as well as the slope reduction and is therefore in a good qualitative agreement to the experimental as well as theoretical results.

In other words, the appearance of the onset of the surface state in dI/dU spectra as a step with a width of about 100 meV is resulting from two facts. First, from the linear dispersion and second from the merging of one band of the spin-split surface state into the bulk continuum. Therefore the appearance as a broad step is intrinsic due to the electronic properties of Pt(111) and not due to other broadening effects as life time effects or due to measurement parameters.

4.6 Summary

In summary, the dispersion of an unoccupied surface state starting at 0.3 eV above the Fermi energy was determined on Pt(111). The measured dispersion has a strong linear contribution. Comparison to density functional theory calculations shows that the *sp* derived surface state is located just at the bottom of the projected bulk band-gap and exhibits a strong spin-orbit coupling induced spin splitting. The calculations yield no surface state below E_F . Concerning the surface band structure, Pt(111) is thus quite similar to Pd(111).

5 Co nanostructures on Pt(111)

This chapter reports on spin-resolved scanning tunneling spectroscopy measurements of Co nanostructures on Pt(111) at low temperatures. On Co monolayer islands and wires the spin-resolved electronic structure changes on the scale of a few atoms due to the changing local stacking of the Co-atoms. First-principle calculations for pseudomorphic fcc and hcp stacked Co monolayers assign the dominant feature in the occupied density of states to a d -like surface resonance of minority-spin character which shifts in energy because of a different coupling to the Pt substrate.¹ Also for the Co double-layer islands we observe shifts in energy of the peaks in the electronic structure below the Fermi energy depending on the local stacking of the islands. Despite the heterogeneous electronic structure of the Co monolayer, the out-of-plane magnetized domains are clearly observed. While the domain wall width measured on wires is less than 4 nm there is no indication for a change in the magnetization direction for islands with a base length up to fifteen times the domain wall width. Furthermore, the magnetic hysteresis in an ensemble of out-of-plane magnetized Co monolayer as well as double-layer nanostructures was observed. While the coercivity for the monolayer nanostructures is about 0.25 T, double-layer islands show surprisingly large coercivities of more than 2 T.

This chapter is organized as follows: After an introduction, Sec. 5.2 gives a brief description of the experimental setup as well as tip and sample preparation. In Sec. 5.3 the spatially resolved electronic structure of oppositely magnetized Co monolayer islands and wires and its correlation to the local stacking is shown. These measurements are compared to first-principle calculations of extended pseudomorphic hcp and fcc Co monolayer films on Pt(111). In Sec. 5.4 the spatially resolved electronic structure of oppositely magnetized Co double-layer islands is presented. Finally, in Sec. 5.5 we discuss the response of Co monolayer and double-layer nanostructures to an external magnetic field.

5.1 Introduction

Cobalt nanostructures on noble metal substrates provide interesting model systems to study magnetic properties in reduced dimensions [4, 7, 8, 80–83]. In par-

¹fcc and hcp denote the crystal lattice structures *Face-Centered Cubic* and *Hexagonal Close-Packed*, respectively.

ticular the system Co/Pt(111) has received great attention due to its potential application in magnetic recording media. Recently a number of experimental reports have demonstrated the significant interest in the exciting magnetic properties of low-dimensional Co structures on Pt(111): Gambardella *et al.* showed how magnetic properties like coercivity and anisotropy can be changed for low dimensional Co structures like single atoms and wires [4,8]. The experiments on single Co atoms located on Pt(111) terraces reveal a giant magnetic out-of-plane anisotropy while the magnetic orientation of ferromagnetic Co wires decorating Pt step edges is canted with respect to the surface normal [4,8]. Furthermore, an increase of the width of the Co wires leads to significant changes of the anisotropy direction and the coercivities [9]. Measurements performed on nano-scale monolayer (ML) high Co islands on Pt(111) by Rusponi *et al.* reveal an out-of-plane anisotropy of these structures which is stabilized to a large extent by the perimeter atoms [7]. These interesting results strikingly demonstrate that the magnetic properties of structures in the nanometer range cannot be rationalized without taking into account the dimensionality, size, shape, environment, and interface structure. While most of the experimental results on Co/Pt(111) samples were obtained by spatially averaging methods based on the magneto-optical Kerr effect (MOKE) and X-ray magnetic circular dichroism (XMCD), there is only one recent spin-sensitive scanning tunneling microscopy (STM) study which was able to distinguish double-layer islands with opposite out-of-plane magnetization orientations [84].

However, already Co monolayer and double-layers on Pt(111) have proven to be complicated systems on the atomic scale. A detailed insight into the growth and the structural properties of ultrathin Co films on Pt(111) has been obtained by STM experiments at room temperature [85,86]. Lundgren *et al.* [86] studied the dislocation network of the Co monolayer on Pt(111), which is formed due to the lattice mismatch of 9.4% between Pt and Co. They observed that the Co atoms preferentially occupy fcc sites while a much smaller number of Co atoms was found on hcp sites. To relieve the strain structural domain walls are introduced consisting of Co atoms in bridge site positions. From the second to the sixth atomic layer a Moiré structure is observed [85,86]. These results indicate a spatially inhomogeneous electronic structure, which has direct impact on the magnetic properties of both systems.

The previous STM experiments did not include electronic structure measurements, and we are not aware of such a study performed for Co ultrathin films on Pt(111) at all. Only one recent scanning tunneling spectroscopy (STS) study on single Co atoms on Pt(111) showed a spectroscopic difference of Co atoms occupying different stacking sites [87]. This is also consistent with our experimental results on the same sample system as described in Chap. 6. Moreover, we could conclude that the single Co atoms show a peak in the occupied LDOS which is shifted downwards for Co atoms on hcp sites relative to those on fcc sites. This

already demonstrates, that stacking is very important for the local electronic properties of this sample system. Also investigations of Co nanostructures on other substrates have shown some interesting properties which may be of importance for the sample system Co/Pt(111) on which this work is focused. For instance, experiments revealing the electronic structure of Co nanostructures and films were performed on Co islands on Cu(111) [80, 81, 88], on Co/Cu/Co sandwiches [89] and on ultrathin as well as thick Co films on W(110) [90–92] by STS. For Co islands on Cu(111) and Co films on W(110) it was possible to distinguish islands and more extended areas of different stacking spectroscopically [81, 88, 90, 92]. In addition, by performing first-principles electronic structure calculations, Wiebe *et al.* [92] showed that this observation can be explained by a different coupling strength of the Co surface resonance to the bulk states. This surface resonance showed up as a dominant peak in the dI/dU spectra below the Fermi energy E_F at about -0.3 eV [80, 81, 89, 92]. Apart from the correlation between structural and electronic properties Pietzsch *et al.* [81] probed the magnetic state of Co islands by spin-resolved STS. Besides a large energy-dependent spin-polarization they found a perpendicular magnetization of the Co islands and a coercivity between 1.0–1.5 T by measuring in the presence of variable external magnetic fields. To gain further insight into the interplay between structural, electronic, and magnetic properties of Co nanostructures on Pt(111) we performed an extensive study on monolayer Co islands and wires and Co double-layer islands. In addition we studied the magnetic properties of these nanostructures. We applied the experimental method of spin-polarized (SP)-STM, which combines a very high lateral resolution with magnetic sensitivity and gives access to the local electronic structure [93].

5.2 Experimental details

All experiments were performed in a multi-chamber UHV system [94], which is different from that described in Chap. 3. It contains a home-built scanning tunneling microscope operating with tip and sample held at $T = 13 \pm 1$ K and several standard devices for preparation and analysis of samples and tips. Using a superconducting split-coil magnet a maximum magnetic field B of 2.5 T perpendicular to the sample surface is available. The base pressure of the system is in the low 10^{-11} mbar range.

For the measurements presented in this Chapter the Pt(111) surface was prepared by cycles of Ar⁺-ion sputtering at room temperature and subsequent annealing at 1500 K for 4 min. Occasionally, an additional annealing at 1000 K in an oxygen atmosphere of $3 \cdot 10^{-7}$ mbar was carried out for 20 min. For monolayer high nanostructures Co was deposited on the clean Pt(111) surface from a rod in a water-cooled e-beam evaporator at room temperature. A typical deposition rate was 0.4 atomic layers (AL) per minute. We define a coverage of one AL

as a complete coverage of the Pt substrate with Co atoms. The preparation of double-layer Co islands on the Pt surface is described in the literature [7]: First depositing Co on Pt(111) at 130 K and then annealing to 340 K leads to well-separated Co double-layer islands while no Co monolayer areas remain. Since the experimental setup of the present study does not allow for cooling of the substrate in the deposition position, the Pt crystal is pre-cooled in the microscope to 13 K and then transferred to the metal deposition chamber. The typical transfer time between the microscope and the Co deposition position amounts to 4 minutes. Since the growth mode differs significantly from that at room temperature we conclude that the sample temperature is still well below 300 K. As a result of the lower surface temperature a higher island density is observed due to the reduced diffusion length. After Co deposition the sample is slightly annealed [7].

5.3 Structure and spin-resolved electronic properties of monolayer Co wires and islands

5.3.1 Experimental results

Figure 5.1(a) shows a topographic image of 0.3 AL Co deposited on Pt(111) at room temperature. On the terrace one atomic layer high Co islands are observed coexisting with one atomic layer high Co wires at the step edges. The Co islands are triangularly shaped with a base length from 60 nm down to a few nm. All islands point in the same direction and some larger ones already show the nucleation of the second atomic layer on top. The faint lines visible on the Pt substrate which are indicated by the arrows can be identified as Co induced double row reconstruction lines [85,95]. The inset shows the area marked by the white rectangle at a closer view and displays the characteristic two parallel bright lines on the Pt substrate. The existence of this kind of reconstruction is indicative of the incorporation of Co atoms into the topmost Pt layer [95]. Since it is known that the double row reconstruction lines run along $\langle 11\bar{2} \rangle$, i.e. perpendicular to closed-packed rows, we can conclude that all edges of the Co islands as well as of the Co wires are parallel to the closed-packed rows. Furthermore, it can be observed that the roughness of the Co wires is smaller when the Pt step edge runs along a closed-packed row, as seen in the bottom right part of Fig. 5.1(a).

Figure 5.1(b) shows two slightly truncated triangular shaped Co islands. Both exhibit an almost voltage independent narrow dislocation network on top which is always found for Co monolayer islands as well as wires. Figure 5.1(c) displays a magnified view of the area marked by the box in (b) and reveals that the network is formed by brighter lines with a relative height of about 10 pm. The same network has been found in a previous STM study on Co monolayer films on Pt(111) [86]. It is due to inhomogeneous stacking of the Co atoms caused by the strain of the

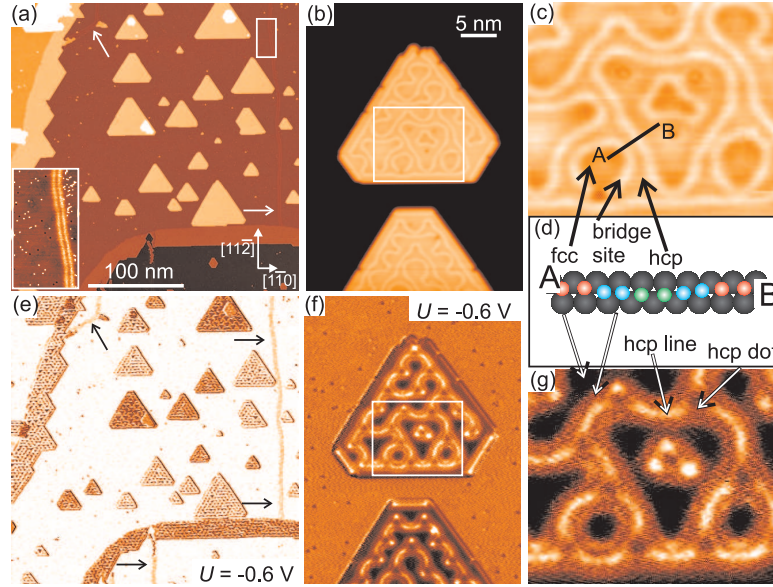


Figure 5.1: Co monolayer islands and wires prepared by Co deposition on the Pt(111) surface at room temperature. Upper panels (a)-(c): Topographic images. Inset in (a): Magnified view of the Co induced double row reconstruction lines. (d) Sketch of the different stacking along the line drawn in (c) (inspired by Ref. [86]). Lower panels (e)-(g): dI/dU maps measured simultaneously to the topographic images of the upper panel with an out-of-plane sensitive magnetic Fe-coated tip ($I = 1.0$ nA, $U_{\text{mod}} = 20$ mV).

overlayer. This strain is induced by the mismatch of -9.4% between the Co and the Pt lattice and relieved by the formation of dislocation lines. According to Ref. [86] the Co atoms preferentially occupy the fcc sites of the Pt lattice. The dislocation lines appear slightly higher and are formed by Co atoms taking bridge-sites separating fcc and hcp stacked regions. Taking these results into account we can assign the more extended areas visible in Fig. 5.1(c) to fcc areas while the brighter lines are formed by Co atoms occupying bridge-sites. Furthermore, the narrow areas in between the lines consist of Co atoms in hcp positions of the Pt lattice. Figure 5.1(d) sketches the local stacking of the Co atoms below the line drawn in (c) which connects two fcc regions while passing two bridge-site lines and one narrow hcp area. The smallest distance between two bridge-site lines is about 8 ± 1 Å, which leads to very narrow hcp regions of only a couple of atoms (For the Pt(111) surface the nearest neighbor distance is 2.77 Å).

Figure 5.1(e) shows an out-of-plane sensitive magnetic dI/dU map recorded simultaneously to Fig. 5.1(a). The Pt surface appears homogeneous except above the Co induced double row reconstruction lines indicated by arrows. Above the

Co wires and islands a dominating two color contrast in the dI/dU signal is found. Since all Co wires as well as all islands have an identical spin-averaged electronic structure we ascribe the origin of this contrast to oppositely magnetized domains of the Co monolayer. We conclude that the Co monolayer has an easy axis normal to the surface plane in agreement with former results obtained by spatially averaging methods for Co on Pt(111) in the submonolayer regime ² [7, 9, 96]. This will be proven in Sec. 5.5. The relative magnetization direction of the Co nanostructures can easily be deduced from the dominant colors of the wires and single domain islands. In addition to the magnetic contrast the appearance of the dI/dU signal above the nanostructures appears to be highly heterogeneous. A comparison of the dI/dU map of two oppositely magnetized single domain islands in (f) to the simultaneously recorded topographic image (b) reveals that these small scale variations of the dI/dU signal are directly correlated to the reconstruction due to the strain relief. In order to investigate this correlation in more detail Fig. 5.1(g) shows a magnified view of the regions marked in (f). By comparing this dI/dU map (g) to the corresponding topography in (c) each dI/dU level can directly be assigned to the local stacking of the atoms: While fcc and hcp areas show the same height in topography, both stackings show different dI/dU intensities and can easily be distinguished. At the applied bias voltage of -0.6 V the highest dI/dU intensity is obtained for the hcp-lines followed by the signal above the bridge site lines while the fcc-areas show the lowest intensity. Interestingly, we can identify a fourth distinct area in dI/dU which has not been seen in the topography. This fourth distinct area is located at positions where three hcp lines come together and will be called hcp-dot in the following. By comparing the two oppositely magnetized islands in Fig. 5.1(f) it becomes obvious that the four stackings are also observed for the lower island. However, due to the different magnetic state they show different absolute dI/dU intensities compared to the stackings on the upper island.

In general we observed the magnetic contrast in dI/dU maps on this sample system within a wide range of voltages from $+1$ V down to -1 V, though the strength as well as the sign of the magnetic contrast varied. Figure 5.2(a) shows the topographic image of five Co monolayer wires attached at Pt step edges. The out-of-plane sensitive magnetic dI/dU maps in Fig. 5.2(b)–(g) clearly reveal that the wires, which are attached to the second and fifth Pt terraces, exhibit an opposite magnetic orientation in comparison to the remaining ones. Additionally, we observe scattering on the Pt terraces in Figs. 5.2(b) and (c) due to the Pt(111) surface state (see Chap. 4). While differences in the apparent height of oppositely magnetized wires are difficult to observe in a section from the topography in (a) as shown in Fig. 5.2(h), this becomes possible in histograms of the height. Fig. 5.2(i) shows histograms of a selected area for each topographic image recorded

²The easy axis refers to the energetically favorable direction of the magnetization.

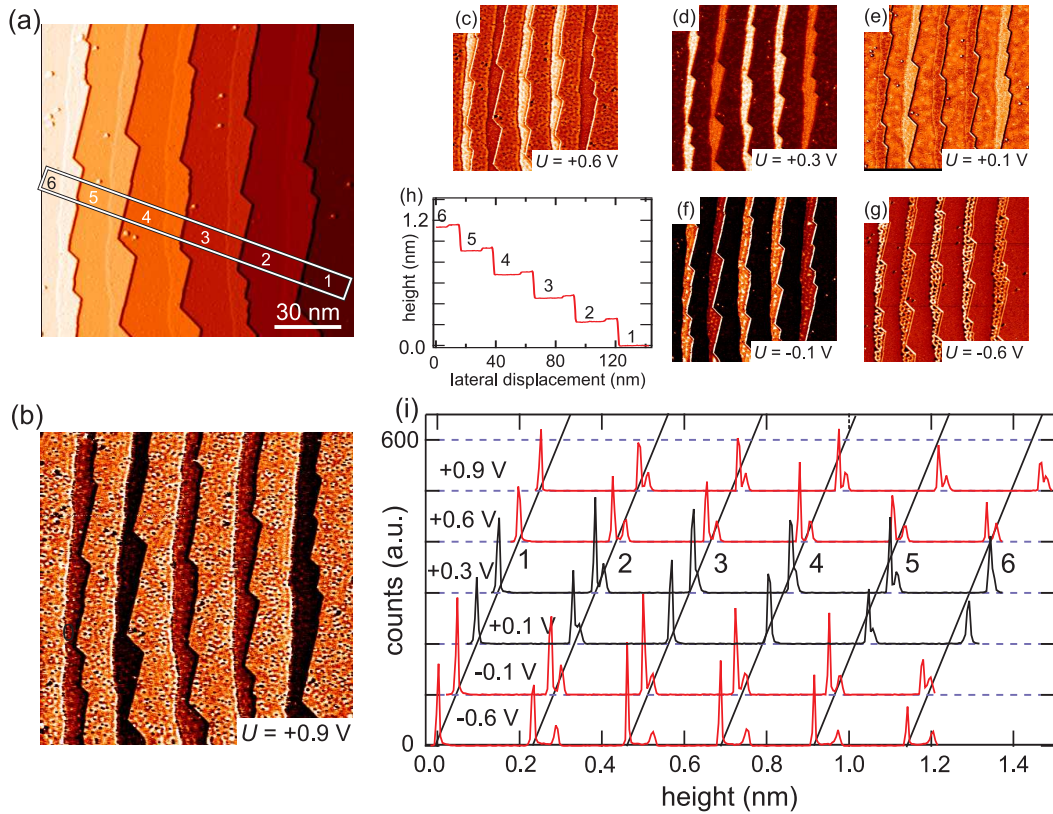


Figure 5.2: Co monolayer wires prepared by Co deposition on the Pt(111) surface at room temperature. (a) Topographic image (partly differentiated). (b)–(g) dI/dU maps measured with out-of-plane sensitive Cr-coated tip at indicated voltages ($I = 1.0$ nA, $U_{\text{mod}} = 20$ mV). (h) Section along the rectangle indicated in (a). (i) Histograms of the area marked in (a) for each topographic image recorded simultaneously to dI/dU maps in (b)–(f). In contrast to the red curves the black curves shows differences of the height of Co wires due to parallel or antiparallel orientation with respect to the tip magnetization.

simultaneously to the corresponding dI/dU maps in Fig. 5.2(b)–(g). The highest peaks in each histogram reflect the Pt terraces, while the smaller satellite peaks belong to the corresponding attached Co wire. The distance between the Co satellite peak and the corresponding Pt peak gives the relative height of each Co monolayer wire for each applied voltage. It can be seen that differences in height due to parallel or antiparallel orientation with respect to the tip magnetization are only observed for +0.3 V and +0.1 V. At these voltages the position of the Co satellite peak of the second and the fifth Co wire relative to the Pt peak is significantly different from the others. A closer inspection reveals that these Co

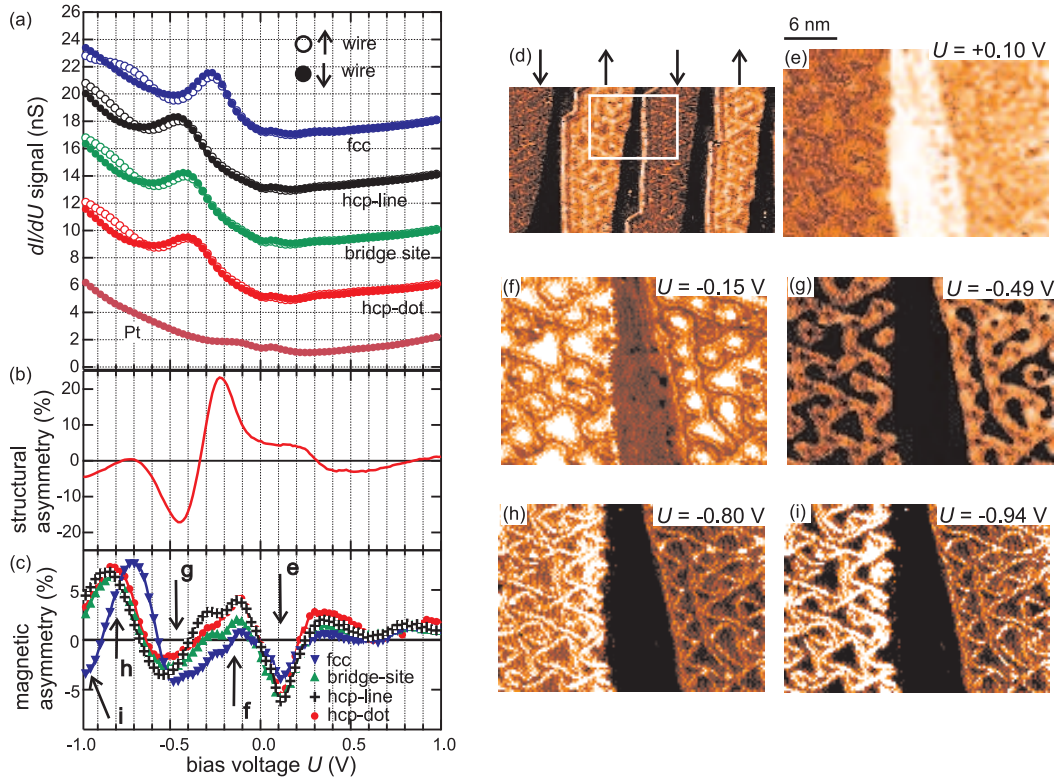


Figure 5.3: (a) Spin- and stacking-resolved dI/dU spectra on Co monolayer wires. Open and filled circles mark spectra taken on the upward and downward magnetized wire, respectively. The area of the spectroscopy measurement is indicated by the white rectangle in (d). For the stacking refer to Fig. 5.1(d). All Co spectra are offset by multiples of 4 nS. (b) Structural asymmetry between spin averaged fcc and hcp-dot spectra. (c) Magnetic asymmetry between upward and downward Co monolayer wires for different stacking. (d) dI/dU map of alternately out-of-plane magnetized Co wires. (e)–(i) Selected spin-resolved dI/dU slices of the STS field ($I_{\text{stab}} = 1.5$ nA, $U_{\text{stab}} = +1.0$ V, $U_{\text{mod}} = 20$ mV, Cr-coated tip).

wires have a height which is 15 pm larger than that of the oppositely magnetic wires. Extraordinary height differences of up to 100 pm as found on Co double-layer islands by Rusponi *et al.* [84] were not observed in our experiment.

In order to get access to the spin- and energy-resolved electronic structure of the different stackings we performed spatially and spin-resolved STS which is shown in Fig. 5.3. The very high lateral resolution of the spectroscopic field enables us to assign the spectra taken above the Co monolayer atoms to a certain stacking sequence. Figure 5.3(d) shows a dI/dU map of alternately out-of-

plane magnetized Co wires. The area where the spin-resolved dI/dU spectra were taken, is indicated by the white rectangle. Although the absolute orientation of the magnetization is unknown, we arbitrarily mark the wires by arrows and refer to upwards and downwards magnetized wires in the following. Figure 5.3(a) shows the dI/dU spectra obtained above the four different Co stackings on each wire and the spectrum above the bare Pt substrate (all obtained by averaging approximately 30 spectra). The Pt spectrum shows no outstanding spectroscopic features apart from a gently increasing dI/dU signal in the negative voltage range. The onset of the surface state described in Chap. 4 is only faintly visible on this scale. All dI/dU spectra of the Co monolayer are also rather featureless in the positive voltage range. However, in contrast to the Pt spectrum they show a pronounced feature below E_F , with the peak energy depending on the specific stacking of the atoms. Independent of their magnetization direction, fcc-stacked Co atoms of monolayer wires reveal a dominant peak located around 0.28 eV below E_F . Additionally, a small feature can be observed for the fcc spectrum obtained on the upward magnetized wire at -0.70 eV. In the spectra of the hcp- and bridge-site lines the dominant peak is shifted to -0.48 eV and -0.42 eV, respectively, while the peak of hcp-dot is located at -0.40 eV. In addition to variations originating from different stackings we observe spectroscopic differences due to the different magnetization directions, i.e. between the upward and downward magnetized wire. While these are generally small in the positive voltage range, we observe larger deviations close to the characteristic peak and in the energy range towards more negative bias voltages for all four different stackings.

In order to distinguish the spectroscopic differences due to a different stacking from those due to different magnetization, we calculate the structural asymmetry A_{struc} and the magnetic asymmetry A_{magn} of the spectra. The structural asymmetry is defined by

$$A_{\text{struc}} = \frac{dI/dU_{\text{fcc}} - dI/dU_{\text{hcp}}}{dI/dU_{\text{fcc}} + dI/dU_{\text{hcp}}}, \quad (5.1)$$

with dI/dU_{fcc} and dI/dU_{hcp} representing the calculated spin-averaged spectra of fcc and hcp regions, respectively. The magnetic asymmetry is defined by

$$A_{\text{magn}} = \frac{dI/dU_{\uparrow} - dI/dU_{\downarrow}}{dI/dU_{\uparrow} + dI/dU_{\downarrow}}, \quad (5.2)$$

with dI/dU_{\uparrow} and dI/dU_{\downarrow} representing the spin-resolved dI/dU spectra of the upward and downward magnetized wire for each stacking, respectively. Figure 5.3(b) shows exemplarily the structural asymmetry between the fcc and hcp-dot regions which confirms the impression that significant differences in dI/dU are located below E_F while the electronic structure in the positive voltage range is mostly stacking independent. The highest structural asymmetry values of around 20% are observed close to the energetic positions of the dominant peaks of the fcc

and hcp-dot spectra. The magnetic asymmetries for each stacking are shown in Fig. 5.3(c). In the negative voltage range the magnetic asymmetries for the Co monolayer are higher than in the positive voltage range. They show distinct minima at about -0.50 eV and larger maxima around -0.80 eV. It appears as if the fcc asymmetry is compressed towards E_F compared to the other asymmetries. This leads to a shift of the minimum and the maximum in the fcc magnetic asymmetry towards E_F by about 0.1 eV. This shift goes along with the corresponding shift of the peaks observed in the dI/dU spectra for the fcc areas towards E_F . As a result the sign of the magnetic asymmetry is reversed for fcc regions compared to the other stackings below -0.9 eV. It is worth to mention that although the spin polarization of the tip states also influences the measured spin polarization, a different sign of the magnetic asymmetry at the *same* energy leads to the conclusion that the sample spin polarization is indeed inverted for fcc stacking relative to hcp stacking at energies below -0.9 eV.

In order to visualize the interplay between structural and magnetic asymmetry we display dI/dU slices at selected energies in Figs. 5.3(e)-(i), the corresponding voltages are indicated in Fig. 5.3(c). The first slice in Fig. 5.3(e), which is taken in the positive voltage range at $+0.10$ eV, shows only very weak influence of the stacking in accordance with the small structural asymmetry (cf. Fig. 5.3(b)). In contrast, as a consequence of the different magnetic orientation of the wires, the dI/dU signal shows a difference between the upward and the downward magnetized wire. Figs. 5.3(f) and (g) show slices at -0.15 eV and at -0.49 eV, respectively, where the structural asymmetry is strongest. While at -0.15 eV the fcc areas exhibit the highest dI/dU intensity, the bridge sites and hcp lines show the highest intensity at -0.49 eV. This is in agreement with the inverted structural asymmetry between -0.20 eV and -0.50 eV as plotted in (b). The different magnetization of the wires is only slightly visible at these energies. Figs. 5.3(h) and (i) finally display slices at -0.80 eV and -0.94 eV, respectively. At -0.80 eV the intensity of each stacking of the upward magnetized wire is higher than that on the downward magnetized wire. This is not the case at -0.94 eV, where the bridge site lines exhibit a higher intensity on the upward than on the downward magnetized wire, while the fcc areas have a lower intensity on the upward than on the downward magnetized wire. This peculiar contrast reversal visualizes the already mentioned inversion of the sample spin polarization for fcc areas with respect to the other stackings at about -0.90 eV.

Up to this point we can conclude that the electronic structure of the Co monolayer on Pt(111) changes significantly between the areas of the four different atom positions on a length scale of only a few atoms. The main change in the electronic structure is a shift of the dominating peak in the negative voltage range, which appears at -0.28 eV on the fcc areas and is shifted to lower energies for the other three stackings. Despite this strong heterogeneous electronic structure it is possible to deduce the magnetic orientation of the Co monolayer using the magnetic

asymmetry of the spin-resolved dI/dU spectra.

5.3.2 Theoretical results

In order to understand the origin of the spectroscopic difference between fcc and hcp stacking of the Co monolayer on Pt(111), we have performed first-principles calculations using the full-potential linearized augmented plane wave (FLAPW) method in film geometry as implemented in the FLEUR code [97].³ The system has been modeled by a symmetric 13-layer Pt slab with the experimental Pt in-plane lattice constant of 2.775 Å and an additional Co layer on both sides. We have applied the generalized-gradient approximation of Perdew, Burke, and Ernzerhof [98]. Self consistency for the charge density has been obtained with about 100 basis functions per atom and 44 \mathbf{k}_{\parallel} points in the irreducible wedge of the two-dimensional Brillouin zone (I2BZ). 81 \mathbf{k}_{\parallel} points in the I2BZ have been used for the calculation of the density of states (DOS).

The surface relaxation for the pseudomorphic Co layer in both fcc and hcp stacking has been carried out by force minimization. We obtained an equilibrium Co-Pt interlayer distance of 2.053 Å for hcp and 2.038 Å for fcc stacking, corresponding to an inward relaxation of 9.4% and 10.1%, respectively, compared to the bulk Pt interlayer distance. The fcc stacking of the Co layer is energetically more favorable by 67.4 meV per Co-atom than the hcp stacking. The magnetic moment of the Co atom was found to be 2.07 μ_B and 2.10 μ_B for fcc and hcp, respectively.

We applied the Tersoff-Hamann model to simulate the spectroscopic measurements. The differential conductance dI/dU is then proportional to the sample DOS in the vacuum at the position of the tip apex [17]. The results for the majority and minority spin channels as well as the sum of both are presented in Fig. 5.4(a) for a tip-sample distance of 6.7 Å. The vacuum DOS in the energy range around the Fermi level is dominated by spin-minority states. The main minority peaks are found at $\varepsilon_{\text{fcc}} = -0.175$ eV and $\varepsilon_{\text{hcp}} = -0.250$ eV for the fcc and hcp structure, respectively, corresponding to a shift of $\Delta\varepsilon = 0.075$ eV.

Since the analysis of the band structure alone is not sufficient to unambiguously pin-point the electronic states contributing to the spectroscopic features, we have decomposed the vacuum DOS $n^{\downarrow}(\varepsilon)$ as a function of the in-plane k-vector \mathbf{k}_{\parallel} : $n^{\downarrow}(\varepsilon, \mathbf{k}_{\parallel})$. We focus on the energies corresponding to the main peaks of the vacuum DOS for the minority spin in the two stackings, i.e. ε_{fcc} and ε_{hcp} (indicated by the dash-dotted lines in Fig. 5.4(a)). The results are shown in Fig. 5.5, where $n^{\downarrow}(\varepsilon, \mathbf{k}_{\parallel})$ has been plotted only in the vicinity of $\bar{\Gamma}$, as sketched in the inset, because of the \mathbf{k}_{\parallel} -dependent exponential decay of the electronic states in the vacuum. At ε_{hcp} , we observe in Fig. 5.5(a) and (b) for both fcc and hcp that the main contribution to

³The calculations were performed by Paolo Ferriani and Stefan Heinze from the *Spin Theory Group* in Hamburg.

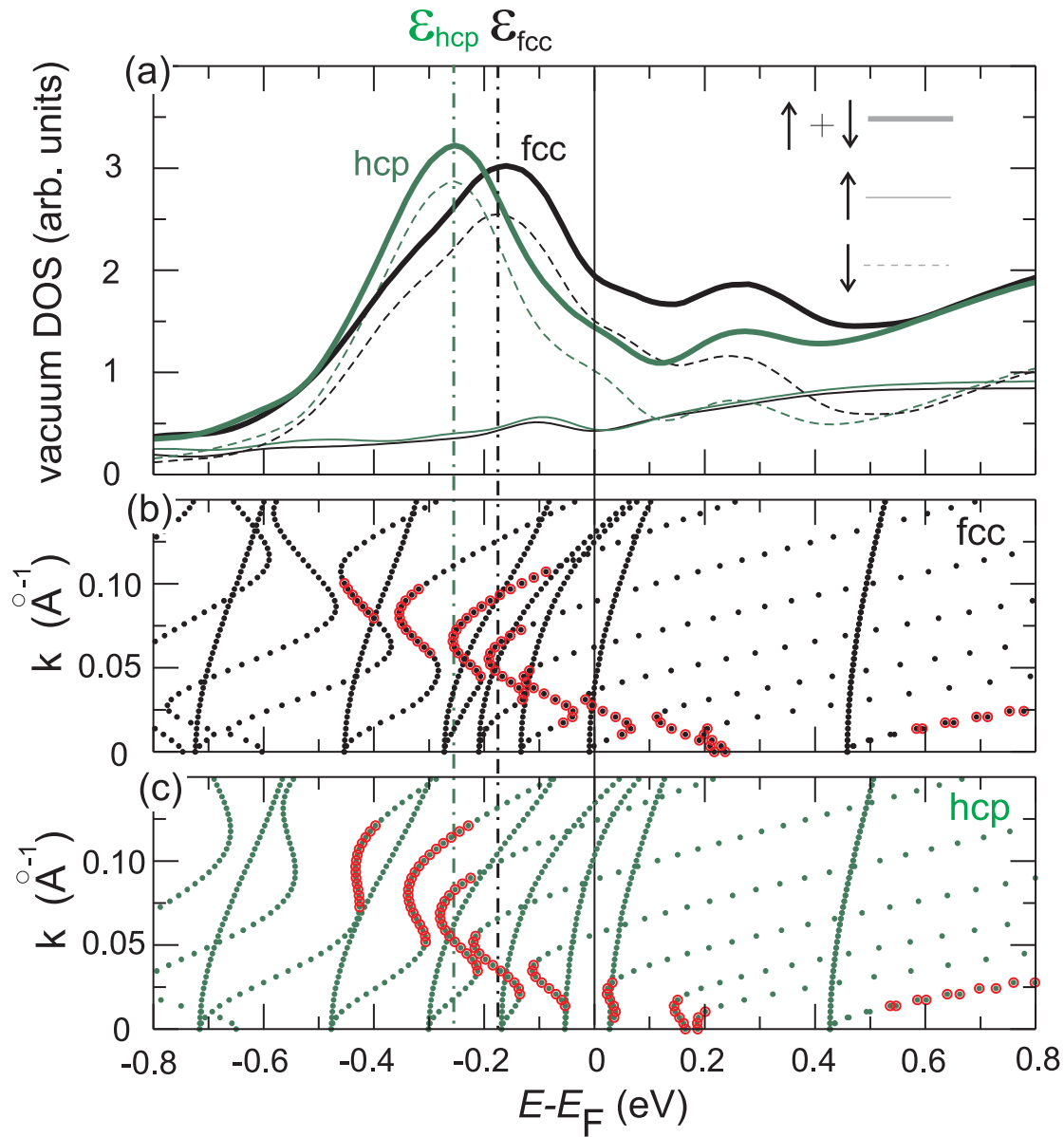


Figure 5.4: (a) Vacuum DOS for fcc (black) and hcp (green) stacking of 1 ML Co on Pt(111) at a distance of 6.7 \AA from the surface. The spin-majority (thin solid line), spin-minority (thin dashed line) contribution and the sum of both (thick solid line) are shown. The spin-minority electron band structure along the $\bar{\Gamma} - \bar{M}$ line is plotted for the fcc (b) and hcp (c) stacking near the $\bar{\Gamma}$ point. States with a localization of more than 5% in the vacuum are marked in red.

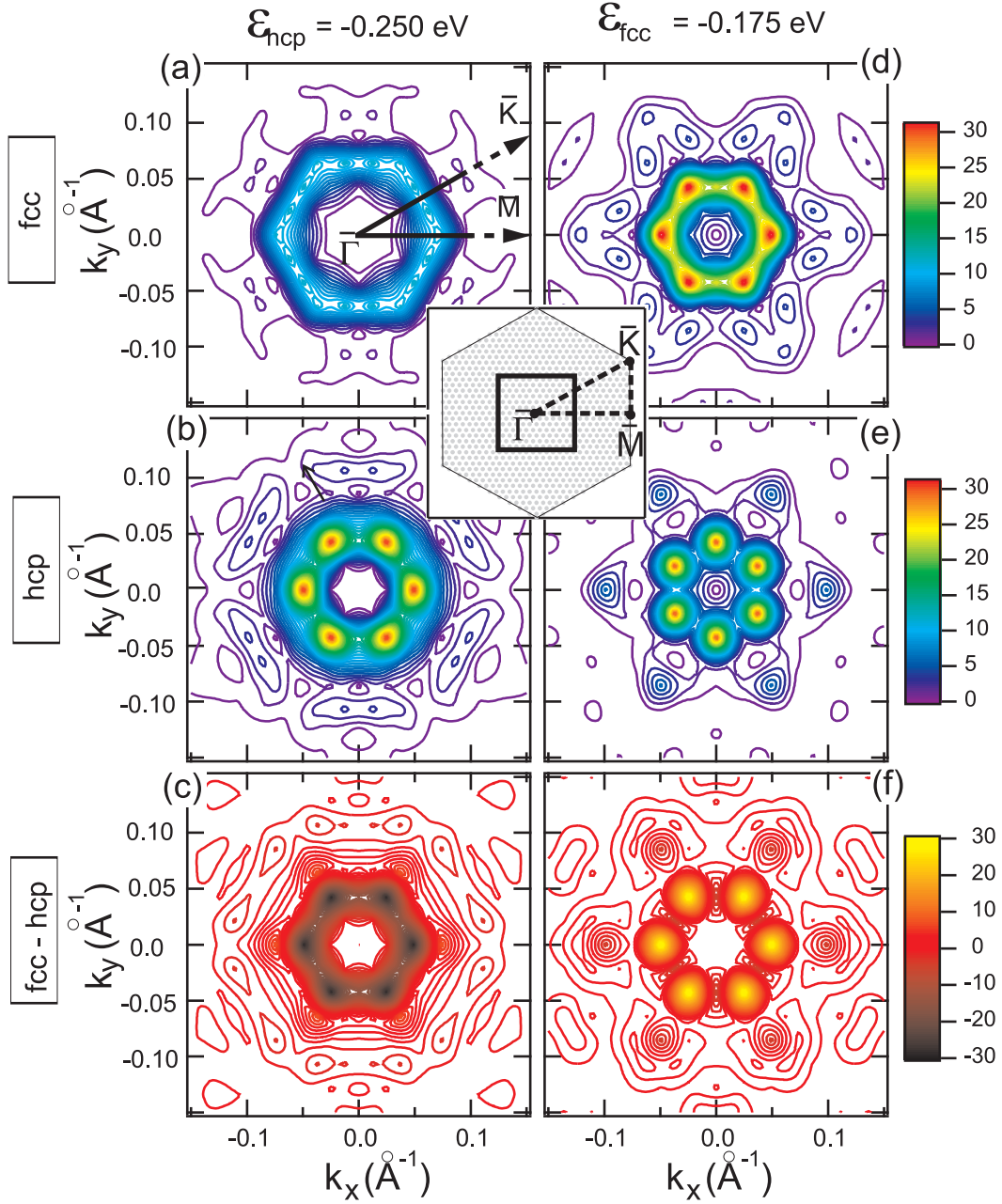


Figure 5.5: Decomposition of the vacuum DOS $n^{\downarrow}(\varepsilon, \mathbf{k}_{\parallel})$ in k -space for fcc (a),(d) and hcp (b),(e) stacking of 1 ML Co on Pt(111) at energies of peak positions and the difference of them (c),(f). A sketch of the BZ and of the plotted area is depicted in the inset by the black square. 817 \mathbf{k}_{\parallel} points in the full BZ have been used for these plots. A Gaussian broadening of the levels of 20 meV has been included.

the DOS comes from a hexagonal distribution of states in the BZ centered around the $\bar{\Gamma}$ point. The vacuum DOS $n^\downarrow(\varepsilon, \mathbf{k}_\parallel)$ has a similar shape in the two stackings, suggesting that it originates from the same band. Information about the \mathbf{k}_\parallel of the states which are affected by a change in the stacking can be inferred from the difference of the vacuum DOS for the two structures. As can be seen in Fig. 5.5(c) these states are located along the $\bar{\Gamma} - \bar{M}$ high-symmetry lines. Let us now focus on the fcc case only and analyze the vacuum DOS at different energies. A comparison of $n^\downarrow(\varepsilon_{\text{hcp}}, \mathbf{k}_\parallel)$ in (a) to $n^\downarrow(\varepsilon_{\text{fcc}}, \mathbf{k}_\parallel)$ in (d) reveals that for this stacking the \mathbf{k}_\parallel distribution of the vacuum DOS depends only weakly on energy. The width of the hexagonal distribution gets smaller as the energy increases, implying a negative effective mass for the involved band. For the hcp case a different trend is found. Interestingly, the DOS peaks for this stacking are located along the $\bar{\Gamma} - \bar{K}$ lines at ε_{fcc} (e), i.e. the hexagonal distribution appears rotated by 30° compared to what was found for ε_{hcp} (b). Nevertheless, the difference in the vacuum DOS for fcc and hcp at ε_{fcc} (Fig. 5.5(f)) reveals that the spectroscopic contrast originates mainly from states along the $\bar{\Gamma} - \bar{M}$ direction, similarly to what was found for ε_{hcp} .

The presented analysis of $n^\downarrow(\varepsilon, \mathbf{k}_\parallel)$ tells us that further information can be extracted from the band structure along the $\bar{\Gamma} - \bar{M}$ direction, shown in Figs. 5.4(b) and (c). The states which are marked in red are those with a high localization in the vacuum, thus giving the strongest contribution to the vacuum DOS. Based on the strong resemblance to the Co(0001) electronic structure, where a very similar band stretches from -0.3 eV to $+0.1$ eV, [92] we can assert that these states describe a Co surface resonance. Our analysis of the charge distribution reveals that the character of this band changes from the band maximum at $\bar{\Gamma}$, where it is predominantly of p character, to the band minimum, where it is of d character with a small contribution of s and p states. In contrast to Co(0001), in the case of 1ML Co/Pt(111) the surface resonance hybridizes with delocalized sp states which show a parabolic-like dispersion. As a result, gaps open in the surface resonance, which splits into several parts. Between -0.50 eV and $+0.2$ eV, the sp bands are slightly different for fcc and hcp stacking, due to the different coupling of the Co layer to the bulk Pt. This is clearly seen in the band structure, where the highly dispersive bands are located at different energies (e.g. compare the band energy at the $\bar{\Gamma}$ point). This results in a different interaction between the surface resonance and the substrate for fcc and hcp stackings. As a consequence, the energy at which the hybridization gaps open as well as the gap size and the surface resonance dispersion are different for the two cases. The influence of the stacking fault on the band energy can be seen also in the flat bands which can be attributed to Co d states from charge distribution analysis.

It is worth noticing that the modification in the electronic structure due to the stacking fault is not simply a rigid energy shift but is state-dependent and cannot be merely ascribed to a single state. The spectroscopic shift of 0.075 eV is an overall effect due to many states and this is also reflected by the large peak

width. The peak of the vacuum DOS is located at the energy corresponding to the highest band density for each stacking. If we focus on an energy interval, e.g. 0.10 eV, centered at the position of the main peak of the hcp spectrum (ε_{hcp}), we can observe that in the hcp case there are three bands contributing to the vacuum DOS, in contrast to the fcc case, where only one band is present. On the other hand, around ε_{fcc} we find more bands contributing to the fcc vacuum DOS than to the hcp one.

In summary, the spectroscopic shift of 0.075 eV is due to the different coupling of the Co layer to the Pt substrate for the fcc and hcp stacking, resulting in different hybridization of the Co surface resonance with Co-Pt *sp* states. The widespread assumption that the main peaks in scanning tunneling spectra are related to states at the $\bar{\Gamma}$ point, due to their weak decay in the vacuum, is not valid here. As demonstrated for the Co/Pt(111) system the electronic structure in the close vicinity of $\bar{\Gamma}$, but not exactly at $\bar{\Gamma}$, can be crucial for the spectral shape, depending on the character, dispersion and energy of the states. Only the analysis of $n^{\perp}(\varepsilon, \mathbf{k}_{\parallel})$ together with the band structure as described above allows us to unambiguously correlate specific spectroscopic features and electronic states.

5.3.3 Discussion

A comparison of the experimental and theoretical results reveals a good qualitative agreement. Both show a dominant feature in the negative bias regime with a comparable negative energy shift from fcc to hcp. The calculated peak positions are slightly closer to E_{F} . We ascribe this discrepancy to the reconstruction due to strain relief of the Co monolayer which is not included in the pseudomorphic slab assumed in the calculation. Thus, we can assign the dominant peak to a minority spin surface resonance below E_{F} . The calculations made it obvious that the different hybridization of this resonance with Co-Pt *sp* states is responsible for the observed differences in dI/dU at negative bias voltages. Such a stacking-dependent electronic contrast has been found for other Co systems like islands on Cu(111) and films on W(110) [81,88,91,92]. In contrast to our study these previous results were obtained on extended areas of different stacking in comparison to another extended area showing a different stacking. This is obviously different for the Co monolayer on Pt(111) where fcc-, bridge-, and hcp-sites alternate on a lateral scale of only a few atoms. Nevertheless, the electronic structure of these a few atoms wide areas is already well described by the infinite layer of the same stacking as shown by the calculations. This indicates that the position with respect to the underlying substrate, i.e. the stacking, is more important than the position of the neighboring Co atoms.

5.4 Structural and spin-resolved electronic properties of double-layer Co islands

Figure 5.6(a) shows the topography of 0.6 AL of Co deposited on the cold Pt(111) with subsequent annealing for 20 minutes. Compact free standing double-layer islands are observed together with double-layer wires attached to the Pt step edges. A comparison to the samples of Ref. [7] leads to the conclusion that the annealing temperature for both samples is similar, i.e. close to 340 K. The Co double-layer islands marked by the rectangle in (a) are shown at a closer view in Fig. 5.6(b). They exhibit a hexagonal superstructure, which is similar to the well-known Moiré pattern typical for the Co double-layer on Pt(111) [85,86]. It is caused by the large lattice mismatch of Co films on Pt(111) leading to strain relief via reconstruction. The bright spots labeled A in the inset can be identified as on-top positions. They are connected by fine bright lines forming a network of triangles. Two other distinct points B and C can be identified as centers of the two types of triangles pointing in opposite directions. A closer look to the superstructure reveals that the Moiré-like pattern is partly disturbed and actually more similar to a misfit structure observed before on annealed Co double-layer films [99]. According to Ref. [99] the Moiré pattern is indicative of an abrupt change of the lattice constants, i.e. a sharp interface, while the misfit structure is caused by a gradual change of the lattice constant due to intermixing of Co and Pt at the interface. Just as the Moiré pattern it is formed by hexagonal shaped areas showing different stacking. Since the size of a unit cell of such a misfit structure formed by completely alloyed films is larger than the original Moiré unit cell, the ratio of the sizes of the unit cells is a measure of the Co concentration in the upper layers. The inset of Fig. 5.6(b) reveals that the indicated unit cell size of the misfit structure is in good agreement with that of the Moiré pattern, i.e. 2.9 ± 0.1 nm. Therefore we can conclude that the present Co islands show some intermixing at the interface while the topmost layer consists mainly of Co. Intermixing and alloying processes are known to take place at temperatures above 340 K [100].

When increasing the annealing temperature after Co deposition the shape of the islands is changed significantly: Fig. 5.6(c) shows a sample of 0.5 AL Co deposited on the cold Pt(111) with subsequent annealing to a temperature which is approximately 50 K higher than for the sample shown in Fig. 5.6(a), i.e. approximately 390 K. The resulting Co double-layer islands show a similar size and density. The two islands marked by the white rectangle in Fig. 5.6(c) are shown at a closer view in Fig. 5.6(d). In comparison to Fig. 5.6(b), where the Co double-layer islands show mainly a step from the top-layer directly onto the Pt(111) surface, the Co islands shown in Fig. 5.6(d) are surrounded by a dendritic monolayer rim. Considering the shape and the growth direction the rim reminds one of the Co induced dendrites on Pt(111) obtained by depositing Co at 400 K [95]. It was

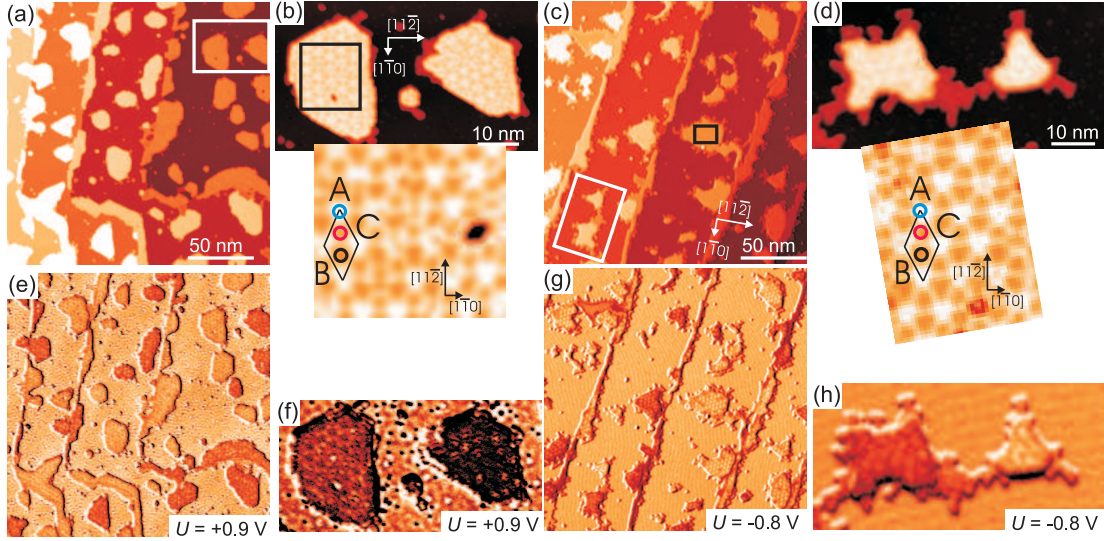


Figure 5.6: Co double-layer islands prepared by Co deposition onto the pre-cooled Pt(111) surface with subsequent annealing. Upper panels: Topographic images of compact (a), (b) and fringy (c), (d) islands; Insets: Magnified view of island reconstruction with unit cell. Lower panels: dI/dU maps measured simultaneously to the topographic images of the upper panels with out-of-plane sensitive magnetic tips ($U_{\text{mod}} = 20$ mV, (e), (f): Cr-coated, $I = 2.0$ nA; (g), (h): Fe-coated, $I = 1.0$ nA).

found that these dendrites consist mainly of Pt. Even though the perimeter of the islands is very different the interior of the Co double-layer shown in (a) and (c) is comparable. Both the compact islands (a), (b) and the fringy ones (c), (d) exhibit the same hexagonal superstructure with the characteristic points A, B and C as indicated in the magnified views.

In order to reveal the magnetic state of the compact Co double-layer islands of Fig. 5.6(a) the simultaneously acquired out-of-plane sensitive magnetic dI/dU map is shown in Fig. 5.6(e). Again we observe a relatively homogeneous electronic structure for the Pt(111) surface and a two-stage contrast for the Co double-layer islands. This shows that the compact Co islands are ferromagnetic with an out-of-plane anisotropy and thus are magnetized either up or down with respect to the surface plane, in accordance with the observations reported in the literature [7,84]. In contrast to the work of Rusponi *et al.* [84], no significant variation in height due to the spin-valve-effect of the tunnel junction was observed. The dI/dU map in Fig. 5.6(f) shows that the two compact islands of (b) are magnetized in opposite directions. In addition to the magnetic signal they show variations of the electronic structure which correlate to the topographic reconstruction. The features in the dI/dU signal of the Pt(111) surface reflect standing electron waves, induced by scattering of the surface state, which are observed on Pt(111) above

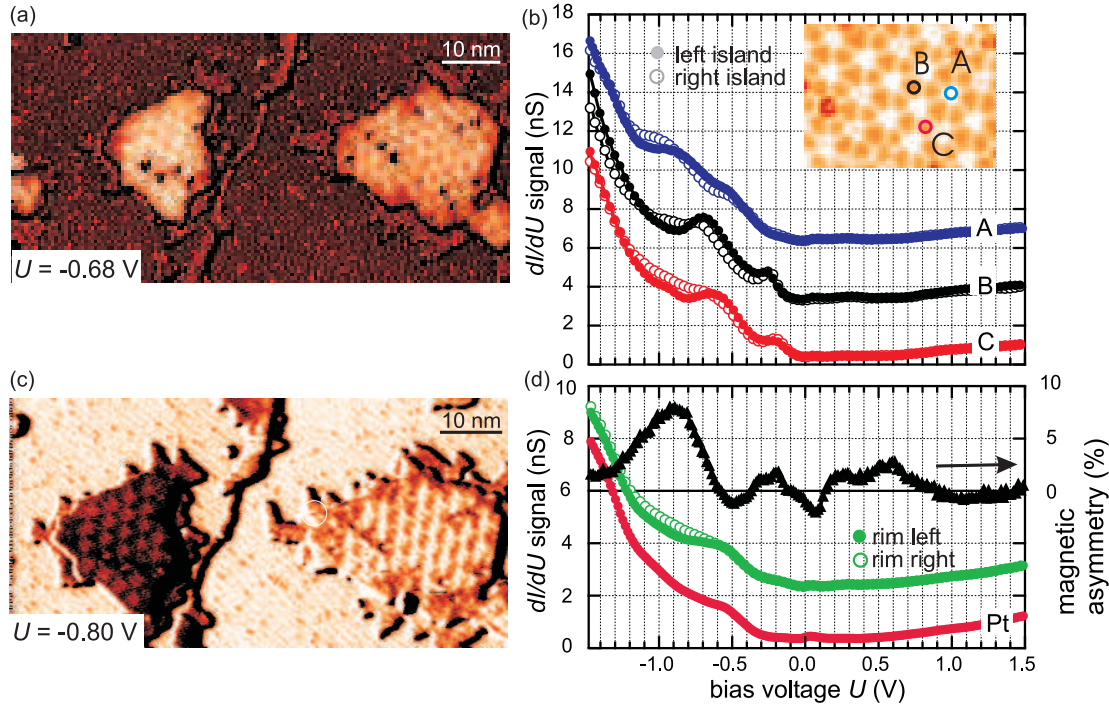


Figure 5.7: (a) Spin-resolved dI/dU slice of STS field. (b) dI/dU spectra on characteristic points of the superstructure pattern (see inset) on the left (filled dots) and the right (open dots) Co double-layer island obtained from the spin-resolved STS field. The Co spectra are shifted by multiples of 3 nS. (c) dI/dU map: the rims of the two islands show different signal intensity. (d) dI/dU spectra on the rim of the left (filled dots) and the right (open dots) Co island and their magnetic asymmetry. The rim spectra are shifted by 2 nS with respect to the Pt spectrum. (Fe-coated tip, $I_{\text{stab}} = 1.5$ nA, $U_{\text{stab}} = +1.5$ V, $U_{\text{mod}} = 20$ mV.)

+0.5 eV as outlined in Chap.4. An out-of-plane sensitive magnetic dI/dU map of the fringy Co islands of Fig. 5.6(c) is shown in Fig. 5.6(g). Also these fringy Co double-layer islands show a two-stage contrast and we therefore conclude that the magnetic structure is equivalent to that of the well-studied compact double-layer islands shown in (e), i.e. they are ferromagnetic with an uniaxial anisotropy normal to the surface. Again, no significant effect of the magnetization direction of the islands on the topographic signal was observed. Figure 5.6(h) shows the dI/dU map measured simultaneously to the topography of (d) and reveals the magnetic orientation.

To investigate the energy-dependent spin-polarization of the double-layer Co islands in more detail a spin-resolved STS field was measured for the two oppositely magnetized islands in the center of Fig. 5.6(g). Fig. 5.7(a) shows a slice of

the STS field at -0.68 eV with magnetic contrast and reveals the influence of the reconstruction on the spin-resolved electronic structure. The dI/dU spectra obtained on characteristic points of the Co double-layer are plotted in Fig. 5.7(b). The topography in the inset indicates the non-equivalent points A, B and C of the misfit structure which are observed both on the compact and the fringing double-layer islands. The spectra with the filled and the open data points are measured on the left and the right island of Fig. 5.7(a), respectively, which are magnetized in opposite directions. All spectra in Fig. 5.7(b) are rather featureless in the positive bias regime but show a two peak structure below E_F . While for the same characteristic point of the misfit structure the peak energies of the left and the right island are the same, the intensity varies slightly as a result of the different magnetic state of the island. For the different points A, B and C the energies of the two peaks are shifted with respect to each other. Overall the structure of the Co-double layer is too complicated to assign the peaks to specific atom arrangements or even electronic states. On the basis of our measurement of the spin- and energy-resolved electronic structure we cannot identify a state that may explain the astonishing difference in the apparent height of Co islands of opposite magnetization as observed in the case reported in the work of Rusponi *et al.* [84].

Interestingly, an analysis of the fringing Co double-layer islands reveals a magnetization direction dependent dI/dU signal also for the monolayer rim surrounding the Co double-layer islands which can be seen in the spin-resolved dI/dU map of Fig. 5.7(c). It is observed that the spin-polarization of the rim is of the same sign as that of the corresponding double-layer island which leads to the conclusion that there is a ferromagnetic coupling. The energy-dependent dI/dU signal at the rims of the two oppositely magnetized islands as well as on the bare Pt is shown in Fig. 5.7(d). The dendritic shape of the rim and its spectroscopic similarity to the bare Pt suggests that the rim consists mainly of Pt. Due to the observation of an overall magnetic moment of the rim in contrast to the bare Pt we conclude that the spin-polarization originates from Co incorporated in or underneath the rim. The magnetic asymmetry between the rim of the left and the right island is also plotted in Fig. 5.7(d). It shows the largest values in the negative voltage regime, just as for the other Co related features. The spin-polarization of the rims is either due to the direct vicinity of the rim to the ferromagnetic Co double-layer island or by the formation of a ferromagnetic CoPt-alloy.

5.5 Magnetism of Co nanostructures

In order to study the magnetic properties of the Co monolayer as well as the Co double-layer nanostructures and to verify the magnetic origin of the observed contrasts in dI/dU maps we probed the Co structures in variable magnetic fields, which were applied along the surface normal.

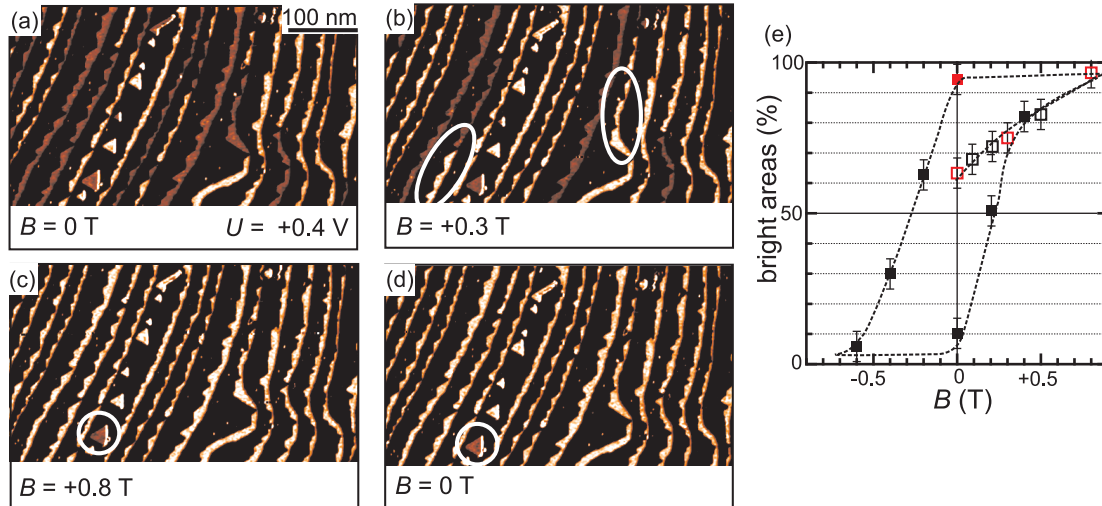


Figure 5.8: (a)–(d) Selection of dI/dU maps of Co monolayer wires and islands in the presence of an external magnetic field applied perpendicular to the surface plane measured with an out-of-plane sensitive magnetic Cr-coated tip. The bright or dark appearance of the Co corresponds to a parallel or antiparallel alignment of the tip and sample magnetization. (e) Hysteresis loop obtained by plotting the percentage of bright domains at certain magnetic fields. The open squares belong to the initial magnetization curve and the red color indicates the dI/dU maps shown. The dashed line is a guide to the eye. ($I = 0.7$ nA, $U_{\text{mod}} = 20$ mV)

5.5.1 Co monolayer nanostructures

Figures 5.8(a)–(d) show selected out-of-plane sensitive magnetic dI/dU maps with an applied external magnetic field B as indicated. The sample preparation, which has been described in Sec. 5.2, results in some free standing Co islands and Co wires which are attached to the Pt step edges. While the Pt substrate has a uniform dI/dU signal with low intensity, a two stage magnetic contrast of the oppositely out-of-plane magnetized Co is clearly visible for the islands as well as the wires. Figure 5.8(a) displays the magnetic virgin state of the sample at 0 T and the amount of both opposite magnetization directions of the Co structures is approximately equal. After increasing the magnetic field to +0.3 T (b), some Co areas which are marked in the dI/dU map changed their magnetic orientation. From this contrast reversal we can directly conclude, that these bright areas are now aligned with the direction of the external field. For the left marked wire in (b), it can be observed that the field-induced reorientation process does not change the magnetization of the wire completely but a domain wall is trapped at

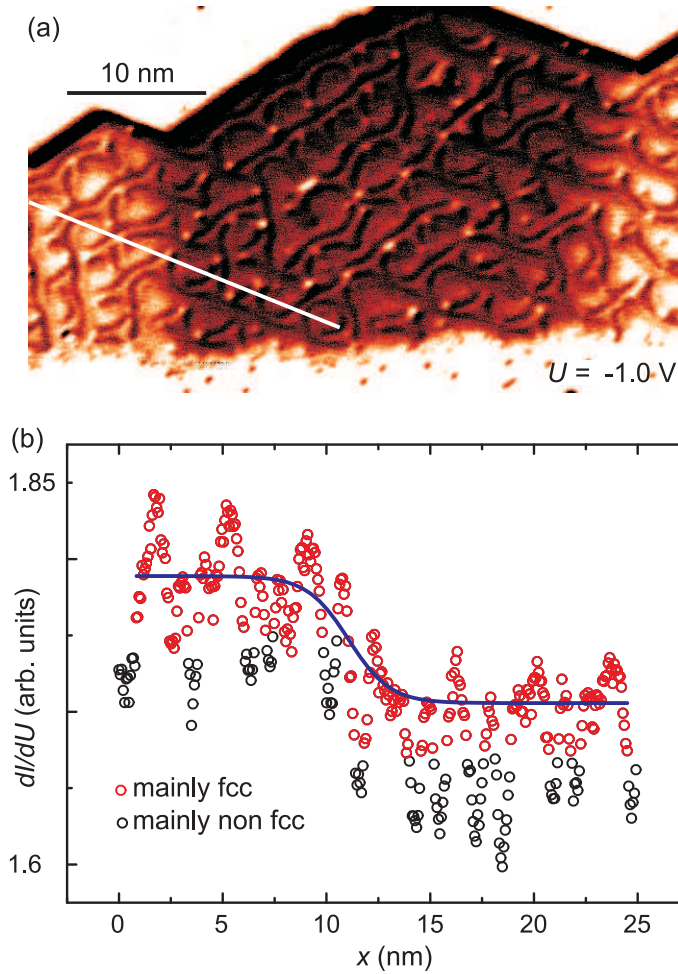


Figure 5.9: (a) dI/dU map of a Co monolayer wire with three domains measured with an out-of-plane sensitive magnetic Cr-coated tip. (b) Domain wall profile (open circles) along the line marked in (a). The solid line gives a fit to the red data points. ($I = 1.5$ nA, $U_{\text{mod}} = 20$ mV)

a constriction. At a magnetic field of $+0.8$ T all Co structures appear bright except one comparably large Co island marked in Fig. 5.8(c). Figure 5.8(d) displays the magnetic state at remanence. A direct comparison to the previous dI/dU map in (c) shows that all wires and islands remain in their magnetic state.

Analyzing the magnetic state of the Co nanostructures and plotting the percentage of the bright Co areas at several applied magnetic fields leads to a hysteresis curve, which is displayed in Fig. 5.8(e). Since the external magnetic field is applied along the easy anisotropy axis, the hysteresis curve shows a typical ferromagnetic shape with a very high remaining magnetization after field removal. The extracted coercivity of this area of the monolayer Co sample is $\mu_0 H_c = 0.25 \pm 0.05$ T. This

value is comparable to the coercivity observed for spatially averaging experiments on few atom wide Co wires on Pt(111) at low temperatures [9]. As visible in (e) the obtained hysteresis curve does not show a simple square loop shape but is slightly canted. This can be understood by taking into account that the magnetic reorientation process occurs not at the same magnetic field for each Co structure, but progresses successively [101]. In general we observe that larger islands as well as wider wires seem to switch abruptly from one saturated state to the opposite one at higher applied magnetic fields than smaller Co structures. Furthermore, the reorientation process itself is different for wires and islands. While the Co islands are always in a single domain state, wires with a sufficient width are reoriented by domain wall movement.

The existence of domain walls in wires allows the critical examination of recent results obtained on nanoscale Co monolayer islands. Namely, Rusponi *et al.* [7] interpreted their MOKE and STM measurements in terms of strongly coordination-dependent magnetic anisotropies: while—according to Ref. [7]—Co atoms at the island perimeter exhibit a very high out-of-plane anisotropy of 0.9 ± 0.1 meV per atom a weak in-plane anisotropy ($E_A = -0.03 \pm 0.01$ meV per atom) is found for surface atoms within the islands. Such magnetic properties have two significant consequences on the nanoscale domain structure of sufficiently large islands and wires: first, the easy axis shall rotate from out-of-plane to in-plane if the lateral dimensions exceed the magnetic correlation or exchange length. Second, the strongly enhanced anisotropy at Co step edges should lead to very narrow domain walls. While we cannot scrutinize the latter hypothesis due to the complex structural and electronic properties of the Co monolayer dislocation network on Pt(111) (cf. Fig. 5.1), we were able to investigate whether the easy axis of magnetization changes with increasing distance from the Co step edge by analyzing domain walls in Co nanowires. As shown in Fig. 5.8 domain walls are preferentially located at constrictions which are a few nanometers wide only, if the terraces are particularly narrow. Therefore, we have studied Co nanowires which were grown on much wider Pt(111) terraces and exhibit a width of 15–25 nm as shown in the dI/dU map of Fig. 5.9(a). In the central part of the image a dark domain can be recognized which is surrounded by two bright domains. Both domain walls separating the three domains are located in constrictions and are about 20 nm long. Since these data were measured with an out-of-plane sensitive probe tip we can conclude that the Co nanowire is perpendicularly magnetized even 20 nm away from the Co step edge. But in which way is this distance related to the magnetic exchange length? This can be analyzed by a closer inspection of the domain wall profile. For this purpose we have taken a profile of the dI/dU signal along the white line in Fig. 5.9(a). The result is plotted in Fig. 5.9(b). In order to minimize the influence of the inhomogeneous spin-averaged electronic structure due to different stacking (see Sec. 5.3) we have not taken the line section perpendicular to the domain wall but under an angle of 60° . Thereby, mostly fcc sites

are crossed and hcp sites are avoided as far as possible. The line section shows two levels of dI/dU signal strength on the left and the right side which represent the oppositely magnetized domains and the transition area in between. While the data points on each domain still scatter due to the remaining stacking influence, the signal becomes much smoother when neglecting the data points originating from the hcp lines which are given in black color. The remaining red data points are fitted with a standard domain wall function [26]

$$y = y_0 + y_{\text{sp}} \tanh \left(\frac{2(x - x_0)}{w} \right) \quad (5.3)$$

which is based on continuum micro-magnetic theory [102]. y_0 and y_{sp} are the spin-averaged and the spin-polarized part of the dI/dU signal, x_0 is the position of the domain wall center, and w represents the domain wall width, which is determined by the exchange stiffness A and the effective anisotropy constant K_{eff} by

$$w = 2\sqrt{\frac{A}{K_{\text{eff}}}}. \quad (5.4)$$

As shown by a solid line in Fig. 5.9(b) the best fit is obtained for a domain wall width of approximately 4 nm, i.e., much narrower than the structural width of the Co nanowire. This observation indicates that the intrinsic anisotropy of surface coordinated Co atoms on Pt(111) is not in-plane as proposed by Rusponi *et al.* [7] but out-of-plane instead. This conclusion is also consistent with our observation that the magnetization of triangular Co monolayer islands is homogeneous across the islands' surfaces even though the base length of some islands is about thirty times larger than the exchange length $L = w/2$ extracted from Fig. 5.9(b). In order to obtain an appropriate value of the exchange stiffness of the ML A_{ML} has been calculated in two ways. Together with the information that 0.8 ML Co/Pt(111) is still ferromagnetic above RT (Ref. [96]) and the assumption $T_C \propto A$ we obtain $A_{\text{ML}} = 7.0 \cdot 10^{-12}$ J/m with $T_{C,\text{bulk}} \approx 1400$ K and $A_{\text{bulk}} = 3.0 \cdot 10^{-11}$ J/m. A second way to obtain A_{ML} is using $n_c \propto A$ where n_c is the number of coordination of an atom. Since n_c is reduced from twelve for bulk atoms to six for a monolayer atom, A_{ML} is given by $1.5 \cdot 10^{-11}$ J/m. Since the correct values for A_{ML} is unknown, both roughly estimated values might be the lower and the upper limit for a reasonable value range. Using these reasonable value for A , the anisotropy constant results in $+0.08 \text{ meV/atom} \leq K_{\text{eff}} \leq +0.17 \text{ meV/atom}$.

5.5.2 Co double-layer nanostructures

Figures 5.10(a)–(f) display out-of-plane sensitive magnetic dI/dU maps of compact Co double-layer islands measured at different magnetic fields.

Figure 5.10(a) reveals the magnetic virgin state of the compact islands and both magnetic orientations are distributed equally. The application of a magnetic

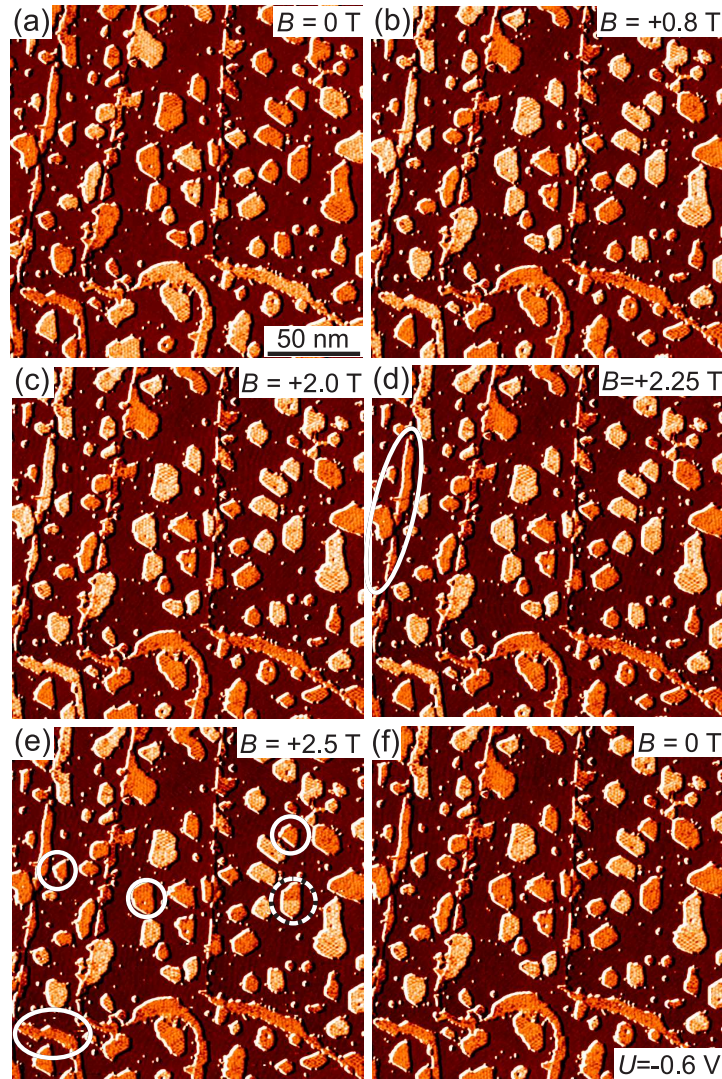


Figure 5.10: (a)–(f) Selection of dI/dU maps of compact Co double-layer islands as shown in Fig. 5.6(a) in the presence of an external magnetic field applied along the surface normal. Between (a) and (b) a field-induced change of the tip magnetization occurs. ($I = 2.0$ nA, $U_{\text{mod}} = 20$ mV)

field of +0.8 T (Fig. 5.10(b)) causes a complete inversion of the magnetic contrast, which can be explained by an alignment of the tip magnetization with the external magnetic field. Although we used a Cr-coated tip for this specific measurement it is possible that small Co/Pt clusters are attached to the tip due to pulsing in order to sharpen the tip. This has also been observed for Fe clusters on a W tip (see Chap. 3). These clusters might cause a residual magnetic moment, which can be aligned in an external magnetic field. A response of the sample

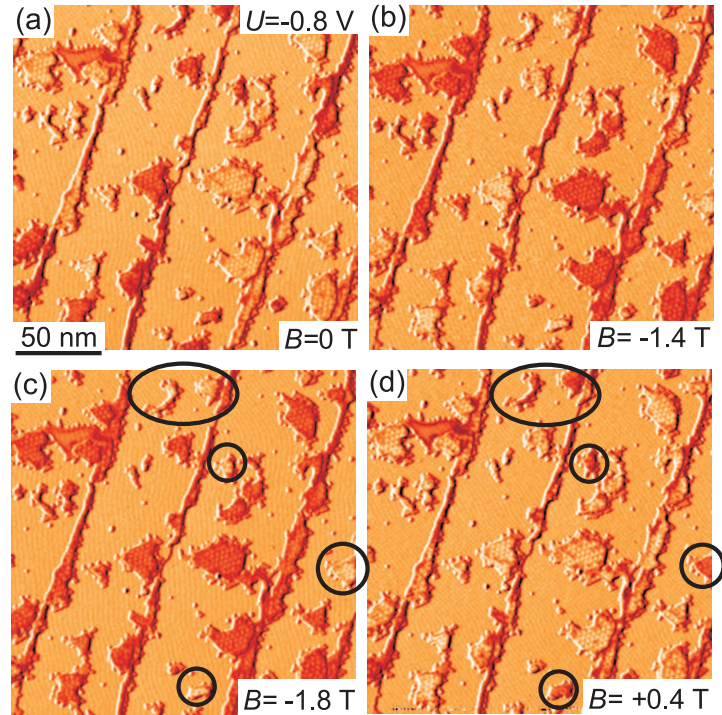


Figure 5.11: (a)–(d) Selection of out-of-plane sensitive magnetic dI/dU maps of fringy Co double-layer islands as shown in Fig. 5.6(e) in the presence of an external magnetic field applied along the surface normal. Between (a) and (b) a field-induced change of the tip magnetization occurs which causes an inversion of the magnetic contrast. ($I = 1.0$ nA, $U_{\text{mod}} = 20$ mV)

magnetization to the external field is not observed. A further increase to $+2.0$ T in (c) does still not reveal any switching of the Co double-layer magnetization. At an applied field of $+2.25$ T in (d) the magnetization of some structures is rotated as indicated. The switched structures are directly attached to the Pt step edge. At a field of $+2.5$ T in (e) a few free standing Co islands switched which are marked by circles. This is the maximum available external field which surprisingly is not sufficient to align the magnetization of all islands. While every island shows a uniform magnetization, i.e. in a single domain state, on top of one island marked in (e) both opposite magnetization directions are visible. This is caused by a magnetization reversal in between two subsequent lines of the image due to a residual stray field of the tip. After the removal of the external field (f), a comparison to (e) reveals that all Co islands remained in their previous magnetic state. Therefore also the compact Co double-layer islands on Pt(111) show 100% remanence. Since the first influence of the external magnetic field on the sample

was detected between +2.0 T and +2.25 T we can conclude that $\mu_0 H_c > 2.0$ T.

Figures 5.11(a)–(d) show a selection of out-of-plane sensitive magnetic dI/dU maps of the fringy Co double-layer islands measured in the presence of an external magnetic field. Figure 5.11(a) shows the virgin state of the sample. When applying -1.4 T in (b) the magnetization direction of the tip is inverted but no change in the island magnetization is observed. In contrast to the dI/dU maps shown in Figure 5.10 this behavior has been expected since an Fe-coated tip has been used. At a field of -1.8 T shown in (c) nearly all fringy double-layer islands switched except the indicated ones. Changing the field now to $+0.4$ T in (d) shows that this field is sufficient to align the tip magnetization again but is too small to rotate the magnetization of any monodomain Co double-layer island. This shows again the complete remanence. According to these observations we can conclude a value of $1.4 \text{ T} < \mu_0 H_c < 1.8 \text{ T}$ for the coercivity of the fringy islands.

The results obtained for the different kinds of Co double-layer islands suggest a high out-of-plane anisotropy of these nanostructures. The surprisingly high coercivities of $\mu_0 H_c > 2.0$ T for the compact islands are to our knowledge higher than all previously reported coercivities for Co structures on Pt(111). While it is already known that Co double-layers islands on Cu(111) [81] exhibit a very high coercivity between 1.0 T–1.5 T, the values of the compact Co double-layer islands studied in this work are even higher. This again emphasizes the important role the substrate plays for the magnetic properties of nanoscale structures.

Interestingly, the fringy islands show a much lower coercivity. It is hard to answer which of the following hypotheses explain this observation. In Sec. 5.4 it has already been pointed out that the higher preparation temperature of the fringy islands not only causes the formation of the surrounding rim but probably also leads to a higher amount of Pt incorporated into the islands. In Ref. [7] the extraordinary importance of the perimeter atoms of Co islands for the total anisotropy due to their reduced coordination was shown. Since the number of the perimeter Co atoms for the fringy islands is reduced (surrounded by Pt in the rim) in comparison to the more compact islands, this might also cause a decrease of the strength of the anisotropy and a smaller coercivity. Finally, the magnetization reversal process might also start at the rim because the nucleation of the opposite domain might be much easier there.

5.6 Summary

We have presented a detailed study of the structural, electronic, and magnetic properties of monolayer and double-layer Co islands and wires on Pt(111). Although the Co monolayer is electronically highly heterogeneous due to a lattice mismatch induced dislocation network, it is possible to observe the out-of-plane magnetized domains by spin-resolved STS. Independent of the magnetization di-

rection the spin-resolved spectra exhibit a dominant peak at about -0.28 eV for fcc, which is shifted downwards by more than 0.12 eV for hcp- and bridge-site stacked regions, which are only several atoms wide. Accordingly the peaks in the magnetic asymmetry in this energy range are also shifted downwards on the hcp- and bridge-site regions relative to the fcc regions.

In order to understand the spectroscopic stacking dependency, first-principles calculations for pseudomorphic Co monolayers on Pt(111) in fcc- and hcp-stacking were performed. A detailed analysis revealed that the dominant peak originates from a d -like Co surface resonance of minority-spin character which is similar to the state found for thicker Co(0001) films on different substrates [92]. The spectroscopic shift between differently stacked areas results from different hybridization of the Co surface resonance with Co-Pt sp states. Even though the calculation was done for infinite areas of a given stacking it reproduces the experimental observations fairly well although the same stacking is only present for a few atoms.

Two types of Co double-layer islands are observed depending on the preparation: compact islands for a lower annealing temperature and fringy islands with a monolayer high rim for higher annealing temperature. Both of them show an out-of-plane anisotropy and exhibit a misfit structure. The reconstruction indicates intermixing between Co and Pt at the interface. Spin-resolved spectroscopy reveals that the non-equivalent stackings of the misfit structure exhibit also distinct energy-dependent differences due to shifting peaks below the Fermi energy. In addition it was found that the monolayer high rim, which surrounds the fringy islands consists of Co as well as Pt atoms, shows a spin-polarization in the negative voltage range and couples ferromagnetically to the corresponding island.

We find an out-of-plane magnetization of all probed Co nanostructures. By measuring the domain wall width on monolayer wires, the magnetic exchange length is determined to be less than 2 nm. According to Ref. [7] the magnetic anisotropy of the surface atoms within the islands is weakly in-plane and only the perimeter atoms exhibit a large out-of-plane anisotropy. We have no experimental indications to support this: islands with a base length as large as thirty times the exchange length still show a homogeneous out-of-plane magnetization. In order to reproduce the measured domain wall width we propose an out-of-plane anisotropy of $+0.08 \text{ meV/atom} \leq K_{\text{eff}} \leq +0.17 \text{ meV/atom}$ for atoms within the island.

Finally, our measurements in the presence of an external magnetic field show that the coercivity of Co nanostructures is highly increased by a change of sample morphology. While a Co monolayer system exhibited a coercivity of $\mu_0 H_c = 0.25 \pm 0.05$ T, for the compact Co double-layer nanostructures we observed a surprisingly high coercivity of $\mu_0 H_c > 2.0$ T. The fringy Co double-layer islands exhibit a coercivity between 1.4 T– 1.8 T.

6 Single Co atoms on Pt(111)

The following chapter reports on the scanning tunneling microscopy and spectroscopy measurements on single Co atoms on Pt(111). It will be shown that the electronic properties of the Co atoms depend on the adsorption site similar to what was found for the Co monolayer islands and wires in Chap. 5.

This chapter is organized as follows: Sec. 6.1 gives an overview of previous STS-results concerning the properties of single atoms on various surfaces. The magnetic properties of single Co atoms on Pt(111) obtained by spatially averaging techniques and the consequences for STS measurements on single Co atoms are also discussed. After describing the sample preparation in Sec. 6.2 the spectroscopic properties of the single Co atoms are shown in Sec. 6.3. The Secs. 6.4 and 6.5 show how Co atoms are manipulated laterally and describe the observation of height changes of atoms, probably due to the formation of Co-H complexes. The last Sec. 6.6 summarizes the results.

All measurements were performed in the low temperature UHV system described in Chap. 3 at temperatures around 0.3 K and 4.2 K.

6.1 Introduction

The technical progress regarding miniaturization of magnetic storage units requires a detailed and comprehensive knowledge of the physical properties of structures on the nanoscale. In order to obtain this knowledge one way starts with the attempt to understand the smallest magnetic units, which consist of a few atoms or even a single atom and are bounded to the surface of a non-magnetic substrate. A perfect tool to probe these structures is the low temperature STM.

Up to now there are basically three approaches which have been applied to study the magnetic properties of single magnetic atoms or magnetic multimers on nonmagnetic surfaces by STS. The first approach uses the spin-flip scattering of substrate electrons on the uncompensated spins of the magnetic adatoms on or inside a nonmagnetic metal crystal, namely the Kondo-effect [103]. The Kondo-effect becomes visible in STS experiments because of the formation of a many electron state. This leads to the so-called Kondo resonance, a sharp zero bias voltage spectroscopic feature, which is localized on top of the adatoms. The width of the resonance scales with $k_B T_K$ where T_K is the so-called Kondo temperature. The first observation of the Kondo resonance succeeded on Ce and Co adatoms

on Ag(111) and Au(111) surfaces, respectively [104,105]. So far the Kondo-effect has been studied for several adatoms on nonmagnetic substrates like Ti and Co on Au(100) [106,107], Co on Au(111), Cu(111), and Ag(111) [108–110] and Ti and Ni on Au(111) [111]. The Kondo temperature for all these systems is several tens of a K. For other material combinations like Fe on Pt(111) [71] or V, Cr, Mn, and Fe on Au(111) [111] STS experiments showed no indications for a Kondo resonance, probably because T_K is much lower than the experimental temperature of about 6 K. Another possible reason might be a larger magnetocrystalline anisotropy energy E_A which should destroy the Kondo-effect, if $E_A \gg k_B T_K$. The appearance or absence of a Kondo resonance on dimers or trimers has been used to provide information about their internal magnetic coupling [112]. This is somewhat hampered by the fact, that the ferromagnetic coupling of two adatoms can also decrease the Kondo temperature due to a decrease of the exchange interaction between the substrate conduction electrons and the dimer [108].

Therefore, a second approach uses the interpretation of spin-split, unoccupied single-electron resonances of magnetic dimers on a NiAl(110) surface. Together with DFT calculations new insights into the ferromagnetic or anti-ferromagnetic coupling of the dimers were obtained [113].

A third and more recent approach to learn more about the magnetic properties of single atoms and multimers uses the method of inelastic electron tunneling spectroscopy (IETS) [114] to excite the internal spin-degrees of freedom. This method has been applied so far on single Mn adatoms [115] and engineered atomic structures [116] deposited on a thin insulating wetting layer. It was possible to show basic magnetic excitations like spin flip processes and to measure the total spin of the chains as well as the exchange coupling as a function of size.

All these previous approaches have been performed using non-magnetic tips and thus did not detect the spin of the involved electrons directly. By applying spin resolved STM it could be possible to measure directly the spin-polarization of the electronic states of the adsorbates as well as their influence on the surrounding substrate. So far this method has shown its great abilities not only by probing oppositely magnetized, nanoscale stripes, films, or islands but also by revealing antiferromagnetic and frustrated coupling with atomic resolution on antiferromagnetic films [26, 41, 117–119]. Regarding single adsorbates, the differences in spin-polarized electron scattering at single oxygen adsorbates on oppositely magnetized Fe films were found by spin resolved STM [120]. But up to now, there are no results on single magnetic adsorbates on non-magnetic surfaces.

Since spin-resolved STS measurements require a magnetic moment of the adatoms which is stable within a reasonable time scale, all Kondo systems are disqualified due to their low magnetocrystalline anisotropy. A promising system for experiments on magnetic atoms with a stable magnetic moment deposited on non-magnetic substrates is the Co/Pt(111) system as will be shown in the following.

Magnetic properties of single Co atoms on Pt(111)

Gambardella *et al.* [8] showed by the spatially averaging XMCD technique that Co chains attached to Pt step edges evolve a long-range ferromagnetic state below 15 K and an increased anisotropy energy of 2.0 meV per atom compared to the Co bulk systems with 0.04 meV per atom.¹ For single Co atoms on Pt(111) their experiments revealed a giant uniaxial magnetic anisotropy energy of $E_A = 9$ meV/atom where the easy axis points perpendicular to the surface plane [4]. This value is obtained by the extracted magnetization from XMCD spectra with respect to the external magnetic field for an ensemble of single Co atoms. The magnetization curves show a paramagnetic shape at a measurement temperature of 5.0 ± 0.5 K. This fact has to be related to the total recording time of the magnetization curve of about 1000 s.² According to Gambardella *et al.* [4] the large magnetic anisotropy energy of the single Co atoms is mainly established by (1) the 3d-electron localization, which is induced by the reduced coordination, and (2) by the strong spin-orbit coupling of the Pt 5d-states. The first increases the spin-orbit energy due to an increase in the LDOS at the Fermi energy, while the latter results in additional magnetic anisotropy energy of the induced magnetization. In addition the experiment revealed that the anisotropy energy per atom decreases for Co particles with an increasing number of atoms (up to five) while the magnetic orientation prefers to be orientated perpendicular to the substrate.

The anisotropy energy E_A allows to calculate the total magnetic energy E of a single Co atom as a function of θ where θ denotes the angle between the easy axis and the magnetic moment. In the presence of a magnetic field B , which is applied in the easy axis, the magnetic energy is given by

$$E(\theta, B) = E_A \cdot \sin^2 \theta - \mu B \cos \theta. \quad (6.1)$$

where μ denotes the total magnetic moment of the single Co atom. E is a sum of the anisotropy energy and the Zeeman energy, which depends on B . Figure 6.1(a) displays E for three different magnetic fields. At zero magnetic field two equivalent minima at $\theta = 0$ and at $\theta = \pi$ can be found representing magnetic *up* and *down* states. Both states are separated by the energy barrier of E_A . When a magnetic field is applied the energy of the magnetic *up* and *down* states differs by ΔE and therefore the magnetic state parallel to B is preferred.

The required temperatures, which allow the measurements of stable magnetic moments of the single atoms, can be estimated in a first approximation by the so-called Néel-Brown model [121, 122]. In this model a single domain particle is either in one of the magnetic *up* or *down* state as shown in Fig. 6.1(a). The energy barrier can only be overcome by thermal activation. In the absence of a magnetic

¹XMCD is an acronym for X-Ray Magnetic Circular Dichroism

²Jan Honolka, private communication.

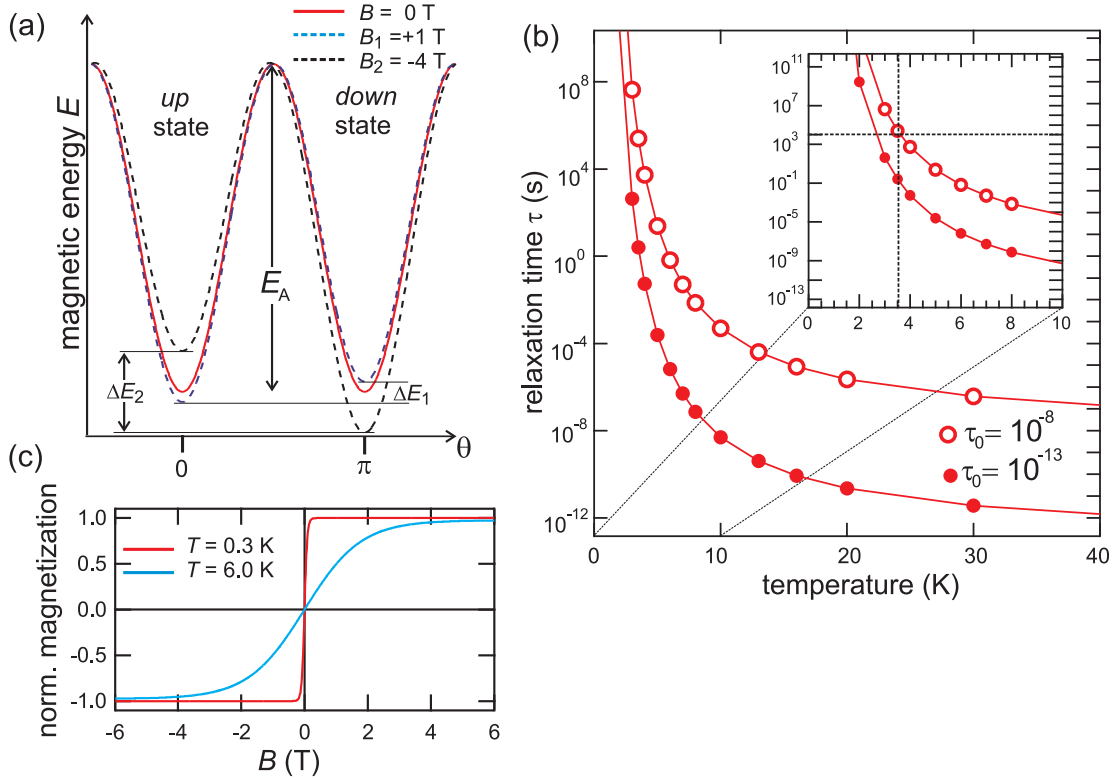


Figure 6.1: (a) Magnetic energy of the single Co atom with respect to θ which denotes the angle between the easy axis and the magnetic moment of the atom. At zero magnetic field two equivalent minima at $\theta = 0$ and at $\theta = \pi$ represent magnetic *up* and *down* states. If a magnetic field B is applied parallel to the easy axis, both energy minima are not equivalent anymore due to the Zeeman energy shift ΔE . (b) Temperature dependence of the switching rate according to Eqn. 6.2 with $E_A = 9$ meV in the absence of B . (c) Calculated magnetization curve of an ensemble of Co atoms at 0.3 K and at 6.0 K with respect to B .

field the relaxation time of the single atom magnetization, which is equal to the inverse switching rate, is expressed by

$$\tau = \tau_0 \times e^{\frac{E_A}{k_B T}} \quad (6.2)$$

with the attempt frequency $1/\tau_0$, the energy barrier E_A , and the temperature T . Even though τ_0 depends on several parameters, for simplicity it is often supposed to be constant [123]. Assuming a range of reasonable values for τ_0 , Fig. 6.1(b) shows the temperature dependence of τ for $\tau_0 = 10^{-8}$ s and $\tau_0 = 10^{-13}$ s. A mean value of $\tau_0 = 10^{-9}$ s is often used to describe thermally activated processes [93,

123]. We observe that the relaxation time becomes very large for the two given values, comparable to the life time of the universe, when the temperature is low enough. The inset of Fig. 6.1(b) displays a magnified view to the temperature dependence below 10 K. In order to perform detailed spatially- and spin-resolved STS studies on several Co atoms and their surrounding at least 3 h are required within the magnetic moment of the Co atoms should be stable. Consequently, the required temperature for Co/Pt(111) system is well below 4 K. This reveals that STM facilities operating below 1 K are particular suitable and needed for these experiments.

This conclusion is valid only if the relaxation process is purely thermally activated and no other processes contribute to the magnetization reversal. One process, which might play an important role, is the so-called quantum tunneling process of the magnetization (QTM). In analogy to the case of electron tunneling shown in Chap. 2, the spin tunnels from one spin state to another (Fig. 6.1(a)). QTM is observed for the so-called high spin molecules (see e.g. [124]). In this case, temperature depending measurements of the switching times of the single atoms could reveal the tunneling rates when the thermally activated processes are frozen out. A second effect, which has to be taken into account, is the width of the Co states, which carry the magnetic moment. Hybridization of the Co d states with the Pt bands produces broad resonances with a width of the order of 1 eV. It is an open question, whether this effect could increase the switching rate compared to the simple Néel-Brown model.

Anyhow, if one of both effects, QTM or hybridization, increases the switching rate above the critical 10 Hz, there is still the possibility to stabilize the magnetic moments of the Co atoms by applying an external magnetic field. In this case one has to assume a superparamagnetic behavior.

Figure 6.1(c) shows the calculated magnetization M of an ensemble of Co atoms as a function of an applied magnetic field at 0.3 K and at 6.0 K. If one assumes a continuum description as in Ref. [4], the magnetization M is given by

$$M = \frac{\int_0^\pi d\theta \sin \theta \cos \theta \exp(-E(\theta, B)/(k_B T))}{\int_0^\pi d\theta \sin \theta \exp(-E(\theta, B)/(k_B T))}. \quad (6.3)$$

with $E(\theta, B)$ from Eqn. 6.1. According to Ref. [4], this describes the field dependent magnetization of Co atoms on Pt(111) at 5.5 K very well. Obviously a magnetic field of only ± 0.5 T is sufficient to stabilize the magnetic moments in both directions at 0.3 K. This allows for magnetic field dependent measurements on a single Co atom using an out-of-plane sensitive Cr-coated W tip having a stable spin structure up to 2.5 T at least [81].

The above discussion suggests, that single Co atoms on Pt(111) are an interesting system to be studied with respect to the magnetic properties on a local

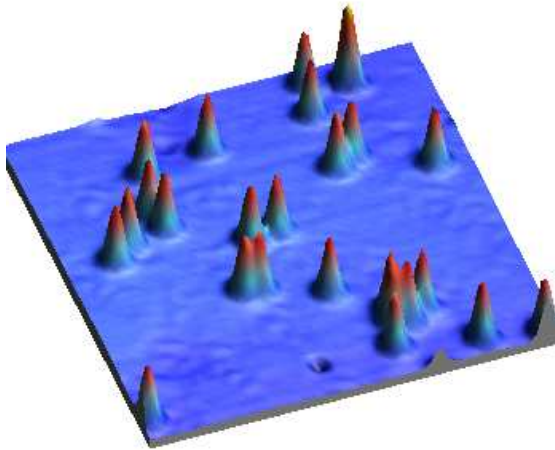


Figure 6.2: Topographic image ($20\text{ nm} \times 20\text{ nm}$) of single Co atoms on the Pt(111) surface. The higher adsorbate in the upper right is probably a multimer or another kind of Co complex. ($T = 0.315\text{ K}$, $U = 1.0\text{ V}$, $I = 0.2\text{ nA}$)

scale. The first two steps in this direction are made and will be described in the following: Spin averaged spectroscopy on single atoms and their manipulation on the Pt(111) surface.

6.2 Preparation

In order to obtain single adatoms, Co has been directly evaporated onto the cold surface of the Pt(111) crystal. The preparation of the Pt(111) substrate was already discussed in Sec. 4.2. The evaporation onto the cold surface is essential to minimize the diffusion length of the atoms and therefore to avoid clustering, island and step flow growth.

A typical Co evaporation procedure is as follows: The STM with the clean Pt crystal is pre-cooled to about 4K in the experimental position (see Fig.3.1). The Co evaporator, which is mounted to the main chamber, is set to a constant flux but the shutter of the evaporator is still closed. The STM is moved down while pumping the 1K-line in order to cool the radiation shield. After reaching the tip/sample exchange position the window of the radiation shield is opened. When the shutter of the evaporator is also opened for typically 2–3 seconds the Co atoms have a direct access to the sample and are deposited onto the Pt surface at a pressure below 2×10^{-10} mbar. After closing the shutter and the radiation shield the STM is moved up to the experimental position where it is cooled down to base temperature. Between opening and closing the radiation shield the sample is directly exposed to the incoming heat radiation from the chamber walls. By keeping this time as short as possible (approx. 30 seconds) the temperature of the STM after reaching the experimental position is below 25K. Fig. 6.2 shows a topographic image of the Pt(111) surface after deposition of 0.3% Co as described

above. Each protrusion corresponds to a single Co atom exhibiting an apparent height of about 0.11 nm.³ Generally the atoms appear very homogeneous not only in height but also in width and shape. The higher adsorbate in the upper right is probably a multimer or another kind of Co complex (see Sec. 6.5).

6.3 Electronic properties

Figure 6.3(a) shows the same area as displayed in Fig. 6.2. Figure 6.3(b) shows two line profiles along the section lines drawn in (a). Both sections reveal the typical apparent height of 0.11 nm. Figures 6.3(c)–(f) display dI/dU maps of the same area as shown in (a) at different bias voltages as indicated. In all images the Pt surface does not appear homogeneous but shows extended scattering patterns. According to the results obtained in Chap. 4 these features can be attributed to scattering from bulk states. All single Co atoms in Fig. 6.3(c) can be clearly distinguished from the Pt(111) surface due to a higher dI/dU intensity. Since the color scale in (c) is inverted, the dI/dU signal above the Co atoms is lower than on the Pt substrate. In contrast to the topography where all atoms appear equally the atoms can be distinguished in dI/dU maps due to weak but significant differences in the dI/dU intensity. Thus we can classify the atoms into two species showing two spectroscopic signatures, type A and type B. The atoms of type B are marked in Figs. 6.3(a)–(f) by circles. Also in Fig. 6.3(d) both species can be observed, but in contrast to the previous image type B appears brighter while the type A appears darker than the substrate. This is conserved in (e) where a strong contrast between both species is obtained by applying a slightly higher voltage of -0.05 V. At a small positive bias voltage the Co atoms are not visible in Fig. 6.3(f). Generally the two atom species type A and type B can be distinguished spectroscopically in a bias voltage range -0.2 V to -0.05 V on many different samples using different tips. In the following we will show that this is related to a different electronic structure of single Co atoms which occupy different surface lattice sites. Other possible contrast mechanisms as different magnetic states or differences due to changed chemical composition can be ruled out.

Figure 6.4(a) shows the topography of five single Co atoms while in (b) the simultaneously recorded dI/dU map is shown. The two species of Co atoms can be clearly distinguished due to their spectroscopic signature and are marked by circles as in Figs. 6.3(a)–(f). Figure 6.4(c) shows the same Co atoms as in (a) but obviously the lateral position of some atoms has been changed. The atoms #1, #2, and #5 changed their positions when the tip passed them. This can be concluded since one part of the atoms is imaged at one position, while the other part is imaged at a different position. Therefore the above atoms changed their position in between two scan lines. Atom #3 shows no discontinuity, but also

³Depending on the electronic states of the tip apex the apparent height may vary by ± 0.1 Å.

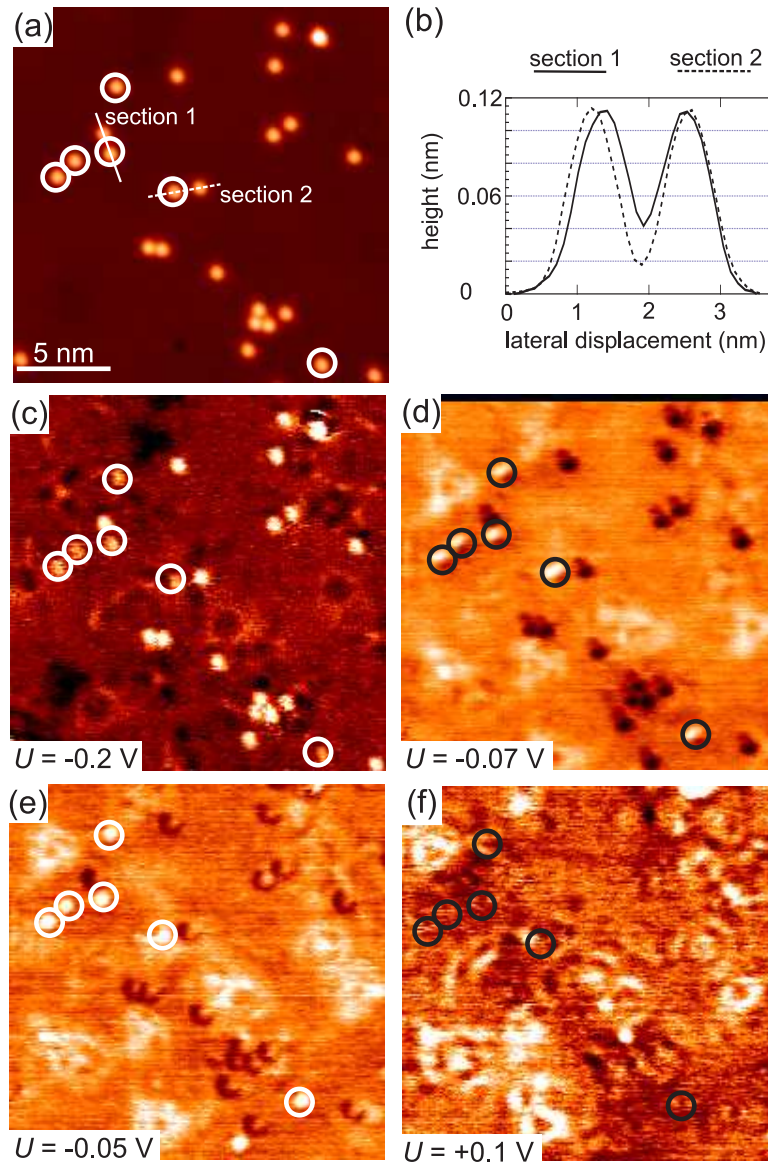


Figure 6.3: (a) Topographic image of single Co atoms on the Pt(111) surface. (b) Sections along indicated lines in (a). (c)–(f) dI/dU maps of area shown in (a) at indicated voltages. In (c)–(e) the Co atoms are distinguishable by two spectroscopic signatures, type A and type B. The position of type B atoms is marked by circles in (a)–(f). The color scale in (c) has been inverted in order to increase the contrast. In (f) no spectroscopic signal of the Co atoms is visible. ($T = 0.315$ K, $I = 1.0$ nA, $U_{\text{mod}} = 5$ mV, (a): $U = -0.2$ V)

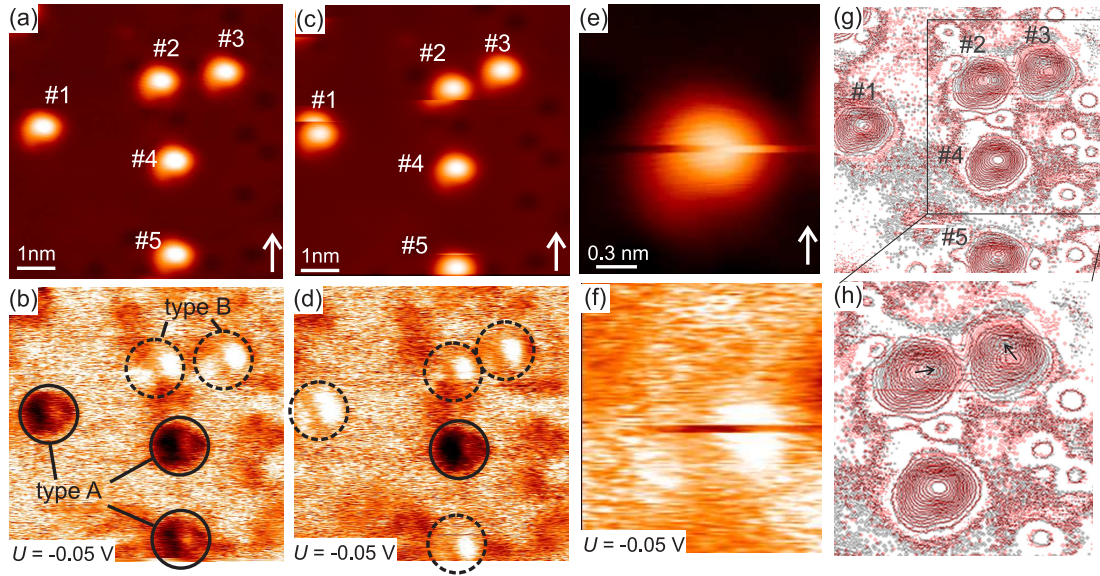


Figure 6.4: (a) Topographic image of five single Co atoms on Pt(111). The white arrow indicates the direction of the slow scan axis. (b) Simultaneously recorded dI/dU map to (a). Two different spectroscopic signatures are observed. (c) Topographic image of the same five single Co atoms on Pt(111). Atoms #1–3 and #5 changed their lateral position compared to (a) during scanning. For tip induced atom movement see text. (d) Simultaneously recorded dI/dU map to (c). (e) Topographic image of a single Co atom, which changed twice its lateral position during scanning. (f) Simultaneously recorded dI/dU map to (e). (g),(h) Superposition of contour plots of (a) and (c). The black arrows in (h) indicate the movement of the center of the atoms. ($T = 0.315$ K, $I = 0.5$ nA, $U_{\text{mod}} = 5$ mV)

moved its position, which becomes obvious by comparing Fig. 6.3(a) with (b). The only atom which did not change its position is atom #4.

The change of the position of the atom has been achieved as follows: Each line of the images in Fig. 6.4 has been scanned twice before scanning the next line, from the left to the right (forward) and from the right to the left (backwards). While for the forward channel the indicated bias voltage of -0.05 V was applied, for the backward channel the bias voltage was set to $+0.1$ V. This bias voltage was found for this tip to cause a tip induced atom movement when passing the atoms. All images shown in Fig. 6.4 are recorded in the forward channel. The manipulation of Co atoms will be discussed in Sec. 6.4. A comparison of the simultaneously recorded dI/dU map in (b) with (d) reveals that two Co atoms (#1 and #5) changed their spectroscopic signature. The remaining three atoms did not change spectroscopically even though two of them have been moved (#2

and #3). In Figure 6.4(e) a single Co atom is shown, which changed its lateral position twice during scanning. It jumped to the right but stayed there only for a few scan lines before jumping back to its former position. The corresponding dI/dU map in (f) clearly reveals the spectroscopic change going in hand with the jump by showing different colors for these scan lines. All in all we can conclude that the Co atoms can change their spectroscopic type from A to B and vice versa by changing their lateral position on the Pt substrate.

In order to measure the position change with high resolution, Fig. 6.4(g) shows a superposition of the contour plots of the images (a) and (c). The perfect matching of the dirt adsorbates on the Pt substrate excludes any drift effects. This allows to confirm that all Co atoms have been moved except for #4. Due to the high lateral resolution of the topographic images (500 pts \times 500 pts) it is possible to determine the length of the lateral position change with an accuracy of 14 pm. This accuracy is much better than the distance of neighboring adsorption sites of 0.16 nm. The arrows in (h) give the length as well as the direction of the jumps. It turns out that the type conserving movements of the atoms #2 and #3 are 0.292 ± 0.020 nm and 0.294 ± 0.020 nm long, respectively. The movements of the atoms #1 and #5 which exhibit a spectroscopic signature change are significantly shorter with 0.172 ± 0.020 nm and 0.171 ± 0.020 nm, respectively.

Several experiments of the kind described above have been evaluated. Figure 6.5(a) shows the lateral displacement coded with different symbols depending on a change or conservation of the spectroscopic signature for each evaluated position change. Obviously there is a clear relation between the displacement distance and the corresponding symbol. All jumps which go in hand with a spectroscopic signature change have an average lateral displacement of 0.174 ± 0.015 nm while movements without a change are of an average length of 0.286 ± 0.012 nm. In addition to the displacement the relative angles of the jumps have been analyzed. Figure 6.5(b) shows the relative angle Φ of the different jumps in respect to the movement #2. While jumps which change the spectroscopic signature exhibit angles of $\Phi = n \cdot 60^\circ + 30^\circ$ with $n \in \{0, 1, 2\}$, the jumps which do not show a spectroscopic change exhibit $\Phi = n \cdot 60^\circ$ with $n \in \{1, 2\}$. Therefore the results summarized in Fig. 6.5(a) and (b) lead to the conclusion that the movements which show a change in the spectroscopic signature are jumps to the nearest neighbor adsorption site, i.e. from fcc to hcp and vice versa. In order to illustrate this relation Fig. 6.5(c) shows a hard sphere model of the Pt(111) surface with two Co atoms on top. Due to the fcc stacking of the Pt crystal the (111) surface offers two non-equal binding sites to the adatoms. The positions are referred to be of type A and B. In order to change the position the indicated Co atoms can either jump 0.16 nm to the nearest neighbor site, which would result in a stacking change, or they keep their stacking by jumping a distance of 0.277 nm to the second nearest neighbor site.

In summary we can conclude that different spectroscopic signatures of the Co

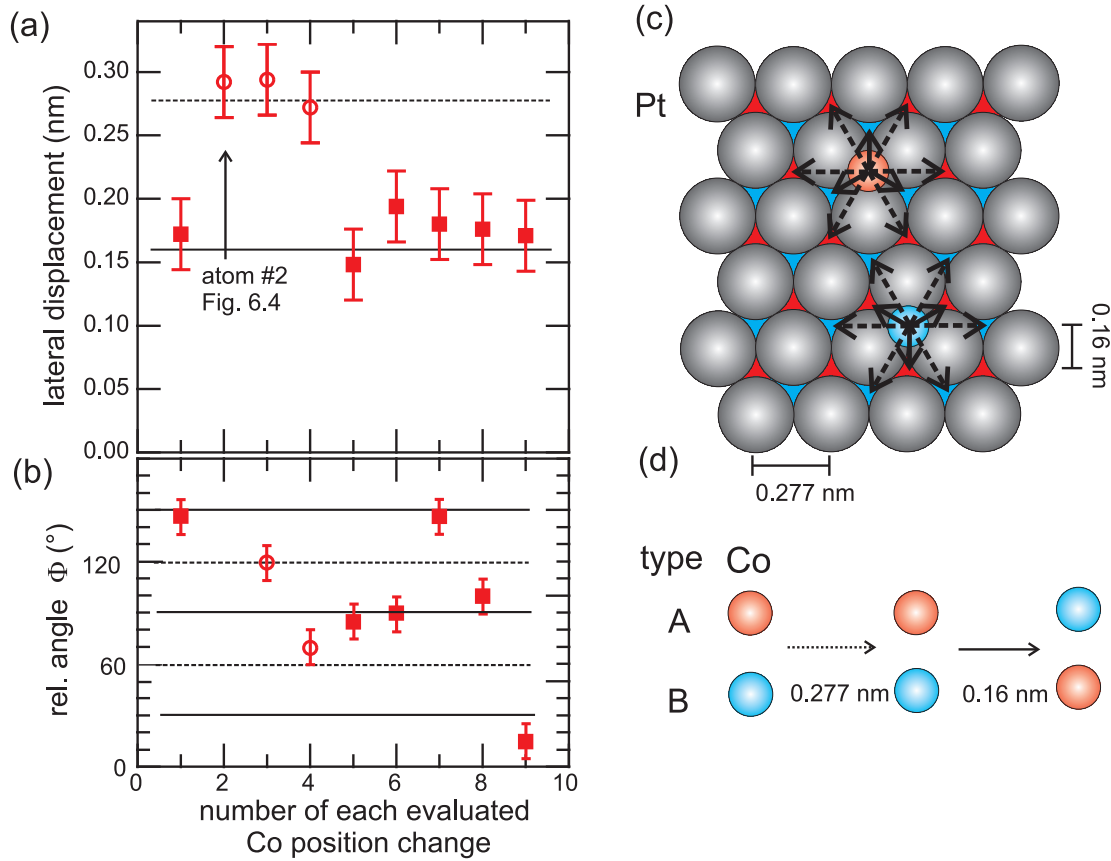


Figure 6.5: (a) Lateral displacement for each position change of some Co atoms. Squares and circles indicate jumps which show a conserved or changed spectroscopic signature, respectively. Solid and dotted lines mark distances from fcc(hcp) to fcc(hcp). (b) Relative angle of the jumps with respect to position change #2 (marked in (a)). (c) Hard sphere model of the Pt(111) surface with two different indicated adsorption sites. Dashed and solid arrows mark jumps to next nearest neighbor and nearest neighbor sites, respectively. (d) Sketch of type conserving and type changing movements with according movement length.

atoms are observed in dI/dU maps in the negative voltage range. This is due to different adsorption sites on the Pt substrate. Up to now, we cannot assign the spectroscopic signature to a corresponding stacking. It is known, that the fcc site is by 25 meV more stable than the hcp site, but the diffusion barrier is 275 meV high and thus much higher than the temperature at which the atoms are deposited ($T < 25$ K) [125]. We thus expect an equal distribution of fcc and hcp stacked atoms. In fact in some of our experiments we saw a predominance of one spectroscopic type while in others the other type is predominant.

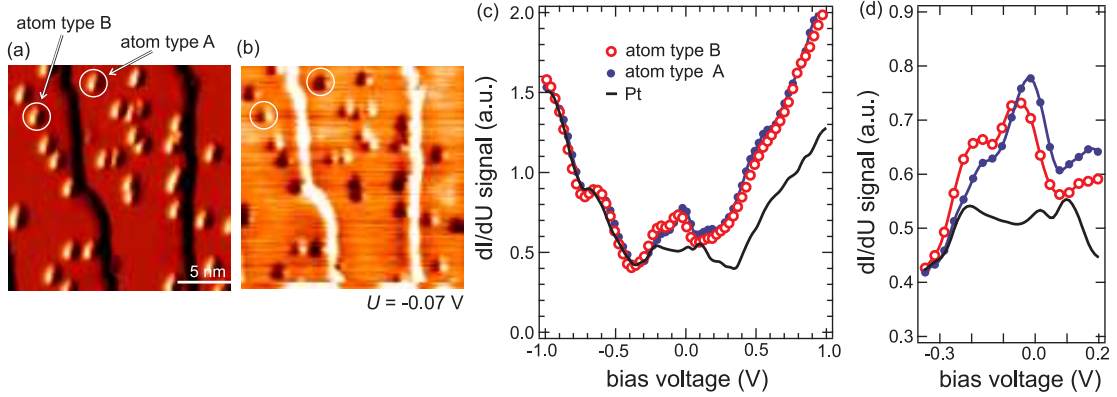


Figure 6.6: (a) Topographic image of single Co atoms on Pt(111) (partly differentiated). (b) dI/dU map measured simultaneously to (a). (c) dI/dU spectra obtained above single Co atoms indicated in (a) and (b), respectively. (d) Magnified view of dI/dU spectra around E_F . ($T = 0.315$ K, $I_{\text{stab}} = 0.5$ nA, $U_{\text{stab}} = -2.0$ V, $U_{\text{mod}} = 50$ mV)

In order to reveal the origin of the differences in the electronic structure, dI/dU spectra have been measured above Co atoms, which appear to be equal in topography (see Fig. 6.6(a)) but different in simultaneously recorded dI/dU maps (see Fig. 6.6(b)). The Co spectra as well as the spectra above the bare Pt surface are displayed in Fig. 6.6(c). From -1.0 V to -0.35 V the three spectra appear quite equal with a nearly linear decrease in conductivity interrupted by a peak at -0.65 eV. For energies above -0.35 eV the Pt shows generally a lower intensity than the Co spectra. Again a broad feature around the Fermi energy and an increasing dI/dU signal starting at $+0.3$ V due to the surface state can be observed for the Pt spectra (e.g. Fig. 4.7). While both Co spectra appear nearly identical in the whole energy range small differences are visible near the Fermi energy. The energy range from -0.35 eV to $+0.2$ eV is shown in Fig. 6.6(d). Both Co spectra exhibit a peak slightly below E_F which is much stronger than that one on the Pt substrate. The peak of the type B atom is shifted energetically downwards by about 50 meV. This spectroscopic difference is the reason for the different spectroscopic signatures observed for both types of atoms in the dI/dU maps. While the general conclusion about the spectroscopic difference between fcc and hcp stacked Co atoms is consistent with a recent publication [87] the advanced assignment of the spectra to a specific stacking by comparison to first principles calculations has to be postponed to the future. Anyhow, this shift in the electronic structure due to different stacking is also consistent with our results on Co monolayer structures presented in Chap. 5.

In order to clarify the question about the existence of the Kondo-effect for single Co atoms on Pt(111) we performed dI/dU spectroscopy with a high lateral

and energy resolution at 0.315 K. Figure 6.7(a) shows the topography of the Co atom. dI/dU spectra above the Co atom and the Pt substrate as indicated in (a) are shown in Fig. 6.7(b). Both spectra exhibit an increased conductance in the negative energy range with a higher intensity for the Co as it has been observed in Fig. 6.6(c). This decrease is also visible on the Pt(111) substrate but much less pronounced. When passing the Fermi energy an abrupt decrease in the dI/dU signal becomes visible. As outlined in Sec. 6.1 the Kondo-effect of single magnetic impurities on non-magnetic substrates has been found by observing the Kondo resonance close to E_F in STS spectra. The shape of the Kondo resonance depends on the relative coupling q of the tip to the localized atomic orbitals and to the delocalized states in the substrate. According to Refs. [104, 105] it is given by a so-called Fano line shape:

$$dI/dU \propto \frac{(q + \epsilon)^2}{1 + \epsilon^2}. \quad (6.4)$$

$\epsilon = (eU - \epsilon_K)/\Gamma$ is the normalized energy and ϵ_K is the position of the resonance of width Γ relative to E_F . According to Ref. [107] ϵ_K varies from -3 meV to +3 meV for Co atoms on various substrates. In order to reveal whether the observed sharp crossover in Fig. 6.7(b) from a high dI/dU signal in the negative energy range to a lower one for positive energy could originate from the Kondo-effect, Fig. 6.7(c) shows several Fano line shapes which have been calculated for different line shape characterizing parameters q . The shape of the line ranges from a dip to a peak depending on q . For q equal to 1 a step-like feature is observed. But in contrast to Fig. 6.7(b) the step has a positive slope around ϵ_K . Thus, the measured feature cannot be fitted by a Fano line shape.

We can summarize that no hints for a Kondo effect for Co on Pt(111) are observed by STS. Generally this can be caused by three reasons: First, the Kondo-effect related feature could be hidden by the characteristic dI/dU intensity change of Co on Pt(111) close to E_F . This is rather unlikely since the Kondo resonances typically cause intensity changes of up to 20% which are comparable with the dI/dU change observed on the present sample. Second, T_K could be too low. According to Eqn. 2.22 the energy resolution of this experiment is 0.75 meV. Assuming that a Fano lineshape with a width of $\Gamma = 2\Delta E$ is still observable, this would result in $T_K \approx 9$ K with $\Gamma = 2k_B T_K$ [126]. Basically this cannot be ruled out but seems to be unlikely too, since $T_K > 55$ K was found for Co atoms on several substrates [107]. The third and most likely reason why no Fano line shape is observed could be the strong magnetocrystalline anisotropy E_A which is sufficient to destroy the Kondo-effect due to $E_A \gg k_B T_K$.

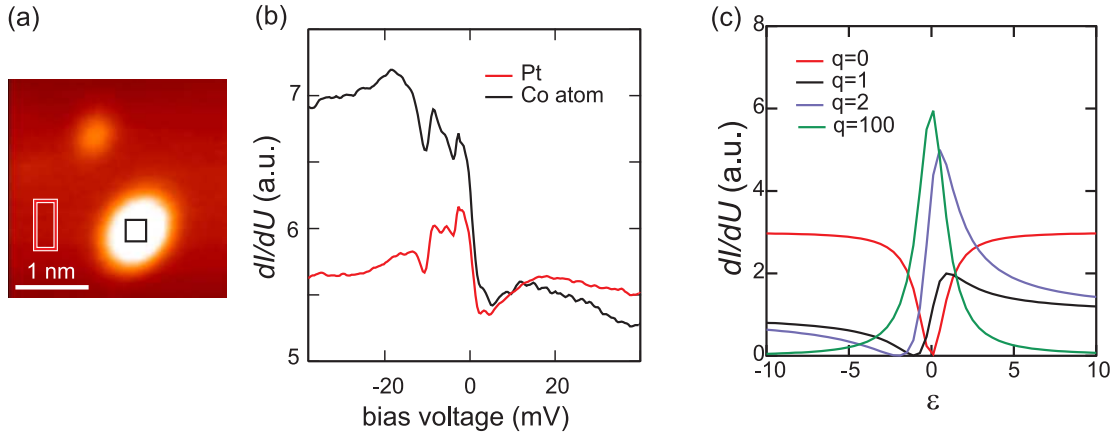


Figure 6.7: (a) Topographic image of a single Co atom on Pt(111). (b) dI/dU spectra obtained above a single Co atom and Pt substrate as indicated in (a). ($T = 0.315$ K, $I_{\text{stab}} = 1.0$ nA, $U_{\text{stab}} = +40$ mV, $U_{\text{mod}} = 0.3$ mV). (c) Calculated Fano line shapes according to Eqn. 6.4.

6.4 Manipulation

This section shows first experiences regarding the manipulation of single Co atoms on Pt(111). The manipulation has already been used to reveal the position-dependent electronic structure of single Co atoms on Pt(111) as described in the previous section.

Manipulation modes

For modifying a surface and changing an arrangement of adsorbates by an STM tip three different parameters play an important role as described in the literature [127]: First, the electrical field between the surface and the tip can decrease the migration barrier at the surface and therefore can induce the diffusion of adsorbates. Second, a sufficient high tunneling current can induce the movement of atoms and molecules due to vibrational excitations. The third and most important parameter, especially for manipulation on metal surfaces, is the strength of the effective force between the tip and the adsorbate at the surface. This effective force is a superposition of several forces, namely the van-der-Waals force, the electro-static force, and the force due to chemical bonds between tip and adsorbate, which is created for very small distances less than 3 \AA . Compared to the electrical field and current effects the effective force is localized [127]. In addition, this force can be very easily tuned by increasing or decreasing the tip-sample distance due to changed tunneling parameters.

Two different ways of manipulating single atoms can be distinguished: the vertical [128, 129] and the lateral mode [130–132]. In the vertical mode the tunneling

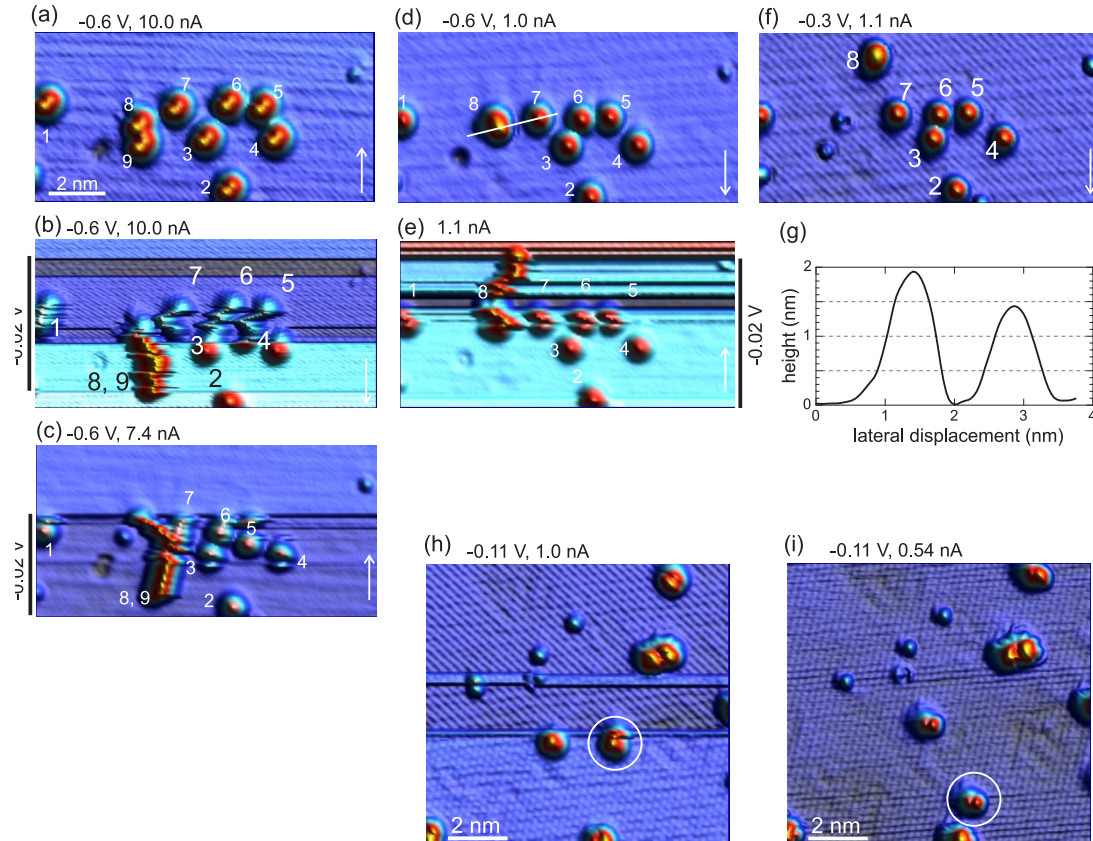


Figure 6.8: Images of an ensemble of nine Co atoms on Pt(111). (a),(d), and (f) Topographic images of the same sample area. (b), (c), and (e) Manipulation images. The bar marks scan lines where a small bias voltage has been applied. White arrows indicate the direction of the slow scan axis. ((a)–(f) $T = 0.315\text{ K}$). (g) Section along the line indicated in (a). (h) Topographic image before manipulating the marked atom in a controlled manner. (i) Topographic image after the manipulation. ($T = 4.2\text{ K}$)

parameters create a tip-adsorbate interaction which is stronger than the substrate-adsorbate interaction. This results in a picking up of the adsorbate by the tip. By changing the tunneling parameters the adsorbate can afterwards be transferred to the substrate at a different position. In the lateral mode the adsorbate never loses the contact during manipulation. The lateral manipulation of Co atoms on Pt(111) has been achieved by using sufficiently low bias voltages in the range of 20 mV and high tunneling currents of about 10 nA as will be described in the following section.

Manipulated Co atoms

Figure 6.8(a) shows six topographic images of an ensemble of nine single Co atoms on the Pt substrate. The white arrow marks the *up* or *down* direction of the slow scan axis. All nine atoms appear with the same height. Due to a small double tip they show a shoulder on the upper right side. Even though the tunneling current is quite high (10 nA), the bias voltage of -0.6 V is obviously not sufficient to induce any movement. While recording the topographic image Fig. 6.8(b) the bias voltage was set to -0.02 V where indicated by the bar on the left. For these scan lines the substrate appears differently and all atoms except #2 and #3 are imaged as stripes. Obviously due to changing the bias voltage to a low value, the tip-adsorbate interaction is tuned in a way, that the Co atoms are following the slow scan direction of the tip movement. Therefore we call the image (b) a *manipulation* image. As visible in this *manipulation* image the movement of the atoms #1 and #4–7 stops and only the movement of #8,9 continues until the bias voltage is reset to -0.6 V. It seems that #8 and #9, which were already close together in (a) are now bound to form a dimer. This is supported by the fact that the tracks of this adsorbate appear higher than the tracks of other adsorbates with the same Pt background. Figure 6.8(c) shows a *manipulation* image for scanning from the bottom to the top of the probed area. Now the dimer formed by #8,9 is moving upwards. Figure 6.8(d) displays the situation after the manipulation. A comparison to (a) reveals a position change of the atoms #1 and #5–7 and a compact Co dimer formed by the two closely located atoms # 8 and #9 in Fig. 6.8(a). In this topographic image the dimer appears a little more elongated and significantly higher than the round single Co atoms as visible in the section (Fig. 6.8(g)) along the line indicated in Fig. 6.8(d). From other STM experiments it is known that individual atoms in the compact shaped dimers cannot be resolved when the inter-atom distance is less than 5 \AA [112]. An additional manipulation image in Fig. 6.8(e) reveals that only the dimer has been moved while the other single Co atoms remain on their former positions. A closer look to the topography after the manipulation in (f) shows that the dimer has been located close to a dirt adsorbate before manipulation.

Figures 6.8(h) and (i) show a controlled manipulation of one single Co atom. After recording Fig. 6.8(h) the tip has been placed directly above the selected atom which is marked by a circle. Then the tunneling parameters for manipulation ($+0.02$ V, 10.0 nA) were applied followed by a lateral tip movement over a distance of 2 nm without scanning. At the new position the parameters were reset to the indicated scanning values. The situation after the manipulation is displayed in Fig. 6.8(i). It is visible that all other adsorbates exhibit their former position except for the marked atom. It has been moved by the chosen length and direction.

These experiments provided us with first experiences regarding the manipulation of single Co atoms on Pt(111) at 0.315 K and 4.2 K.

6.5 Height switching

In the previous sections it has been shown that all single Co atoms appear with equal height in topography while Co dimers show an increased height and width in comparison to the single atoms. For some of our samples it has been observed that some Co atoms appear with a different height in topography and can change their height under certain scanning conditions. This will be called height switching.

Figures 6.9(a) and (b) show two topographic images of single Co atoms on Pt(111), recorded consecutively with a bias voltage of 1 V and a tunneling current of 100 pA. A comparison of both images reveals that the apparent height of the two Co adsorbates marked by circles is changed. The height profiles along the lines in Fig. 6.9(a) and (b) are displayed in (c). In both profiles three different height levels are distinguishable. Taking all Co adsorbates into account, which are visible in (a) and (b), nearly two third exhibit the usual height of 0.14 nm and a nearly perfect spherical shape with a FWHM⁴ of 0.75 nm. The remaining adsorbates show a different height of 0.16 nm or 0.20 nm. A comparison of both line profiles along the lines in (a) and (b) reveals that the marked Co adsorbates A and B switch to different height levels. The Co adsorbate A switches from 0.14 nm to 0.16 nm while B switches from 0.14 nm to 0.20 nm. Such a switching of the height has been observed for some of our samples while scanning with bias voltages in the range of 1 V and above. We also observe the reversed switching from 0.2 nm to 0.14 nm and 0.16 nm to 0.14 nm. In order to exclude that the height switching is related to the individual position of the Co adsorbates described in Sec. 6.3 we probed the spectroscopic signature of the switched adsorbates. Figures 6.9(d) and (e) show topographic images and the simultaneously recorded dI/dU maps which reveal the different positions of the single Co atoms. In Fig. 6.9(d) three atoms have been marked by circles, two of them are of type A and one is of type B according to the results of Sec. 6.3. After scanning at +1.5 V, Fig. 6.9(e) shows the same area. As shown in Fig. 6.9(f) the three marked Co atoms changed in height from 0.12 nm to 0.16 nm. In addition, a tip change took place which leads to an elongated appearance of all adsorbates. In the simultaneously recorded dI/dU maps all height switched atoms appear equally but significantly different from the atoms of type A or B. Their spectroscopic signature is a black spot with a small white satellite spot at the left.

So far the reason for the height switching of the Co atoms is unknown. The previous observations rule out that the height change is related to the position with respect to the Pt substrate. Also magnetic effects are not likely, since the height switching was also observed with nonmagnetic tips. Even though the switched Co adsorbates appear with a similar height as Co dimers, we exclude a tip induced dimer formation, i.e. no Co atoms are transferred from the tip to a single atom on the substrate. Furthermore, no relation of the switching to the site of the

⁴FWHM is an acronym for Full Width at Half Maximum

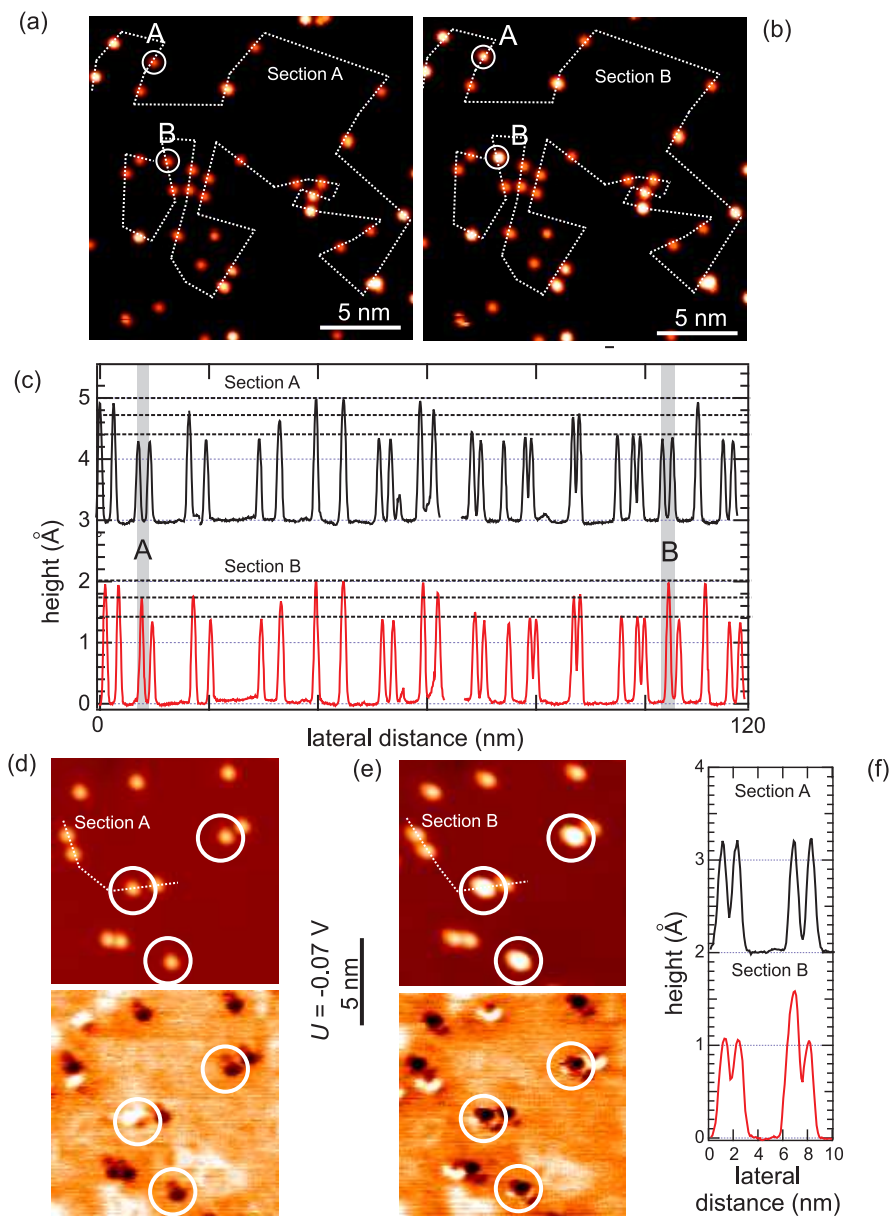


Figure 6.9: (a),(b) Topographic images of Co adsorbates on Pt(111) ($U = 1\text{ V}$, $I = 100\text{ pA}$). Two marked adsorbates exhibit a height change in (b) with respect to (a). (c) Sections along indicated line in (a) and corresponding positions in (b). (d),(e) Topographic images and simultaneously recorded dI/dU maps. (f) Sections along indicated lines in (d) and (e), respectively.

modified adsorbate concerning the vicinity to one of the remaining dirt adsorbate

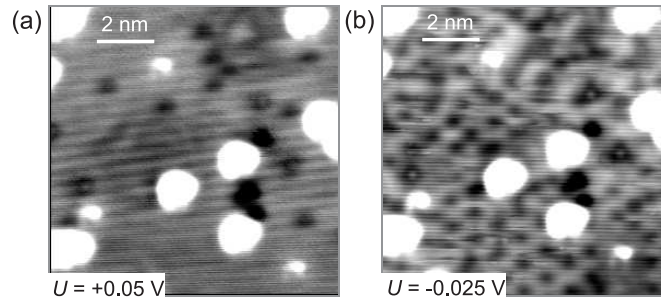


Figure 6.10: (a) Topographic image of single Co atoms on the Pt(111) surface. (b) Topographic image of the same sample area using a lower bias voltage. In contrast to (a) at this bias voltage a hexagonal pattern on the Pt(111) surface becomes visible. This pattern might be caused by adsorbed hydrogen atoms. ($T = 0.315$ K, $I = 6.0$ nA)

was revealed. Thus, there are no experimental hints that such a height change is a tip induced change of the chemical composition of the Co adsorbates by forming a complex with one of the visible dirt adsorbates. The only mechanism we cannot exclude is the formation of a complex of a Co atom with an atom or molecule from the gas phase or with another adsorbate that is not imaged at the scanning parameters. The latter explanation is favored due to the following result:

On some of our samples where we observed the height switching an adsorbate induced hexagonal pattern has been observed using very low bias voltages. Figure 6.10(a) shows a topographic image of several Co atoms on the Pt(111) surface. Except for the known dirt adsorbates only a small modulation in z of 2 pm due to vibrational noise is visible on the substrate. Figure 6.10(b) shows the same area but now imaged using a lower bias voltage. A hexagonal pattern with a nearest-neighbor distance of about 0.9 nm and a modulation in z of up to 5 pm is observed. These patterns can be observed only for low bias voltages $|U| < 25$ mV. For larger bias voltages the pattern disappears as in Fig. 6.10(a). Furthermore, the pattern can be changed by scanning with a higher bias voltage. It is related to a regular arrangement of an adsorbate. Since the occurrence is only observed on some samples, it is probably not related to an intrinsic property but somehow related to the preparation process. Our favored explanation is the deposition of hydrogen from the gas phase since hydrogen represents the largest fraction of the UHV background pressure gases. From STM experiments on Cu(111) at 5 K it is known that the closed ML of H_2 forms a hexagonal pattern (nearest-neighbor distance of about 0.4 nm) similar to our observations [133]. The influence of hydrogen to single metal adsorbates has been studied by room temperature STM experiments on Pt adatoms on Pt(110)-(1 \times 2). It was revealed that hydrogen atoms form Pt-H complexes, which appear 0.4 Å higher than pure Pt adatoms in

STM images [134].

These results suggest, that the height switching is related to the formation of complexes from Co atoms and one or several H atoms, which are manipulated from the substrate on the atom by the tip. This hypothesis could be proven by a controlled dosing of H onto the Co/Pt(111) sample.

6.6 Summary

In conclusion a detailed study of the site dependent and spin-averaged electronic structure of single Co atoms on Pt(111) has been presented.

Although Co atoms appear uniformly in topographic images, it is possible to distinguish two different species in dI/dU maps and dI/dU spectra. It has been shown that the specific spectroscopic signature can be related to the adsorption of the single atoms at fcc or hcp positions with respect to the Pt(111) substrate. The spectroscopic difference between the differently adsorbed atoms is a small shift in the electronic structure similar to the results on Co monolayer and double-layer nanostructures presented in Chap. 5. But in contrast to the extended layers the spectroscopic differences showed up in a narrow energy range close to the Fermi energy. These results are in excellent agreement with a recent publication by Yayon *et al.* [87]. No indications for a Kondo-effect around the Fermi energy were found using an energy resolution of less than 1 meV. Thus, either the Kondo temperature is far below or the magnetocrystalline anisotropy is large enough to stabilize the magnetic moments of the Co atoms.

First experiments showing the successful manipulation of Co atoms were performed. We can conclude, that even with a software and hardware system, which is not optimized for manipulation procedures, it is feasible to manipulate Co atoms on Pt(111) in a well controlled manner. After an improvement of the technical conditions it should be possible to construct Co chains of different length and shape and investigate their magnetic properties by SP-STM.

Even though a final prove for the mechanism which causes the height switchings is missing, the presented results favor the explanation, that complexes are formed from Co atoms and one or more H atoms. These appear several tens of a pm higher in topography and can be identified by their spectroscopic signature in dI/dU maps. Such Co-H complexes provide an interesting model system to study their electronic and magnetic properties.

The results presented in this Chapter make a contribution to the understanding of the spin-averaged electronic properties of single Co atoms on Pt(111), which is the basis for future studies of the magnetic properties using spin-resolved STM.

7 Conclusions and outlook

In this thesis the electronic properties of the bare Pt(111) surface, the structural, electronic, and magnetic properties of monolayer and double-layer high Co nanostructures on Pt(111) as well as the spin-averaged electronic structure of single Co atoms on Pt(111) were studied.

Most of the scanning tunneling microscopy and spectroscopy experiments have been performed in an STM facility operating at temperatures of down to 0.3 K and magnetic fields of up to 14 T under ultra-high vacuum conditions. Within the time period of this thesis the facility has been taken into operation. The performed characterization measurements revealed a very high stability of the tunneling junction and an energy resolution of about $100 \mu\text{eV}$.

The (111)-surface of a Pt single crystal has been investigated at 0.3 K by scanning tunneling spectroscopy. By imaging scattering states on the Pt(111) surface and by measuring the local density of states the dispersion of an unoccupied surface state on Pt(111) was measured experimentally for the first time. Due to a comparison of the measured dispersion to the band structure, which has been obtained by density functional theory calculations, the surface state was assigned to a *sp* derived surface state. It is located close to the bottom of the projected bulk band gap and exhibits a strong spin-orbit induced spin-splitting. The close vicinity to the bulk bands leads to a strong linear contribution to the dispersion and thus to a deviant appearance in the density of states in comparison to the surface states of the (111) surfaces of noble metals.

Monolayer and double-layer high Co nanostructures on the Pt(111) surface reveal an interrelation of their structural, electronic, and magnetic properties as investigated by spin-resolved scanning tunneling microscopy and spectroscopy at 13 K. An inhomogeneous stacking of the Co atoms within both kinds of nanostructures due to the large lattice mismatch between Co and Pt is found. This causes an inhomogeneous electronic structure of the nanostructures especially below the Fermi energy which also changes the energy resolved spin-polarization on the scale of only a few Å. In the case of the monolayer high Co nanostructures insights into the stacking-dependent energy shifts of dominant peaks in the local density of states are given by density functional theory calculations for pseudomorphic Co layers on Pt(111) in different stacking. These calculations show that the dominant features in the local density of states of Co originate from a *d* like Co surface resonance, which hybridizes stacking dependent with *sp* CoPt states.

The magnetic state of all probed Co nanostructures was found to be out-of-

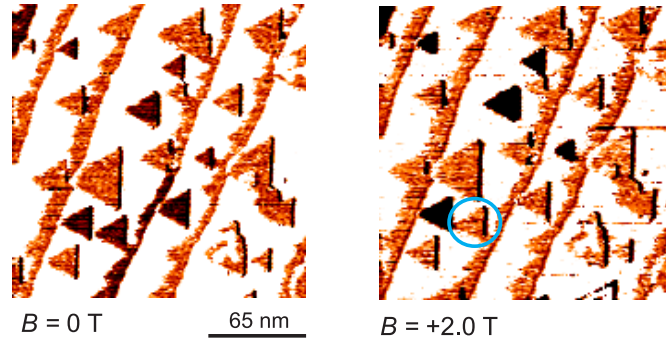


Figure 7.1: left: dI/dU map of Co monolayer wires and islands on the Ir(111) surface. An out-of-plane sensitive magnetic Fe-coated tip was used. The Ir(111) substrate appears white. The two different colors of Co wires and islands indicate opposite magnetic states. right: By applying a magnetic field of +2.0 T only one single marked Co island switched its magnetic state. ($I = 1.5 \text{ nA}$, $U = -0.4 \text{ V}$, $T = 12.7 \text{ K}$)

plane. By studying the domain wall width on Co monolayer wires the exchange length was determined. In contrast to Ref. [7] no indications for a change of the anisotropy from the in-plane direction for the atoms within the islands to an out-of-plane direction for the rim atoms were found. Instead, a uniform out-of-plane anisotropy of $+0.08 \text{ meV/atom} \leq K_{\text{eff}} \leq +0.17 \text{ meV/atom}$ was found for atoms of the monolayer. Measurements in the presence of a magnetic field gave insights into the influence of the sample morphology on the coercivity of the probed nanostructures. The coercivity of Co double-layer nanostructures is found to be surprisingly high with $\mu_0 H_c > 2.0 \text{ T}$.

Single Co atoms on Pt(111) show a spectroscopic signature dependence on different adsorption sites on the substrate as observed for the Co atoms within the Co monolayer nanostructures. In contrast to the monolayer the spectroscopic difference was found in an energy range close to the Fermi energy. No hints for a feature related to the Kondo-effect was observed. This leads to the conclusion, that either the Kondo temperature of Co/Pt(111) is far below 10 K, or the magnetic anisotropy of 9 meV per Co atom found by Ref. [8] is indeed large enough to stabilize the magnetic moment of a single Co atom at 0.3 K. Besides first experiments on the manipulation of the Co atoms, indications for H-Co complexes were found on the Pt(111) surface. The formation of these complexes influences the topographic as well as the spectroscopic appearance of the Co adsorbates in comparison to pure Co atoms.

The main future goal is probing the magnetic state of a single atom on a non-magnetic substrate. Based on the results of this thesis a lot of premises for promising spin-resolved experiments are fulfilled. Concerning the technical requirements the ^3He STM facility operates with a very high lateral and energy resolution even in the presence of high magnetic fields. From the experimental point of view wide knowledge and experience about the preparation and the spin-averaged electronic structure of the single Co atoms have been obtained. Taking into account the results concerning the magnetic properties of the Co nanostructures a promising experiment is given by the common preparation of Co double-layer nanostructures and single atoms. The high coercivity of the nanostructures would allow to probe the magnetic state of an out-of-plane sensitive Cr-tip even in the presence of an applied magnetic field. Therefore, a fully characterized tip can be used to study the magnetism of the single atoms on the same sample area.

A preliminary result of a similar magnetic Co system is shown in Fig. 7.1. Co monolayer islands and wires were deposited on Ir(111) at room temperature. In contrast to Co on Pt(111) the nanostructures grow in a pseudomorphic mode. Concerning the electronic structure and the direction of the magnetic anisotropy it behaves quite similar to the Co on Pt(111) system. Measurements in the presence of an applied external magnetic field reveal that 2 T are obviously not sufficient to switch the magnetic states of the islands. This might indicate a high substrate driven magnetocrystalline anisotropy, which could be even higher than for the Co/Pt(111) system. Thus, Co atoms on Ir(111) are also a promising system to study the magnetization of single atoms and chains by SP-STs.

Bibliography

- [1] F. J. Himpsel, J. E. Ortega, G. J. Mankey, R. F. Willis: *Magnetic nanostructures*. Adv. Phys. **47**, 511 (1998).
- [2] I. Zutic, J. Fabian, S. D. Sarma: *Spintronics: Fundamentals and applications*. Rev. Mod. Phys. **76**, 323 (2004).
- [3] S. Blügel, G. Bihlmayer: *Reduced Dimensions in: Magnetism goes Nano*, edited by S. Blügel, T. Brückner and C. M. Schneider, (Schriften des Forschungszentrums Jülich 2005).
- [4] P. Gambardella, S. Rusponi, M. Veronese, S. Dhesi, C. Grazioli, A. Dallmeyer, I. Cabria, R. Zeller, P. Dederichs, K. Kern, C. Carbone, H. Brune: *Giant Magnetic Anisotropy Of Single Cobalt Atoms And Nanoparticles*. Science **300**, 1130 (2003).
- [5] J. Thiele, C. Boeglin, K. Hricovini, F. Chevrier: *Magnetic circular x-ray-dichroism study of Co/Pt(111)*. Phys. Rev. B **53**, R11934 (1996).
- [6] M. Wellhöfer, M. Weißenborn, R. Anton, S. Pütter, H. P. Oepen: *Morphology and magnetic properties of ECR ion beam sputtered Co/Pt films*. J. Magn. Mater. **292**, 345 (2005).
- [7] S. Rusponi, T. Cren, N. Weiss, M. Epple, P. Bulushek, L. Claude, H. Brune: *The Remarkable Difference Between Surface And Step Atoms In The Magnetic Anisotropy Of Two-Dimensional Nanostructures*. Nature Materials **2**, 546 (2003).
- [8] P. Gambardella, A. Dallmeyer, K. Maiti, M. Malagoli, W. Eberhardt, K. Kern, C. Carbone: *Ferromagnetism In One-Dimensional Monatomic Metal Chains*. Nature **416**, 301 (2002).
- [9] P. Gambardella, A. Dallmeyer, K. Maiti, M. Malagoli, S. Rusponi, P. Ohresser, W. Eberhardt, C. Carbone, K. Kern: *Oscillatory Magnetic Anisotropy In One-Dimensional Atomic Wires*. Phys. Rev. Lett. **93**, 077203 (2004).
- [10] G. Binnig, H. Rohrer, C. Gerber, E. Weibel: *Tunneling through a controllable vacuum gap*. Applied Physics Letters **40**, 178 (1982).

- [11] G. Binnig, H. Rohrer, C. Gerber, E. Weibel: *Surface Studies by Scanning Tunneling Microscopy*. Phys. Rev. Lett. **49**, 57 (1982).
- [12] R. Wiesendanger, H.-J. Güntherodt, G. Güntherodt, R. J. Gambino, R. Ruf: *Observation of vacuum tunneling of spin-polarized electrons with the scanning tunneling microscope*. Phys. Rev. Lett. **65**, 247 (1990).
- [13] M. Bode: *Spin-Polarized Scanning Tunneling Microscopy*. Rep. Prog. Phys. **66**, 523 (2003).
- [14] R. Wiesendanger: *Scanning Probe Microscopy and Spectroscopy*. Cambridge University Press, Cambridge (1994).
- [15] C. J. Chen: *Introduction to Scanning Tunneling Microscopy*. Oxford University Press, New York, Oxford (1993).
- [16] G. Binnig, H. Rohrer: *Scanning Tunneling Microscopy*. Helv. Phys. Acta **55**, 726 (1982).
- [17] J. Tersoff, D. R. Hamann: *Theory and Application for the Scanning Tunneling Microscope*. Phys. Rev. Lett. **50**, 1998 (1983).
- [18] J. Bardeen: *Tunnelling from a Many-Particle Point of View*. Phys. Rev. Lett. **6**, 57 (1961).
- [19] V. A. Ukraintsev: *Data evaluation technique for electron-tunneling spectroscopy*. Phys. Rev. B **53**, 11176 (1996).
- [20] D. Haude: *Rastertunnelspektroskopie auf der InAs(110)-Oberfläche: Untersuchungen an drei-, zwei-, und nulldimensionalen Elektronensystemen im Magnetfeld*. Thesis, Institute of Applied Physics, University of Hamburg (2001).
- [21] A. Wachowiak: *Aufbau einer 300mK-Ultrahochvakuum-Rastertunnelmikroskopie-Anlage mit 14 Tesla Magnet und spinpolarisierte Rastertunnelspektroskopie an ferromagnetischen Fe-Inseln*. Thesis, Institute of Applied Physics, University of Hamburg (2003).
- [22] J. C. Slonczewski: *Conductance and exchange coupling of two ferromagnets separated by a tunneling barrier*. Phys. Rev. B **39**, 6995 (1989).
- [23] T. Miyazaki, N. Tezuka: *Giant magnetic tunneling effect in Fe/Al₂O₃/Fe junction*. J. Magn. Magn. Mater. **139**, L231 (1995).
- [24] S. Heinze: *First Principle Theory of Scanning Tunneling Microscopy Applied to Transition-Metal Surfaces*. Thesis, University of Hamburg (2000).

- [25] D. Wortmann, S. Heinze, P. Kurz, G. Bihlmayer, S. Blügel: *Resolving Complex Atomic-Scale Spin Structures by Spin-Polarized Scanning Tunneling Microscopy*. Phys. Rev. Lett. **86**, 4132 (2001).
- [26] A. Kubetzka, M. Bode, O. Pietzsch, R. Wiesendanger: *Spin-Polarized Scanning Tunneling Microscopy With Antiferromagnetic Probe Tips*. Phys. Rev. Lett. **88**, 057201 (2002).
- [27] J. Wiebe: *Aufbau einer 300mK-Ultrahochvakuum- Rastertunnelmikroskopie-Anlage mit 14T-Magnet und Untersuchung eines stark ungeordneten zweidimensionalen Elektronensystems*. Thesis, Institute of Applied Physics, University of Hamburg (2003).
- [28] Oxford Instruments/Research Instruments, Tubney Woods, Abingdon, Oxon, OX13 SQX, England.
- [29] J. Wiebe, A. Wachowiak, F. Meier, D. Haude, T. Foster, M. Morgenstern, R. Wiesendanger: *A 300 mK ultra-high vacuum scanning tunneling microscope for spin-resolved spectroscopy at high energy resolution*. Rev. Sci. Instrum. **75**, 4871 (2004).
- [30] F. Meier: *Aufbau eines temperaturvariablen MOKE-Systems zur Charakterisierung ultradünner Schichten im Ultrahochvakuum*. Diplomarbeit, Institute of Applied Physics, University of Hamburg (2002).
- [31] S. H. Pan, International Patent Publication No. WO 93/19494 (International Bureau, World Intellectual Property Organization), Sep 30, 1993.
- [32] G. Mariotto, M. D. Angelo, I. V. Shvets: *Dynamic behavior of a piezowalker, inertial and frictional configurations*. Rev. Sci. Instrum. **70**, 3651 (1999).
- [33] J. Klijn, L. Sacharow, Chr. Meyer, S. Blügel, M. Morgenstern, R. Wiesendanger: *STM measurements on the InAs(110) surface directly compared with surface electronic structure calculations*. Phys. Rev. B **68**, 205327 (2003).
- [34] H. F. Hess, R. B. Robinson, R. C. Dynes, J. M. Valles, J. V. Waszczak: *Scanning-Tunneling-Microscope Observation of the Abrikosov Flux Lattice and the Density of States near and inside a Fluxoid*. Phys. Rev. Lett. **62**, 214 (1989).
- [35] M. Tinkham: *Introduction to Superconductivity, 2nd. Ed.* McGraw-Hill, Inc. (1996).
- [36] J. Bardeen: *Tunnelling from a Many-Particle Point of View*. Phys. Rev. Lett. **6**, 57 (1961).

- [37] J. Tersoff, D. R. Hamann: *Theory of the scanning tunneling microscope*. Phys. Rev. B **31**, 805 (1985).
- [38] J. Bardeen, L. N. Cooper, J. R. Schrieffer: *Theory of Superconductivity*. Phys. Rev. **108**(5), 1175 (1957).
- [39] H. F. Hess, R. B. Robinson, J. V. Waszczak: *STM spectroscopy of vortex cores and the flux lattice*. Physica B **169**, 422 (1991).
- [40] S. H. Pan, E. W. Hudson, J. C. Davis: *Vacuum tunneling of superconducting quasiparticles from atomically sharp scanning tunneling microscope tips*. Appl. Phys. Lett. **73**, 2992 (1998).
- [41] M. Pratzner, H. J. Elmers, M. Bode, O. Pietzsch, A. Kubetzka, R. Wiesendanger: *Atomic-Scale Magnetic Domain Walls in Quasi-One-Dimensional Fe Nanostripes*. Phys. Rev. Lett. **87**, 127201 (2001).
- [42] M. Bode, R. Pascal, R. Wiesendanger: *STM study of carbon-induced reconstructions on W(110): strong evidence for a surface lattice deformation*. Surf. Sci. **344**, 185 (1995).
- [43] K. von Bergmann: *Iron nanostructures studied by spin-polarized scanning tunneling microscopy*. Thesis, University of Hamburg (2004).
- [44] T. K. Yamada, M. M. J. Bischoff, T. Mizoguchi, H. van Kempen: *Use of voltage pulses to detect spin-polarized tunneling*. Appl. Phys. Lett. **82**, 1437 (2003).
- [45] N. Memmel: *Monitoring and modifying properties of metal surfaces by electronic surface states*. Surf. Sci. Rep. **32**, 91 (1998).
- [46] M. F. Crommie, C. P. Lutz, D. M. Eigler: *Imaging standing waves in a two-dimensional electron gas*. Nature **363**, 524 (1993).
- [47] Y. Hasegawa, P. Avouris: *Direct Observation of Standing Wave Formation at Surface Steps Using Scanning Tunneling Spectroscopy*. Phys. Rev. Lett. **71**, 1071 (1993).
- [48] F. E. Olson, M. Persson, A. G. Borisov, J.-P. Gauyacq, J. Lagoute, S. Fölsch: *Localization of the Cu(111) Surface State by Single Cu Adatoms*. Phys. Rev. Lett. **93**, 206803 (2004).
- [49] L. Limot, E. Pehlke, J. Kröger, R. Berndt: *Surface-State Localization at Adatoms*. Phys. Rev. Lett. **94**, 036805 (2005).

- [50] F. Silly, M. Pivetta, M. Ternes, F. Patthey, J. P. Pelz, W.-D. Schneider: *Creation of an Atomic Superlattice by Immersing Metallic Adatoms in a Two-Dimensional Electron Sea*. Phys. Rev. Lett. **92**, 16101 (2004).
- [51] J. Li, W.-D. Schneider, R. Berndt, O. R. Bryant, S. Crampin: *Surface-State Lifetime Measured by Scanning Tunneling Spectroscopy*. Phys. Rev. Lett. **81**, 4464 (1998).
- [52] L. Limot, T. Maroutian, P. Johansson, R. Berndt: *Surface-State Stark Shift in a Scanning Tunneling Microscope*. Phys. Rev. Lett. **91**, 196801 (2003).
- [53] S. LaShell, B. A. McDougall, E. Jensen: *Spin Splitting of an Au(111) Surface State Band Observed with Angle Resolved Photoelectron Spectroscopy*. Phys. Rev. Lett. **77**, 3419 (1996).
- [54] L. Petersen, P. Hedegård: *A simple tight-binding model of spin-orbit splitting of sp-derived surface states*. Surf. Sci. **459**, 49 (2000).
- [55] G. Nicolay, F. Reinert, S. Hüfner, P. Blaha: *Spin-orbit splitting of the L-gap surface state on Au(111) and Ag(111)*. Phys. Rev. B **65**, 033407 (2001).
- [56] A. Zangwill: *Physics at surfaces*. (University Press, Cambridge, 1988).
- [57] H. Lüth: *Surfaces and Interfaces of Solid Materials*. (Springer, Berlin Heidelberg New York, 1995).
- [58] S. D. Kevan: *Evidence for a New Broadening Mechanism in Angle-Resolved Photoemission from Cu(111)*. Phys. Rev. Lett. **50**, 526 (1983).
- [59] S. D. Kevan, R. H. Gaylord: *High-resolution photoemission study of the electronic structure of the noble-metal (111) surfaces*. Phys. Rev. B **36**, 5809 (1987).
- [60] O. Krupin, G. Bihlmayer, K. Starke, S. Gorovikov, J. E. Prieto, K. Dobrich, S. Blügel, G. Kaindl: *Rashba effect at magnetic metal surfaces*. Phys. Rev. B **71**, 201403 (2005).
- [61] M. Donath, F. Passek, V. Dose: *Surface State Contribution of the Magnetic Moment of Ni(111)*. Phys. Rev. Lett. **70**, 2802 (1993).
- [62] J. Braun, M. Donath: *Contest between surface resonances and surface states at 3d ferromagnets*. Europhys. Lett. **59**, 592 (2002).
- [63] S. Pons, P. Mallet, L. Magaud, J. Y. Veuille: *Investigation of the Ni(111) Shockley-like surface state using confinement to artificial nanostructures*. Europhys. Lett. **61**, 375 (2003).

- [64] S. L. Hulbert, P. D. Johnson, M. Weinert: *High-resolution inverse-photoemission study of the Pd(111) surface*. Phys. Rev. B **34**, 3670 (1986).
- [65] A. Schäfer, I. L. Shumay, M. Wiets, M. Weinelt, T. Fauster, E. V. Chulkov, V. M. Silkin, P. M. Echenique: *Lifetimes of unoccupied surface states on Pd(111)*. Phys. Rev. B **61**, 13159 (2000).
- [66] P. Roos, E. Bertel, K. D. Rendulic: *Observation of an sp-derived surface resonance on Pt(111) indicating the crucial role of surface states in physisorption*. Chem. Phys. Lett. **232**, 537 (1995).
- [67] N. Memmel, E. Bertel: *Role of Surface States for the Epitaxial Growth on Metal Surfaces*. Phys. Rev. Lett. **75**, 485 (1995).
- [68] R. Drube, V. Dose, A. Goldmann: *Empty Electronic States at the (1×1) and (5×20) Surfaces of Pt(100): an Inverse Photoemission Study*. Surf. Sci. **197**, 317 (1988).
- [69] A. Kokalj, M. Causà: *Periodic density functional theory study of Pt(111): surface features of slabs of different thicknesses*. J. Phys.: Condens. Matter **11**, 7463 (1999).
- [70] S. Link, H. A. Dürr, G. Bihlmayer, S. Blügel, W. Eberhardt, E. V. Chulkov, V. M. Silkin, P. M. Echenique: *Periodic density functional theory study of Pt(111): surface features of slabs of different thicknesses*. Phys. Rev. B **63**, 115420 (2001).
- [71] M. F. Crommie, C. P. Lutz, D. M. Eigler: *Spectroscopy of a single adsorbed atom*. Phys. Rev. B **48**, 2851 (1993).
- [72] M. Hohage, M. Bott, M. Morgenstern, Z. Zhang, T. Michely, G. Comsa: *Atomic Processes in Low Temperature Pt-Dendrite Growth on Pt(111)*. Phys. Rev. Lett. **76**, 2366 (1996).
- [73] M. Bott, M. Hohage, M. Morgenstern, T. Michely, G. Comsa: *New Approach for Determination of Diffusion Parameters of Adatoms*. Phys. Rev. Lett. **76**, 1304 (1996).
- [74] J. Wintterlin, R. Schuster, G. Ertl: *Existence of a "Hot" Atom Mechanism for the Dissociation of O₂ on Pt(111)*. Phys. Rev. Lett. **77**, 123 (1996).
- [75] K. Bedürftig, S. Volkening, Y. Wang, J. Wintterlin, K. Jacobi, G. Ertl: *Vibrational and structural properties of OH adsorbed on Pt(111)*. The Journal of Chemical Physics **111**, 11147 (1999).

- [76] B. C. Stipe, M. A. Rezaei, W. Ho, S. Gao, M. Persson, B. I. Lundqvist: *Single-Molecule Dissociation by Tunneling Electrons*. Phys. Rev. Lett. **78**, 4410 (1997).
- [77] J. Li, W. D. Schneider, R. Berndt: *Local density of states from spectroscopic scanning-tunneling-microscope images: Ag(111)*. Phys. Rev. B **56**, 7656 (1997).
- [78] S. Baud, C. Ramseyer, G. Bihlmayer, S. Blügel, C. Barreteau, M. C. Desjonquères, D. Spanjaard, N. Bernstein: *Comparative study of ab initio and tight-binding electronic structure calculations applied to platinum surfaces*. Phys. Rev. B **70**, 235423 (2004).
- [79] J. Kliewer, R. Berndt, E. Chulkov, V. Silkinand, P. Echenique, S. Crampin: *Dimensionality effects in the lifetime of surface states*. Science **288**, 1399 (2000).
- [80] L. Diekhöner, M. Schneider, A. Baranov, V. Stepanyuk, P. Bruno, K. Kern: *Surface States Of Cobalt Nanoislands On Cu(111)*. Phys. Rev. Lett. **90**, 236801 (2003).
- [81] O. Pietzsch, A. Kubetzka, M. Bode, R. Wiesendanger: *Spin-Polarized Scanning Tunneling Spectroscopy Of Nanoscale Cobalt Islands On Cu(111)*. Phys. Rev. Lett. **92**, 057202 (2004).
- [82] L. Niebergall, V. S. Stepanyuk, J. Berakdar, P. Bruno: *Controlling the Spin Polarization of Nanostructures on Magnetic Substrates*. Phys. Rev. Lett. **96**, 127204 (2006).
- [83] O. Pietzsch, S. Okatov, A. Kubetzka, M. Bode, S. Heinze, A. Lichtenstein, R. Wiesendanger: *Spin-Resolved Electronic Structure of Nanoscale Cobalt Islands on Cu(111)*. Phys. Rev. Lett. **96**, 237203 (2006).
- [84] S. Rusponi, N. Weiss, T. Cren, M. Epple, H. Brune: *High Tunnel Magnetoresistance In Spin-Polarized Scanning Tunneling Microscopy Of Co Nanoparticles On Pt(111)*. Appl. Phys. Lett. **87**, 2514 (2005).
- [85] P. Grütter, U. Dürig: *Growth Of Vapor-Deposited Cobalt Films On Pt(111) Studied By Scanning-Tunneling-Microscopy*. Phys. Rev. B **49**, 2021 (1994).
- [86] E. Lundgren, B. Stanka, M. Schmid, P. Varga: *Thin Films Of Co On Pt(111): Strain Relaxation And Growth*. Phys. Rev. B **62**, 2843 (2000).
- [87] Y. Yayon, X. Lu, M. F. Crommie: *Bimodal electronic structure of isolated Co atoms on Pt(111)*. Phys. Rev. B **73**, 155401 (2006).

- [88] A. Vázquez de Parga, F. Garcíá-Vidal, R. Miranda: *Detecting Electronic States At Stacking Faults In Magnetic Thin Films By Tunneling Spectroscopy*. Phys. Rev. Lett. **85**, 4365 (2000).
- [89] S. Okuno, T. Kishi, K. Tanaka: *Spin-Polarized Tunneling Spectroscopy Of Co(0001) Surface States*. Phys. Rev. Lett. **88**, 066803 (2002).
- [90] M. Pratzner, H. Elmers: *Structure And Electronic Properties Of Ultrathin Co Films On W(110)*. Surf. Sci. **550**, 223 (2004).
- [91] M. Pratzner, H. Elmers: *Scanning Tunneling Spectroscopy Of Dislocations In Ultrathin Fcc And Hcp Co Films*. Phys. Rev. B **72**, 035460 (2005).
- [92] J. Wiebe, L. Sacharow, A. Wachowiak, G. Bihlmayer, S. Heinze, S. Blügel, M. Morgenstern, R. Wiesendanger: *Scanning Tunneling Spectroscopy On Co(0001): Spectroscopic Signature Of Stacking Faults And Dislocation Lines*. Phys. Rev. B **70**, 035404 (2004).
- [93] M. Bode, R. Wiesendanger: *Spin-Polarized Scanning Tunneling Spectroscopy* in: *Magnetic Microscopy of Nanostructures*, edited by H. Hopster and H. P. Oepen, (Springer, Berlin, 2006).
- [94] O. Pietzsch, A. Kubetzka, D. Haude, M. Bode, R. Wiesendanger: *A Low-Temperature Ultrahigh Vacuum Scanning Tunneling Microscope With A Split-Coil Magnet And A Rotary Motion Stepper Motor For High Spatial Resolution Studies Of Surface Magnetism*. Rev. Sci. Instrum. **71**, 424 (2000).
- [95] E. Lundgren, B. Stanka, W. Koprolin, M. Schmid, P. Varga: *An Atomic-Scale Study Of The Co Induced Dendrite Formation On Pt(111)*. Surf. Sci. **423**, 357 (1999).
- [96] C. Shern, J. Tsay, H. Her, Y. Wu, R. Chen: *Response And Enhancement Of Surface Magneto-Optic Kerr Effect For Co-Pt(111) Ultrathin Films And Surface Alloy*. Surf. Sci. **429**, L497 (1999).
- [97] <http://www.flapw.de>: .
- [98] Y. Zhang, W. Yang: *Comment on "Generalized Gradient Approximation Made Simple"*. Phys. Rev. Lett. **80**, 890 (1998).
- [99] E. Lundgren, G. Leonardelli, M. Schmid, P. Varga: *A Misfit Structure In The Co/Pt(111) System Studied By Scanning Tunnelling Microscopy And Embedded Atom Method Calculations*. Surf. Sci. **498**, 257 (2002).
- [100] J. Tsay, C. Shern: *Diffusion And Alloy Formation Of Co Ultrathin Films On Pt(111)*. J. Appl. Phys. **80**, 3777 (1996).

- [101] O. Pietzsch, A. Kubetzka, M. Bode, R. Wiesendanger: *Observation Of Magnetic Hysteresis At The Nanometer Scale By Spin-Polarized Scanning Tunneling Spectroscopy*. Science **292**, 2053 (2001).
- [102] A. Hubert, R. Schäfer: *Magnetic Domains*. (Springer, Berlin, 1998).
- [103] A. C. Hewson: *The Kondo Problem to Heavy Fermions*. Cambridge University Press, Cambridge (1993).
- [104] J. Li, W.-D. Schneider, R. Berndt, B. Delley: *Kondo Scattering Observed at a Single Magnetic Impurity*. Phys. Rev. Lett. **80**, 2893 (1998).
- [105] V. Madhavan, W. Chen, T. Jamneala, M. F. Crommie, N. S. Wingreen: *Tunneling into a Single Magnetic Atom: Spectroscopic Evidence of the Kondo Resonance*. Science **280**, 567 (1998).
- [106] K. Nagaoka, T. Jamneala, M. Grobis, M. F. Crommie: *Temperature Dependence of a Single Kondo Impurity*. Phys. Rev. Lett. **88**, 077205 (2002).
- [107] P. Wahl, L. Diekhöner, M. A. Schneider, L. Vitali, G. Wittich, K. Kern: *Kondo Temperature of Magnetic Impurities at Surfaces*. Phys. Rev. Lett. **93**, 176603 (2004).
- [108] W. Chen, T. Jamneala, V. Madhavan, M. F. Crommie: *Disappearance of the Kondo resonance for atomically fabricated cobalt dimers*. Phys. Rev. B **60**, R8529 (1999).
- [109] H. C. Manoharan, C. P. Lutz, D. M. Eigler: *Quantum mirages formed by coherent projection of electronic structure*. Nature **403**, 512 (2000).
- [110] N. Knorr, M. A. Schneider, L. Diekhöner, P. Wahl, K. Kern: *Kondo Effect of Single Co Adatoms on Cu Surfaces*. Phys. Rev. Lett. **88**, 096804 (2002).
- [111] T. Jamneala, V. Madhavan, W. Chen, M. F. Crommie: *Scanning tunneling spectroscopy of transition-metal impurities at the surface of gold*. Phys. Rev. B **61**, 9990 (2000).
- [112] T. Jamneala, V. Madhavan, M. F. Crommie: *Kondo Response of a Single Antiferromagnetic Chromium Trimer*. Phys. Rev. Lett. **87**, 256804 (2001).
- [113] H. J. Lee, W. Ho, M. Persson: *Spin Splitting of s and p States in Single Atoms and Magnetic Coupling in Dimers on a Surface*. Phys. Rev. Lett. **92**, 186802 (2004).
- [114] B. C. Stipe, M. A. Rezaei, W. Ho: *Inducing and Viewing the Rotational Motion of a Single Molecule*. Science **279**, 1907 (1998).

- [115] A. J. Heinrich, J. A. Gupta, C. P. Lutz, D. M. Eigler: *Single-Atom Spin-Flip Spectroscopy*. *Science* **306**, 466 (2004).
- [116] C. F. Hirjibehedin, C. P. Lutz, A. J. Heinrich: *Spin Coupling in Engineered Atomic Structures*. *Science* **312**, 1021 (2006).
- [117] A. Wachowiak, J. Wiebe, M. Bode, O. Pietzsch, M. Morgenstern, R. Wiesendanger: *Direct Observation of Internal Spin Structure of Magnetic Vortex Cores*. *Science* **298**, 577 (2002).
- [118] S. Heinze, M. Bode, A. Kubetzka, O. Pietzsch, X. Nie, S. Blügel, R. Wiesendanger: *Real-Space Imaging of Two-Dimensional Antiferromagnetism on the Atomic Scale*. *Science* **288**, 1805 (2000).
- [119] K. von Bergmann, S. Heinze, M. Bode, E. Y. Vedmedenko, G. Bihlmayer, S. Blügel, R. Wiesendanger: *Observation of a Complex Nanoscale Magnetic Structure in a Hexagonal Fe Monolayer*. *Phys. Rev. Lett.* **96**, 167203 (2006).
- [120] K. von Bergmann, M. Bode, A. Kubetzka, M. Heide, S. Blügel, R. Wiesendanger: *Spin-Polarized Electron Scattering at Single Oxygen Adsorbates on a Magnetic Surface*. *Phys. Rev. Lett.* **92**, 046801 (2004).
- [121] M. L. Néel: *Ann. Geophys.* **5**(99) (1949).
- [122] W. F. Brown: *Thermal Fluctuations of a Single-Domain Particle*. *Phys. Rev.* **130**, 1677 (1963).
- [123] W. Wernsdorfer, E. B. Orozco, K. Hasselbach, A. Benoit, B. Barbara, N. Demoncey, A. Loiseau, H. Pascard, D. Mailly: *Experimental Evidence of the Néel-Brown Model of Magnetization Reversal*. *Phys. Rev. Lett.* **78**, 1791 (1997).
- [124] J. R. Friedman, M. P. Sarachik, J. Tejada, R. Ziolo: *Macroscopic Measurement of Resonant Magnetization Tunneling in High-Spin Molecules*. *Phys. Rev. Lett.* **76**, 3830 (1996).
- [125] R. F. Sabiryanov, K. Cho, M. I. Larsson, W. D. Nix, B. M. Clemens: *Growth and properties of small Co islands on a strained Pt surface*. *J. Magn. Magn. Mater.* **258-259**, 365 (2003).
- [126] M. A. Schneider: *Single-Spin Detection at Surfaces* in: *Magnetism goes Nano*, edited by S. Blügel, T. Brückner and C. M. Schneider, (Schriften des Forschungszentrums Jülich 2005).
- [127] G. Meyer, F. Moresco, S.-W. Hla, J. Repp, K.-F. Braun, S. Fölsch, K. H. Rieder: *Manipulation of Atoms and Molecules with the Low-Temperature Scanning Tunneling Microscope*. *Jpn. J. Appl. Phys.* **40**, 4409 (2001).

- [128] D. M. Eigler, C. P. Lutz, W. E. Rudge: *An atomic switch realized with the scanning tunnelling microscope*. Nature **352**, 600 (1991).
- [129] A. J. Heinrich, C. P. Lutz, J. A. Gupta, D. M. Eigler: *Molecule Cascades*. Science **298**, 1381 (2002).
- [130] D. M. Eigler, E. K. Schweitzer: *Positioning single atoms with a scanning tunnelling*. Nature **344**, 524 (1990).
- [131] L. Bartels, G. Meyer, K.-H. Rieder: *Basic Steps of Lateral Manipulation of Single Atoms and Diatomic Clusters with a Scanning Tunneling Microscope Tip*. Phys. Rev. Lett. **79**, 697 (1997).
- [132] S.-W. Hla, K.-F. Braun, K.-H. Rieder: *Single-atom manipulation mechanisms during a quantum corral construction*. Phys. Rev. B **67**, 201402 (2003).
- [133] J. A. Gupta, C. P. Lutz, A. J. Heinrich, D. M. Eigler: *Strongly coverage-dependent excitations of adsorbed molecular hydrogen*. Phys. Rev. B **71**, 115416 (2005).
- [134] S. Horch, H. T. Lorensen, S. Helveg, E. Lægsgaard, I. Stensgaard, K. W. Jacobsen, J. K. Nørskov, F. Besenbacher: *Enhancement of surface self-diffusion of platinum atoms by adsorbed hydrogen*. Nature **398**, 134 (1999).

Publications

- J. Wiebe, A. Wachowiak, F. Meier, D. Haude, T. Foster, M. Morgenstern, and R. Wiesendanger: *A 300 mK ultra-high vacuum scanning tunneling microscope for spin-resolved spectroscopy at high energy resolution*, Review of Scientific Instruments **75**, 4871 (2004).
- J. Wiebe, F. Meier, K. Hashimoto, G. Bihlmayer, S. Blügel, P. Ferriani, S. Heinze, and R. Wiesendanger: *Unoccupied surface state on Pt(111) revealed by scanning tunneling spectroscopy*, Physical Review B **72**, 193406 (2005).
- F. Meier, K. von Bergmann, P. Ferriani, J. Wiebe, M. Bode, K. Hashimoto, S. Heinze, and R. Wiesendanger: *Spin-dependent electronic and magnetic properties of Co nanostructures on Pt(111) studied by spin-resolved scanning tunneling spectroscopy*, submitted for publication.
- F. Meier, K. von Bergmann, J. Wiebe, M. Bode, and R. Wiesendanger: *Co Double-layer Nanostructures on Pt(111) Studied by Spin-resolved Scanning Tunneling Microscopy*, submitted for publication.

Conferences

- F. Meier: *Aufbau eines temperaturvariablen MOKE-Systems für die Charakterisierung ultradünner, magnetischer Schichten im UHV.*
Graduiertenkolleg "Nanostrukturierte Festkörper",
Hamburg (Germany), 3.7.2002 (talk).
- F. Meier, A. Wachowiak, J. Wiebe, D. Haude, M. Morgenstern, and R. Wiesendanger: *Eine UHV-Rastertunnelmikroskopieanlage für Messungen bei 300 mK und 14 T.*
67th Spring Conference, Deutsche Physikalische Gesellschaft,
Dresden (Germany), 24.3.2003 (poster).
- F. Meier: *Erste Rastertunnelmikroskopie-Messungen bei $T = 300$ mK.*
Graduiertenkolleg "Nanostrukturierte Festkörper",
Hamburg (Germany), 14.5.2003 (talk).
- F. Meier, J. Wiebe, A. Wachowiak, D. Haude, M. Morgenstern, and R. Wiesendanger: *An Ultra High Vacuum (UHV)-Scanning Tunneling Microscope (STM) system operating at 300 mK and 14 T.*
12th International Conference on Scanning Tunneling Microscopy,
Eindhoven (Netherlands), 23.7.2003 (talk).
- F. Meier, J. Wiebe, A. Wachowiak, D. Haude, M. Morgenstern, and R. Wiesendanger: *An Ultra High Vacuum (UHV)-Scanning Tunneling Microscope system operating at 300 mK and 14 T.*
13th International Winterschool on New Developments in Solid State Physics,
Mauterndorf (Austria), 16.2.2004 (poster).
- F. Meier, J. Wiebe, A. Wachowiak, D. Haude, T. Foster, M. Morgenstern, and R. Wiesendanger: *An Ultra High Vacuum (UHV)-Scanning Tunneling Microscope system operating at 300 mK and 14 T.*
68th Spring Conference, Deutsche Physikalische Gesellschaft,
Regensburg (Germany), 9.3.2004 (talk).
- F. Meier, J. Wiebe, A. Wachowiak, D. Haude, M. Morgenstern, and R. Wiesendanger: *An Ultra High Vacuum Scanning Tunneling Microscope system operating at 300 mK and high magnetic fields.*
International Symposium on Quantum Hall Systems and
Quantum Materials, Hamburg (Germany), 23.9.2004 (poster).

- F. Meier, K. Hashimoto, G. Bihlmayer, S. Blügel, P. Ferriani, S. Heinze, J. Wiebe, and R. Wiesendanger: *Observation of a Surface State on the Pt(111) Surface*.
13th International Conference on STM, Sapporo (Japan), 8.7.2005 (talk).
- F. Meier, K. von Bergmann, J. Wiebe, P. Ferriani, M. Bode, K. Hashimoto, S. Heinze, and R. Wiesendanger: *Spin-resolved scanning tunneling spectroscopy of Co nanostructures on Pt(111)*.
4th International Conference on Scanning Probe Spectroscopy (SPS06) and 1st International Workshop on Spin-Polarized Scanning Tunneling Microscopy (SPSTM-1), Hamburg (Germany), 25.7.2006 (poster).

Acknowledgments

I would like to thank Prof. Dr. Roland Wiesendanger for the possibility to work in his *Group R*, his supervision and the steady support of my work.

In particular Dr. Jens Wiebe is thanked. He has been an excellent supervisor in all aspects.

Many thanks to my LAB006-mates Dr. Daniel Haude and Dr. Katsushi Hashimoto, who supported me a lot. Especially Daniel's profound knowledge about electronics and technics was always a great help. I enjoyed the collaboration very much. Prof. Dr. Markus Morgenstern supported my work a lot until he left for Aachen. I would like to thank Dr. Matthias Bode and in particular Dr. Kirsten von Bergmann for the measurement period as well as the very good collaboration in LAB013. In addition, Matthias' hints and suggestions regarding experimental procedures and problems were always welcome in LAB006.

Many questions regarding computers and software were patiently answered by Felix Marczinowski.

I also thank for the help from the *theory* and the very good collaboration. The DFT calculations concerning the surface state were performed by Dr. Gustav Bihlmayer and Prof. Dr. Stefan Blügel from the *Forschungszentrum Jülich* as well as by Dr. Paolo Ferriani and Prof. Dr. Stefan Heinze from the *Spin Theory Group* in Hamburg. The calculations presented in Chapt. 5 have been mainly made by Paolo.

Each member of *Group R* contributes to a very fruitful and pleasant atmosphere. The various suggestions, hints, tips, tricks, discussions, explanations, and directives have been extremely helpful.

The workshops, especially the mechanical one, provided many parts of the equipment. Therefore, I would like to thank Rolf-Peter Benecke, Horst Biedermann and all other colleagues. Wolfgang Hatje delivered always the required liquid Helium even during times of temporary shortage.

Joining the mixed lunch group was always fun.

I am very grateful to Dr. Enno Scholz for proofreading this thesis.

Finally, special thanks to my parents and my sister as well as to Silvia and her family for their support and encouragement. This has been very important to me.